SAPIENZA UNIVERSITÀ DI ROMA
DOTTORATO DI RICERCA IN FISICA
SCUOLA DI DOTTORATO "VITO VOLTERRA"

Search for Supersymmetry with Gauge-Mediated Breaking using high energy photons at CMS experiment

THESIS SUBMITTED TO OBTAIN THE DEGREE OF
"Dottore di Ricerca" - Doctor Philosophiæ
PhD IN PHYSICS - XX CYCLE - OCTOBER 2007

BY

Francesco Santanastasio

Program Coordinator
Prof. Enzo Marinari

Thesis Advisors
Prof. Egidio Longo
Dott. Shahram Rahatlou
Dott. Daniele del Re

Contents

Introduction

The Standard Model (SM) of fundamental interactions is a successful theory describing strong, weak and electromagnetic interactions of elementary particles. The SM has been verified with high accuracy by several experiments in the last decades, and no deviations from theoretical expectations have been observed. In spite of the perfect agreement with all experimental observations, the SM has its natural drawbacks and unsolved theoretical problems, ranging from the origin of the particle masses to the nature of the Dark Matter in the Universe.

There are several alternative theories to the SM which try to solve such open issues. In these models, new physics, in terms of new particles and new interactions, is expected to be visible at the TeV energy scale. Among them Supersymmetry (SUSY) is one of the plausible theories for the physics beyond the SM, which foresees the existence of supersymmetric partners of the ordinary particles. If present, SUSY is expected to be broken, since super-partners with the same mass of their SM counterparts should have been already discovered by high energy physics experiments. The heaviest supersymmetric particles must have a mass larger than hundreds GeV.

There are several SUSY models which differ for the specific SUSY breaking mechanism. Theories with Gauge Mediated Supersymmetry Breaking (GMSB) allow a natural suppression of the Flavour Changing Neutral Currents in the theory. In addition, they foresee relatively high production cross section and have a very distinctive experimental signature.

Search for SUSY with gauge-mediated breaking has already been performed by experiments at LEP and Tevatron colliders, but results had shown no evidence of new physics. Lower limits on the masses of the lightest neutralino and the chargino of about 100 and 200 GeV, respectively, are set at the 95% confidence level by CDF and D0 experiments operating at Tevatron. These are the most stringent limits to date for GMSB models with a short-lived neutralino ($\tilde{\chi}_1^0$) as the next to lightest SUSY particle.

The future experiments at the Large Hadron Collider (LHC), in construction at the CERN laboratories of Geneva, will benefit of a larger energy in

the center of mass of $\sqrt{s} = 14$ TeV, compared to the $\sqrt{s} = 1.96$ TeV of the Tevatron, thus permitting the possible creation of heavy SUSY particles above the current Tevatron reach. In addition, the very high luminosity of the machine $\mathcal{L} = 10^{34}$ cm^{-2}s^{-1} will allow a relatively large production rate of such rare events, to claim discoveries or exclusions. The Compact Muon Solenoid (CMS) is one of the two general purpose detectors which will operate at the LHC. The search for SUSY is one of the most important items in the research program of the CMS experiment.

In this thesis, the study of the $\tilde{\chi}_1^0 \to \tilde{G}\gamma$ prompt decay within GMSB models, with a full simulation of the CMS detector, is presented. The presence of two high energy photons and the large missing transverse energy in the final state due to gravitinos ($\tilde{G}$), makes the experimental signature of such events very clear.

The dissertation is organized as follows:

- a theoretical outline of the SM, the main motivation for the physics beyond it and Supersymmetry are discussed in chapter 1;

- a description of the GMSB mechanism and the main experimental implications at colliders are discussed in chapter 2;

- a brief overview of the most important features of the LHC and the CMS experiment is presented in chapter 3;

- the study of the $\tilde{\chi}_1^0 \to \tilde{G}\gamma$ decay within GMSB models and the description of the main SM backgrounds, using generator level quantities, is discussed in chapter 4;

- the analysis strategy, the event reconstruction, the selection, and the determination of signal and background yields are discussed in chapter 5;

- the physics potential in terms of the statistics needed to claim discovery of SUSY and the prospects for future upgrades of this analysis are investigated in chapter 6;

- the conclusions are discussed in chapter 7.

In addition to the physics analysis, further studies on more hardware oriented issues related to the electromagnetic calorimeter and photon energy measurements, has been performed during graduate studies.

The first activity included both the development and the implementation of the analysis software for the stability test of the photodetector power

supply of the electromagnetic calorimeter (ECAL). The stability of the high voltage system has been verified at the level of 60 mV, which is necessary in order to keep the ECAL resolution for high energy electrons and photons within the 0.5%, as by design performances. This activity is discussed in appendix A.

Another relevant activity was the study of the feasibility of the ECAL calibration using the $\pi^0 \to \gamma\gamma$ decays, which is crucial for many physics analysis in CMS. This method presents some advantages compared to the other approaches. It does not rely on the information from the track detectors, and can be performed in the early days of data taking when alignment will be not fully understood yet. In addition, given the large production of π^0 mesons, this method has abundant statistics and the calibration can be performed in a short time ($\mathcal{O}$(days)). This study is reported in appendix B.

Chapter 1

Physics beyond Standard Model

The first part of this chapter is dedicated to a theoretical outline of the Standard Model. A brief introduction to the Higgs boson and both experimental and theoretical constraints on Higgs mass are discussed. Then, the main motivations for new physics beyond the Standard Model are presented. Finally, Supersymmetry is introduced as a possible alternative model to solve the open issues of the Standard Model.

1.1   Brief introduction to the Standard Model

The Standard Model (SM) of fundamental interactions describes strong, weak and electromagnetic interactions of elementary particles [1]. The SM has been verified with high accuracy by several experiments in the last decades, and no deviations from theoretical expectations have been observed. At the present, the combined results of all past and present experiments show a very good agreement with SM predictions. This makes of the SM a successful theory.

The SM is based on a "gauge" principle, according to which all the fundamental forces are mediated by an exchange of the gauge fields, corresponding to a specific symmetry group. The symmetry group of the SM is

$$SU_{color}(3) \otimes SU_{left}(2) \otimes U_{hypercharge}(1) \tag{1.1}$$

and the correspondent gauge fields are 8 gluons, 3 intermediate weak bosons and an abelian boson. In the framework of Quantum Field Theory, the SM is described by a Lagrangian that can be written in a very concise form as

$$\mathcal{L}_{SM} = \mathcal{L}_{gauge} + \mathcal{L}_{Yukawa} + \mathcal{L}_{Higgs} \tag{1.2}$$

The first term $\mathcal{L}_{gauge}$ describes the gauge interactions and it has been tested with the best precision at the experiments [2]. The second term $\mathcal{L}_{Yukawa}$ describes the flavour physics (quarks and leptons) and it has been investigated with particularly high precision in the last decades by several experiments [3]. The last term $\mathcal{L}_{Higgs}$ represents the electroweak symmetry breaking, that is the least tested part of the model. Such breaking mechanism is very important because all SM particles, both gauge bosons and fermions, acquire their masses due to the spontaneous breaking of $SU_{left}(2) \otimes U_{hypercharge}(1)$ symmetry group via a non-zero vacuum expectation value of the Higgs field. The Higgs boson is the missing particle of the SM, because it has not yet been discovered by experiments. Its mass m_H is still an unknown parameter of the theory.

Several direct searches and indirect measurements of the Higgs boson have been performed. The mass of the Higgs boson is constrained from precision electroweak data [2]. The most recent results of the global electroweak fit show that the preferred value for its mass, assuming the SM, is at 76 GeV, as shown in the figure 1.1. While this is not a proof that the Standard-Model Higgs boson actually exists, it does serve as a mass range guideline for its searches. The precision electroweak measurements can be used to set an upper limit at 95% confidence level on the Higgs boson at 144 GeV. On the other hand, experimental direct searches at LEP-2 experiments, have established a lower bound of 114.4 GeV, at 95% confidence level, on the Higgs mass [4]. If the results of direct and indirect searches are combined, the upper limit on the Higgs mass increases from 144 GeV to 182 GeV.

Finally, theoretical studies indicate that Higgs boson mass must be lower than 1 TeV, in order to be consistent with the SM [5].

1.2   Open issues in Standard Model

In spite of the perfect agreement with all experimental observations, the Standard Model has its natural drawbacks and unsolved theoretical problems. The most relevant ones, for what concerns this thesis, are described in the following.

Hierarchy problem - The "Hierarchy Problem" concerns the Higgs mass stability under radiative corrections. The radiative corrections to the SM Higgs boson mass, due to the fermion loop diagram in figure 1.2, can be written as

$$\Delta m_H^2 = \frac{|\lambda_f|^2}{16\pi^2} \cdot \left(-2\Lambda^2 + 6m_f^2 \cdot \ln(\Lambda/m_f) + ... \right) \qquad (1.3)$$
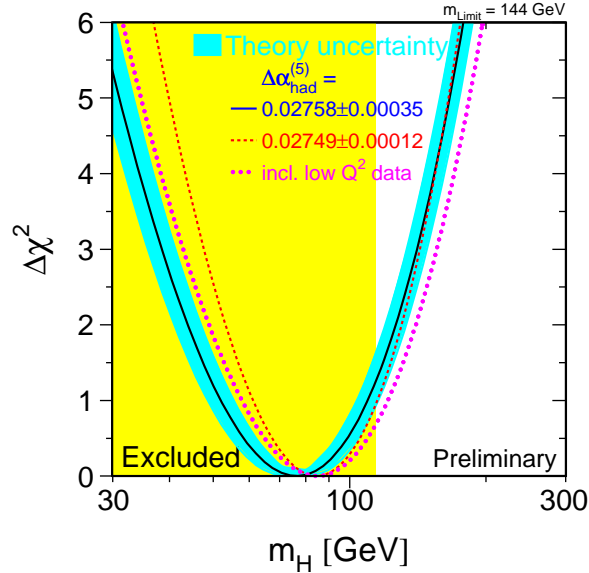
Figure 1.1: $\Delta\chi^2$ curve derived from precision electroweak measurements, performed at LEP and by SLD, CDF, and D0, as a function of the Higgs boson mass, assuming the Standard Model to be the correct theory of Nature [2].

where m_f is the fermion mass, λ_f the fermion coupling to the Higgs and Λ is the cut-off used in the integrals. These diagrams give a quadratic divergent contribution.

It is known that the SM must be a low-energy effective theory, and so a cut-off Λ should be imposed on these internal momenta, corresponding to the scale of new physics. The only known physics/interaction above the electroweak scale ($m_{W,Z} \approx 10^2$ GeV) is the gravity at Planck scale ($M_P = \sqrt{\hbar c / G_N} \approx 10^{19}$ GeV). If one assumes $\Lambda = M_P$, the Δm_H correction becomes several order of magnitude larger than the expected value for the SM Higgs mass, which is around 100 GeV, thus requiring an unnatural cancellation at tree level of these contributions. A plausible choice to have radiative corrections under control is that the scale of new physics is around TeV.

Origin of the particle masses - The mass spectrum of elementary particles ranges from few eV of the neutrinos [6], [7], to around 175 GeV

11
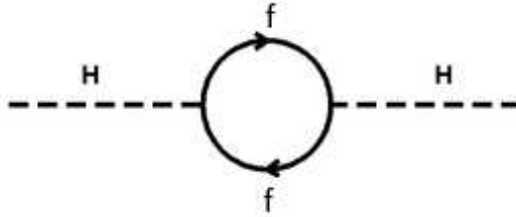
Figure 1.2: One-loop corrections to the Higgs squared mass parameter m_H^2, due to a Dirac fermion.

of the top quark [8]. There is no apparent fundamental reason for this large spread of mass values. The particles of the SM acquire mass proportional to the vacuum expectation value of the Higgs field $v = M_H/\sqrt{\lambda_H}$ and the mass spectrum is strictly connected with the unknown origin of the Higgs boson parameters.

Unification of Gauge couplings - The Grand Unification Theories (GUT) [9], are based on the hypothesis that all known interactions are different branches of a unique interaction, associated with a simple gauge group. If gravity is not included since it is too weak, the unification of strong (g_3), weak (g_2) and electromagnetic (g_1) couplings to a single GUT coupling (g_{GUT}) should occur at some high energy, far from the low energy range investigated by present experiments. In SM, the g_i couplings evolve, according with the renormalization group equation, as a function of the energy scale Q [10]

$$\alpha_i^{-1} = \alpha_i^{-1}(m_Z) + \frac{b_i}{2\pi} \log \frac{Q}{m_Z} \tag{1.4}$$

where $\alpha_i = g_i^2/4\pi$, $\alpha_i(m_Z)$ is the coupling constant calculated at the electroweak scale, b_i is a coefficient different for each coupling, depending on the number of quark and lepton generations and the number of Higgs doublet fields of the theory, and m_Z is the mass of the Z boson. Figure 1.3 shows the evolution of the inverse of the couplings as a function of the logarithm of energy scale. Although the values of the coupling constants tend to converge for low Q values, they do not come to a common value at any scale. This result means that the unification can only be obtained if new physics enters between the electroweak scale and the Planck scale.

Origin of the Dark Matter - Another open issue in particle physics and cosmology is the nature of Dark Matter. Several cosmological and
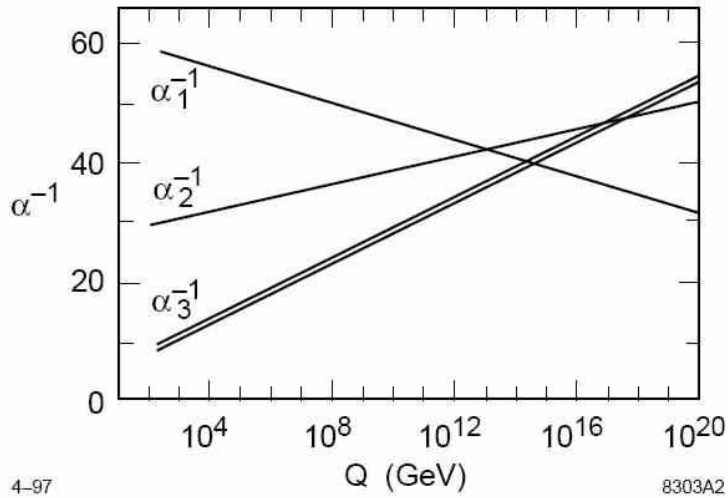
Figure 1.3: Evolution of the inverse of the coupling constants in the SM [10]. The theoretical error bands on α_3^{-1} are shown.

astrophysical measurements lead to the conclusion that around 25% of the energy density of the Universe is represented by neutral and weakly interacting matter, the so called Dark Matter. Figure 1.4 shows the composition of Universe, according to recent experimental results [11]. The problem is that SM has no possible candidates for such kind of matter.

These are the most important open issues in the SM. Several alternative models, including for example String Theory [12] and Extra Dimensions [13], have been proposed in the last years to solve these problems. Among them Supersymmetry is considered one of the plausible theories for the new physics beyond the SM.

1.3 Motivation for Supersymmetry

Supersymmetry (SUSY) [14] is one of the best studied theory for physics beyond the Standard Model, because it cancels the quantum loop effects that causes the hierarchy problem, and finds a solution to many of the unsolved problems discussed so far. In addition, it preserves all the results of the SM confirmed by experiments.

A Supersymmetry operator turns a bosonic quantum state into a fermionic
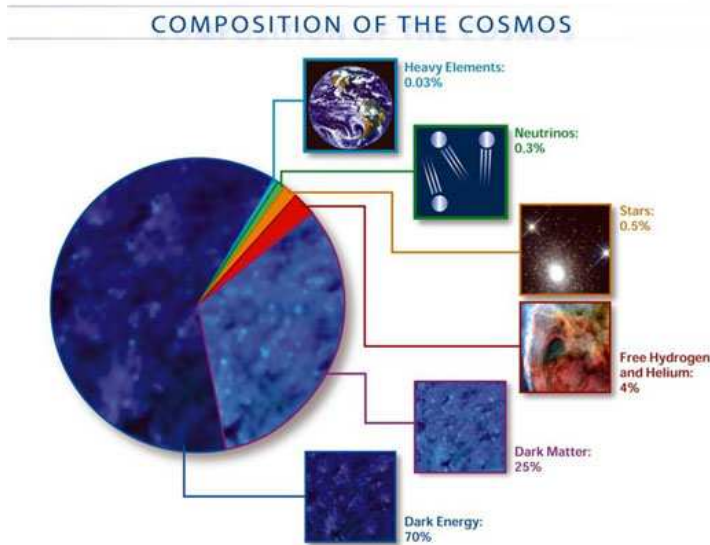
Figure 1.4: Composition of the Universe.

state, and vice versa,

$$\bar{Q}|\text{Boson}\rangle = |\text{Fermion}\rangle, \qquad Q|\text{Fermion}\rangle = |\text{Boson}\rangle \qquad (1.5)$$

where Q is the generator of SUSY algebra, [15]. Starting from a state with spin n, and acting by SUSY generator, one obtains a state with spin $n \pm 1/2$.

The basic idea of Supersymmetry models is that the theory is invariant under Q transformation. This requirement can be satisfied through the addition of supersymmetric fields. These fields represent the supersymmetric partners of the SM particles. To each fermion (boson) of the SM corresponds a supersymmetric boson (fermion) (see figure 1.5).

The presence of these new fields in the theory determines a natural cancellation of the quadratic divergences in the one-loop corrections to Higgs mass. In fact, in supersymmetric models, such radiative corrections due to the fermions, shown in equation 1.3, are exactly canceled by the corresponding terms due to the scalar supersymmetric particles, thus solving the Hierarchy Problem of the SM.

In addition, within the SUSY model, an unification of the gauge couplings can be obtained if the SUSY mass scale M_{SUSY} is around 1 TeV. This is shown in figure 1.6; the SUSY particles are assumed to effectively contribute to the running of the coupling constants only for energies above the typical SUSY

mass scale, causing the change in the slope of the dependence of coupling constants on the scale above 1 TeV. Even if this does not prove existence of Supersymmetry, it is considered its first "evidence", especially since M_{SUSY} was found in the range preferred by arguments on the Higgs mass corrections.
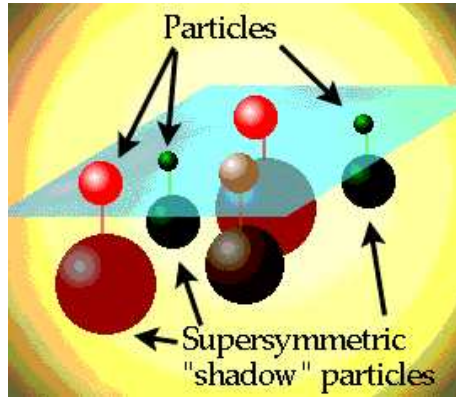
Figure 1.5: A schematic picture of the SM particles and the relative supersymmetric partners.
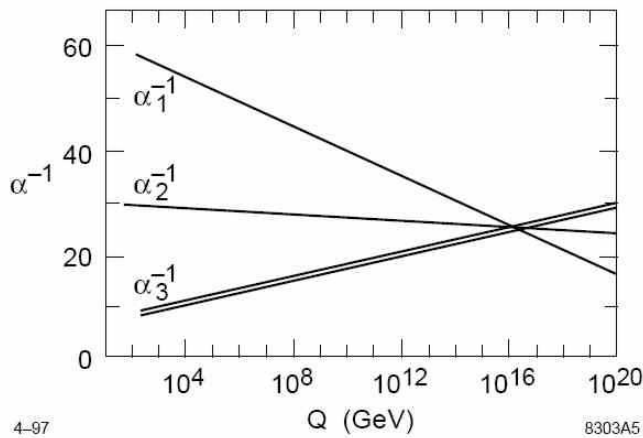
Figure 1.6: Unification of gauge couplings in SUSY models [10]. The theoretical error bands on α_3^{-1} are shown.

Finally, in SUSY models where R-Parity is conserved (see section 1.4), the Lightest Supersymmetric Particle (LSP) is stable, neutral and weakly

15

interacting. For this reason, the LSP is a good candidate for the Dark Matter in the Universe.

1.4 The Minimal Supersymmetric Standard Model (MSSM)

The Minimal Supersymmetric Standard Model (MSSM) is the minimal extension to the Standard Model that includes Supersymmetry [15]. The particle content of the MSSM is reported in table 1.1. There is one supersymmetric partner for each of the SM particles and two Higgs doublets in addition. The common notation to indicate the super symmetric fields is to use the suffix (ending) "s-" ("-ino") before (after) the name of the correspondent SM fermion (boson), for example quark/s-quark or Higgs/Higgs-ino.

If Supersymmetry were exact, superpartners would have the same mass of their SM counterparts and would have been already discovered by experiments. The absence of such observations can be explained by the fact that, if SUSY exists, it must be a broken symmetry, with SUSY masses large enough to evade current experimental bounds.

Multiplet name	Bosons	Fermions
Q	$(\tilde{u}, \tilde{d})_L$	$(u, d)_L$
U	$\tilde{u}_R$	$u_R^\dagger$
D	$\tilde{d}_R$	$d_R^\dagger$
L	$(\tilde{\nu}, \tilde{e})_L$	$(\nu, e)_L$
E	$\tilde{e}_R$	e_R
H$_1$	(H_1^0, H_1^-)	$(\tilde{H}_1^0, \tilde{H}_1^-)$
H$_2$	(H_2^+, H_2^0)	$(\tilde{H}_2^+, \tilde{H}_2^0)$
V	$W^\pm,\ W^0$	$\tilde{W}^\pm,\ \tilde{W}^0$
V'	B^0	$\tilde{B}^0$
G	g	$\tilde{g}$

Table 1.1: The particle content of the Minimal Supersymmetric Standard Model.

The Lagrangian of the MSSM can be written in the concise form as

$$\mathcal{L}_{MSSM} = \mathcal{L}_{SUSY} + \mathcal{L}_{Breaking} \tag{1.6}$$

where the first term is the SUSY generalization of the Standard Model Lagrangian, and the second part represents the SUSY breaking.

Once SUSY is broken, MSSM states can mix to form the physical mass eigenstates. This produces five Higgs bosons, after the electroweak symmetry breaking: two CP-even neutral states, h^0 and H^0, a CP-odd neutral state, A^0 and two charged states $H^\pm$. The gaugino and higgsino states mix to create four neutralinos, $\tilde{\chi}^0_1$, $\tilde{\chi}^0_2$, $\tilde{\chi}^0_3$, $\tilde{\chi}^0_4$ (ordered by increasing mass), and four charginos $\tilde{\chi}^\pm_1$, $\tilde{\chi}^\pm_2$. The exact mixing depends on the specific breaking mechanism considered (see section 1.5).

The states can be labeled with a multiplicative quantum number called R-parity which is defined as $R_p = (-1)^{3(B-L)+2s}$, where B, L and s are baryon and lepton number and the spin respectively. All SM particles have $R_p = 1$ and all the superpartners have $R_p = -1$. R-parity conservation has the effect of suppressing proton decay and of preventing any mixing between SM and SUSY particles. In addition, R-parity conservation has important consequences for experimental searches:

- any initial state created in laboratories has $R_p = +1$ and so SUSY particles must be created in pairs.

- any SUSY particle decays to an $R_p = -1$ state which contains another SUSY particle.

- the Lightest Supersymmetric Particle (LSP) is stable

- a light stable LSP is neutral and weakly interacting to have escaped detection.

1.5 Supersymmetry Breaking Mechanisms

Soft SUSY breaking is usually used to create the SUSY particle masses and it is done by introducing terms into the Lagrangian which involve only the SUSY particles, thus explicitly breaking the symmetry. This procedure introduces a total of around 100 new parameters into the theory, including masses, mixing angles and phases. The number of free parameters can be largely reduced by assuming that an underlying mechanism which produces the SUSY breaking in a natural way exists. A form of spontaneous symmetry breaking, like the Higgs mechanism, is not possible in the MSSM, because none of the fields can have non-zero vacuum expectation value (v.e.v.) to break SUSY without spoiling the gauge invariance.

The most common framework producing low-energy supersymmetry breaking is obtained by introducing a hidden sector. Accordingly, there exist two sectors: the usual MSSM fields belongs to the visible sector, while the second, the hidden sector, contains additional fields which lead to the breaking

of Supersymmetry. The SUSY breaking, occurring at some high energy in the hidden sector, is mediated to the visible sector by the exchange of weakly interacting "messengers". So far, there are four different possible mechanisms which describe this mediation:

- gravity mediation (SUGRA) [16];

- gauge mediation;

- anomaly mediation [17];

- gaugino mediation [18].

This work is focused on the Gauge Mediated Supersymmetry Breaking models. More details will be given in chapter 2.

Chapter 2

Gauge-Mediated Supersymmetry Breaking

Theories with Gauge-Mediated Supersymmetry Breaking (GMSB) [19],[20] provide an interesting scenario, in alternative to the well known Super-Gravity scenario (SUGRA). This chapter describes the GMSB mechanism and the main experimental implications at colliders.

A concise description of the breaking mechanism is reported in the section 2.1. Gravitino as the Lightest Supersymmetric Particle (LSP) in GMSB models is discussed in section 2.2. Sections 2.3 and 2.4 describe the phenomenological meaning of model parameters and the main benchmark scenarios respectively. Finally, the neutralino as Next to Lightest Supersymmetric Particle (NLSP) is discussed in section 2.5, including MSSM mass spectrum, cross section and experimental signature of $\tilde{\chi}_1^0 \to \tilde{G}\gamma$ decay.

2.1 Breaking mechanism in GMSB models

GMSB models have three sectors of particles. The first one is the *visible sector* which contains the particles of MSSM, i.e. quarks, leptons, gauge bosons, and two Higgs doublets, together with their supersymmetric partners. The second sector, called *hidden sector*, is responsible for Supersymmetry breaking. It contains a collection of yet-unobserved quantum superfields and the corresponding hypothetical particles, which do not interact via the SM force messengers, i.e. via gluons, photons, and W and Z bosons. Finally, the theory has a *messenger sector*, represented by some new superfields Φ which interact with MSSM via standard $SU_{color}(3) \otimes SU_{left}(2) \otimes U_{hypercharge}(1)$ gauge interactions and, at the same time, couple at tree level with the chiral superfield X of the hidden sector, via some Yukawa interaction. Figure 2.1 shows

a schematic view of the different sectors described so far.
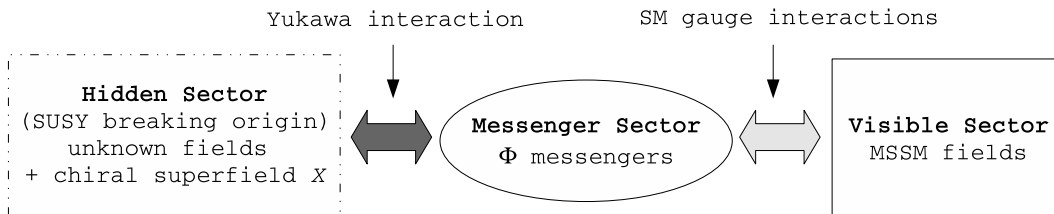
Figure 2.1: Schematic view of the Gauge-Mediated Supersymmetry Breaking scenario.

The simplest way to convey Supersymmetry breaking to the messenger sector is to introduce the following Yukawa interaction between the chiral superfield X and the messengers Φ:

$$W_m = \lambda X \Phi \bar{\Phi} \tag{2.1}$$

A generic chiral superfield contains three components:

- a scalar component with the energy dimension +1,

- a fermionic component with the energy dimension +3/2,

- an auxiliary scalar component with (unusual) energy dimension of +2.

Due to some (not specified yet) dynamics in the hidden sector, X gets non-zero v.e.v. of its scalar and auxiliary components

$$\langle X \rangle = \mathrm{M}_m + \theta^2 F_m \tag{2.2}$$

where θ is an additional "Grassman" coordinate of the superspace with energy dimension -1/2, and M_m [$mass$] and F_m [$mass^2$] are the fundamental mass scales in the theory, which can vary from several TeV up to the GUT scale. The fermionic component, which does not appear in the SUSY breaking, will be used later to give mass to the gravitino, as described in section 2.2. The coupling between messengers Φ and superfield X generates masses of order M_m for the messengers field and mass-squared splittings between the components of the messenger multiplets of order F_m ($M^2_{\Phi_1, \Phi_2} = \mathrm{M}^2_m \pm F_m$), where the coupling constant λ of the equation 2.1 can be re-absorbed in the definitions of the two fundamental scales. For this reason, $\sqrt{F_m}$ can be considered the measure of Supersymmetry breaking in the messenger sector. In addition, the relation $\mathrm{M}_m \ll M_P$, where M_P is the Planck mass, must be

20

satisfied in order to have negligible gravitational interactions. Finally, since the messenger mass have to be positive, the following relations need to be satisfied:

$$\sqrt{F_m} < \mathrm{M}_m \ll M_P \tag{2.3}$$

The visible sector is affected by the SUSY breaking in the messenger sector. Ordinary particles of the visible sectors are degenerate at tree level, since they do not directly couple to the X superfield. The splitting of their masses arises at one-or-more-loop level because of gauge interactions between MSSM and messengers fields, described by the Feynman diagrams in figure 2.2.
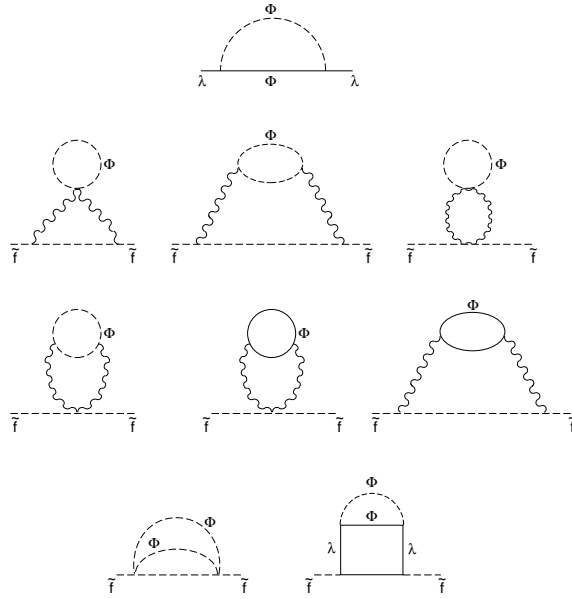
Figure 2.2: Feynman diagrams contributing to Supersymmetry breaking gaugino (λ) and sfermion ($\tilde{f}$) masses. The scalar and fermionic components of the messenger fields Φ are denoted by dashed and solid lines respectively. Ordinary SM gauge bosons are denoted by wavy lines.

Through this mechanism, the Supersymmetry breaking, i.e. the v.e.v. of X superfield, is transmitted from the hidden sector to the visible one, giving mass (at the scale M_m) to the gaugino λ_i and the scalar particles ϕ of MSSM:

$$m_{\lambda_i} = \mathrm{N}_m \cdot \Lambda \cdot f_\lambda(\alpha_i) \tag{2.4}$$
$$m_\phi^2 = \mathrm{N}_m \cdot \Lambda^2 \cdot f_\phi(\alpha_i) \tag{2.5}$$

where $\Lambda = F_m/\mathrm{M}_m$ can be interpreted as the effective SUSY breaking scale in the visible sector, N_m is the number of Φ messenger generations and f_λ, f_ϕ

are known functions of the three gauge couplings α_i of the SM. The final mass spectrum of MSSM particles is obtained by evolution of the sparticles masses from the M_m scale down to the MSSM scale (TeV), via renormalization group equations (RGE).

An important feature of gauge-mediated breaking is that Flavour Changing Neutral Currents (FCNC), which typically arise in all supersymmetric theories, are naturally suppressed in this model. In the GMSB mechanism, because mass terms of SUSY breaking are proportional to gauge quantum numbers, squarks and sleptons with same quantum numbers are degenerate in mass leading to a suppression of FCNC effects.

2.2 Gravitino as the Lightest Supersymmetric Particle

As a result of the spontaneous breaking of Supersymmetry, the physical spectrum contains a massless spin-1/2 fermion, the goldstino, which comes from the fermionic component of the chiral superfield X discussed so far. When a global supersymmetric theory is coupled to gravity and promoted to a locally supersymmetric theory, the goldstino is absorbed in the longitudinal component of the gravitino field (the supersymmetric partner of the graviton with spin 3/2) and it acquires a mass equal to

$$m_{\tilde{\text{G}}} = \frac{F_0}{\sqrt{3}M_P} \tag{2.6}$$

where F_0 can be interpreted as the fundamental scale of supersymmetry breaking. In general, a dimensionless factor C_{grav} can be introduced in the theory relating F_0 and F_m by

$$\text{C}_{grav} = \frac{F_0}{F_m} \tag{2.7}$$

where $\text{C}_{grav} \geq 1$. Therefore the equation 2.6 can be re-written as

$$m_{\tilde{\text{G}}} = \frac{\text{C}_{grav}}{\sqrt{3}} \cdot \frac{F_m}{M_P} \sim \text{C}_{grav} \left(\frac{\sqrt{F_m}}{100 \text{ TeV}} \right)^2 2.4 \text{ eV} \quad . \tag{2.8}$$

In GMSB models, the mass of other SUSY particles is above 100 GeV. For any relevant value of $\sqrt{F_m}$ (from several TeV to $\sim 10^{10}$ GeV), $m_{\tilde{\text{G}}}$ is lower than few GeV and therefore the gravitino is the LSP.

2.3   Description of GMSB parameters

The visible sector sparticle masses and couplings are fully determined by six parameters [21], [22]:

$$\Lambda, M_m, N_m, \tan\beta, \text{sign}(\mu), C_{grav} \qquad (2.9)$$

The GMSB parameters and their physical meaning are listed below.

- Λ ($= F_m/M_m$). The effective scale of SUSY breaking in the visible sector Λ sets the overall mass for the MSSM superpartners. To first approximation, it scales linearly with Λ, as derived from equations 2.4 and 2.5. To have sparticle masses in the TeV region, the parameter Λ must be of the order of 100 TeV.

- M_m. The messenger mass M_m appears in the RGE evolution of the MSSM parameters. Sparticle masses depend only on the logarithm of M_m. The relation $\Lambda < M_m \ll M_P$ can be derived for the equation 2.3.

- N_m. It is the number of messenger generations. Gaugino masses scale with N_m, while the squark and slepton masses scale like $\sqrt{N_m}$ as derived from equations 2.4 and 2.5. The N_m parameter is important to set which is the NLSP in the theory. For $\Lambda \approx \mathcal{O}(100\ \text{TeV})$, the typical value for the number of messenger generations is between 1 and 5, in order to have sparticle masses in the TeV region. In general, for low values of N_m, the neutralino $\tilde{\chi}_1^0$ is the NLSP, while for large values the stau $\tilde{\tau}$ is the NLSP.

- $\tan\beta$. The ratio $\tan\beta$ between the two MSSM Higgs v.e.v. is in the range $1 \leq \tan\beta \leq 50$, and it also contributes to fix which is the NLSP in the theory. Low values of $\tan\beta$ are excluded because, in that region, the top Yukawa coupling diverges below the unification scale. On the other hand, large values of $\tan\beta$ are excluded, in order to avoid the CP-odd neutral Higgs mass m_{A^0} to be negative.

- $\text{sign}(\mu)$. The sign of Higgs and Higgsino supersymmetric mass parameter μ. The module of μ is determined from the electroweak-breaking condition. The case $\mu < 0$ gives a larger mixing between the sparticles than the $\mu > 0$ case.

- C_{grav}. It is the ratio of F_0 to F_m ($C_{grav} \geq 1$ but also $C_{grav} >> 1$). It contributes to set the mass of gravitino

$$m_{\tilde{G}} \simeq C_{grav} \left(\frac{\sqrt{M_m \cdot \Lambda}}{100\ \text{TeV}} \right)^2 2.4\ \text{eV}, \qquad (2.10)$$

as derived from equation 2.8. Furthermore, NLSP lifetime scales with C_{grav}^2, as

$$c\tau_{NLSP} \simeq C_{grav}^2 \cdot \left(\frac{100 \text{ GeV}}{m_{NLSP}}\right) \cdot \left(\frac{M_m}{\Lambda}\right)^2 \cdot 10^{-5} \text{ m} . \qquad (2.11)$$
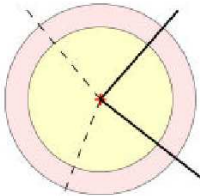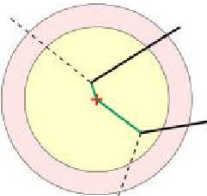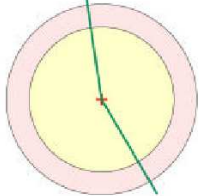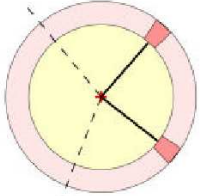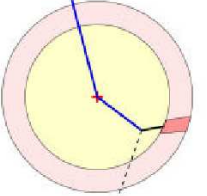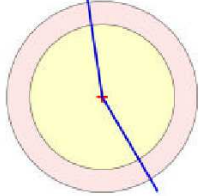
2.4 Benchmark scenarios

Assuming R-parity conservation, SUSY particles are expected to be produced in pairs at colliders, as discussed in section 1.4. Each of the two SUSY particles starts a decay chain, where other SUSY and SM particles are produced. At the end, two stable LSP are found in the final state, together with SM particles. This sequence is in common with all SUSY breaking models. In particular, since in GMSB models the decays of other SUSY particles into the LSP are strongly suppressed, the phenomenology depends crucially on the nature of NLSP, which decays into the LSP and one SM particle.

The NLSP can be either the lightest neutralino $\tilde{\chi}_1^0$ or the lightest stau $\tilde{\tau}_1$, depending on the particular choice of model parameters. The most important parameter for the determination of the NLSP is the number of messenger generations N_m. For $N_m = 1$, the $\tilde{\chi}_1^0$ tends to be the NLSP and it decays into $\tilde{G}$ and photon in most of the cases. For larger N_m values, the NLSP is the $\tilde{\tau}_1$ because, as N_m increases, the scalar masses increase less than their gaugino counterparts. The $\tilde{\tau}_1$ decays into $\tilde{G}$ and τ.

In addition to that, also the lifetime of the NLSP is relevant to determine the experimental signature of the SUSY processes. Depending on the value of C_{grav} parameter, the NLSP, produced at detector vertex, can in fact decay promptly, in flight inside detector, or even outside of it. In particular, $C_{grav} \approx 1$ gives a prompt NLSP decay while, for large values of C_{grav}, the NLSP is a long lived particle. Figure 2.4 shows the different experimental signatures depending on the nature of the NLSP and its lifetime.

All these scenarios are considered in the reference [23] where "The Snowmass Points and Slopes" (SPS) are introduced as a set of specific benchmark points and parameter lines (continuous set of parameters depending on one dimensional parameter) in the MSSM parameter space corresponding to different scenarios in the search for Supersymmetry at present and future experiments.

Figure 2.3: Experimental signatures for GMSB scenarios with stau (up) and neutralino (down) as the NLSP with different values of lifetime. The NLSP lifetime can be short, medium or long if $C_{grav} = 1$, $C_{grav} \geq 1$ or $C_{grav} >> 1$ respectively.

2.5 Neutralino as the Next to Lightest Supersymmetric Particle

The GMSB parameters of "SPS 8 line" are chosen for this study, and reported in table 2.1. With this choice of parameters the neutralino $\tilde{\chi}_1^0$ is the NLSP. In addition, C_{grav} parameter is fixed to 1, in order to study the prompt neutralino decay.

GMSB SPS 8 line					
M_m	N_m	$\tan\beta$	$sign(\mu)$	Λ	C_{grav}
$2 \cdot \Lambda$	1	15	$+1$	free	1

Table 2.1: GMSB SPS 8 line: scenario with neutralino NLSP [23]

2.5.1 MSSM mass spectrum and SUSY cross sections

In this model, production cross section and mass spectrum of SUSY particles are mostly determined by the parameter Λ. Total SUSY cross section, calculated at leading order (LO), is reported in table 2.2 for different values of parameter Λ. The main processes which contribute to the total SUSY cross section are shown in table 2.3 with the relative cross section; the values are reported for the point $\Lambda = 140$ TeV of SPS 8 line.

Λ (TeV)	100	120	140	160	180
σ_{SUSY} (fb)	2885	1050	455	215	110

Table 2.2: Total SUSY cross section σ_{SUSY} in pp interactions at $\sqrt{s} = 14$ TeV of SPS 8 line models for different values of free parameter Λ. Statistical uncertainties on cross sections are less than 2% (see description of generator tools for GMSB events in section 4.1).

Table 2.4 shows the full mass spectrum of SUSY particles for the point $\Lambda = 140$ TeV. The NLSP mass is $m_{\tilde{\chi}_1^0} \simeq 192$ GeV while LSP mass is only $m_{\tilde{G}} \approx 10$ eV, according with equation 2.10.

The dependence of the SUSY cross section, in pp interactions at $\sqrt{s} = 14$ TeV [1], and of the mass of some SUSY particles, as a function of Λ parameter, is summarized in figure 2.4. Mass of SUSY particles increases linearly

---

[1]The center of mass energy at LHC collider. See chapter 3 for details.

Process	σ_i (fb)	% of total SUSY cross section
$q^j + g \rightarrow \tilde{q}^j_{L,R} + \tilde{g}$	144.7	31.8%
$q + \bar{q}' \rightarrow \tilde{\chi}^0_2 + \tilde{\chi}^\pm_1$	85.1	18.7%
$g + g \rightarrow \tilde{g} + \tilde{g}$	52.5	11.5%
$q + \bar{q} \rightarrow \tilde{\chi}^\pm_1 + \tilde{\chi}^\mp_2$	43.6	9.6%
$q^i + q^j \rightarrow \tilde{q}^i_{L,R} + \tilde{q}^j_{L,R}$	39.3	8.7%
Other processes (~ 80)	89.8	19.7%
All processes	455	100%

Table 2.3: Cross sections for main processes with production of SUSY particles in pp interactions at $\sqrt{s} = 14$ TeV for point $\Lambda = 140$ TeV of GMSB SPS 8 line. q is a generic quark. Statistical uncertainties on cross sections are less than 2% (see description of generator tools for GMSB events in section 4.1).

Mass spectrum of SUSY particles (GeV)					
L/R	$\tilde{d}$	$\tilde{u}$	$\tilde{s}$	$\tilde{c}$	$\tilde{b}$	$\tilde{t}$
L	1527.75	1525.63	1527.75	1525.63	1467.15 ($\tilde{b}_2$)	1480.28 ($\tilde{t}_2$)
R	1453.41	1459.50	1453.41	1459.50	1446.82 ($\tilde{b}_1$)	1332.32 ($\tilde{t}_1$)
L/R	$\tilde{e}$	$\tilde{\nu}_e$	$\tilde{\mu}$	$\tilde{\nu}_\mu$	$\tilde{\tau}$	$\tilde{\nu}_\tau$
L	502.62	489.86	502.62	489.86	502.38 ($\tilde{\tau}_2$)	488.96
R	245.42	-	245.42	-	237.68 ($\tilde{\tau}_1$)	-
$\tilde{g}$	$\tilde{\chi}^0_1$	$\tilde{\chi}^0_2$	$\tilde{\chi}^0_3$	$\tilde{\chi}^0_4$	$\tilde{\chi}^+_1$	$\tilde{\chi}^+_2$
1135.72	191.69	377.86	561.27	577.86	378.36	577.78
h^0	H^0	A^0	H^+			$\tilde{G}$
116.99	730.16	725.27	734.59			$9.43\ 10^{-9}$

Table 2.4: Mass spectrum of SUSY particles for point $\Lambda = 140$ TeV of the GMSB SPS 8 line. Masses for left (L) and right (R) fields are also specified. $\tilde{b}_{1,2}, \tilde{t}_{1,2}$ and $\tilde{\tau}_{1,2}$ are the mass eigenstates coming from the mixing of correspondent L/R fields (see description of generator tools for GMSB events in section 4.1).

with Λ, as expected from equations 2.4 and 2.5. On the other hand, cross section decreases exponentially with parameter Λ, because, at fixed $\sqrt{s}$, it becomes more and more difficult to produce heavier sparticles in the final state.
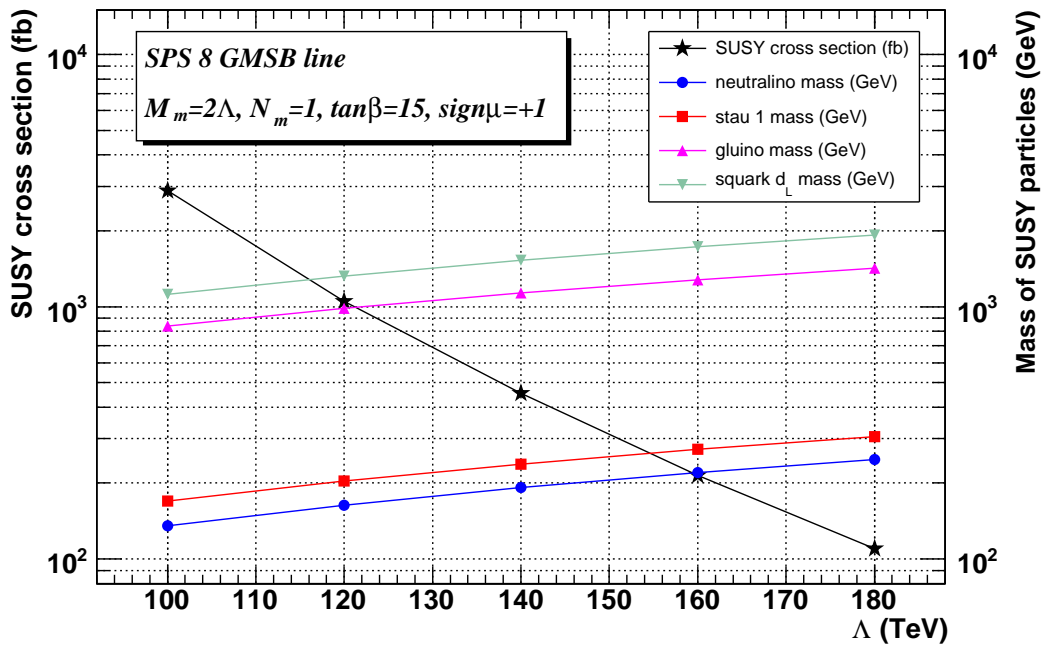

Figure 2.4: The GMSB SPS 8 line cross sections for pp interactions at $\sqrt{s} = 14$ TeV and masses of some chosen SUSY particles as a function of the scaling parameter Λ (see description of generator tools for GMSB events in section 4.1).

2.5.2 Experimental signature of $\tilde{\chi}_1^0 \to \tilde{G}\gamma$ decay

The experimental signature of GMSB events is determined by the characteristics of the NLSP decay that, for the SPS8 choice of parameters, is the neutralino $\tilde{\chi}_1^0$. Table 2.5 shows the branching ratio (BR) of neutralino in different channels as a function of parameter Λ.

Decay channel	$\tilde{\chi}_1^0$ branching ratios as a function of Λ (TeV)				
	$\Lambda = 100$	$\Lambda = 120$	$\Lambda = 140$	$\Lambda = 160$	$\Lambda = 180$
$\tilde{\chi}_1^0 \to \tilde{G}\gamma$	95.0%	91.1%	87.7%	85.1%	83.2%
$\tilde{\chi}_1^0 \to \tilde{G}Z^0$	3.0%	7.0%	10.4%	13.1%	15.0%
$\tilde{\chi}_1^0 \to \tilde{G}e^+e^-$	2.0%	1.9%	1.9%	1.8%	1.8%
$\tilde{\chi}_1^0 \to \tilde{G}h^0$	$6.0 \cdot 10^{-6}$	$4.5 \cdot 10^{-5}$	$8.0 \cdot 10^{-5}$	$1.2 \cdot 10^{-4}$	$1.4 \cdot 10^{-4}$

Table 2.5: Branching ratios of neutralino decay channels as a function of Λ parameter of the GMSB SPS 8 line (see description of generator tools for GMSB events in section 4.1).

This work is focused on the $\tilde{\chi}_1^0 \to \tilde{G}\gamma$ decay. Considering that a SUSY particles almost decays into another SUSY particle and one SM particle, the correspondent decay chain is

$$
\begin{aligned}
p + p &\to \tilde{S}_1 \tilde{S}_2 + X \\
(\tilde{S}_{1,2} &\to \tilde{\chi}_1^0 + X_{1,2} \to \tilde{G}\gamma + X_{1,2}) \\
&\to 2\tilde{G} + 2\gamma + X'
\end{aligned}
\tag{2.12}
$$

where $\tilde{S}_1$ and $\tilde{S}_2$ are two generic SUSY particles and $X, X_{1,2}, X'$ represents other SM particles produced in the event. This event has three interesting features from the experimental point of view:

1. there are photons with P_T larger than several tens GeV, which can be easily detected by an electromagnetic calorimeter;

2. the BR of neutralino into the photon channel is very high, around 85%-95% and slighlty model dependent. For this reason, two high P_T photons are expected in about 70%-90% of the SUSY events;

3. two LSP gravitinos are present in final state of each SUSY event. Gravitinos are light, stable, neutral and very weakly interacting; they escape from direct detection, creating an imbalance of the transverse energy in the event.

In addition, quark and leptons are produced in the decay chain of SUSY particles. Thus, high P_T jets are expected in the final state. Finally, neutralino lifetime is chosen to be very small by fixing parameter $C_{grav} = 1$, that gives $c\tau_{\tilde{\chi}_1^0} \approx 10^{-2}$ mm as derived from equation 2.11. Since the displacement between production and decay vertex of neutralino is very small, photons can be identified by the electromagnetic calorimeter as particles pointing to the interaction vertex. Figure 2.5 shows a schematic picture of a typical signal event.

Supersymmetry will be studied by experiments operating at the Large Hadron Collider (LHC). The high center of mass energy $\sqrt{s} = 14$ TeV of the LHC will allow to produce final states with heavy supersymmetric particles. The high luminosity[2] of the LHC will provide an high rate of SUSY events, even if the cross section for such processes is small, thus permitting discovery or exclusion for GMSB models. Chapter 3 describes the LHC and the CMS experiment, which is one of the two general purpose detectors operating in the next years at the CERN laboratories.

_____

[2]The definition of luminosity is given in section 3.1.
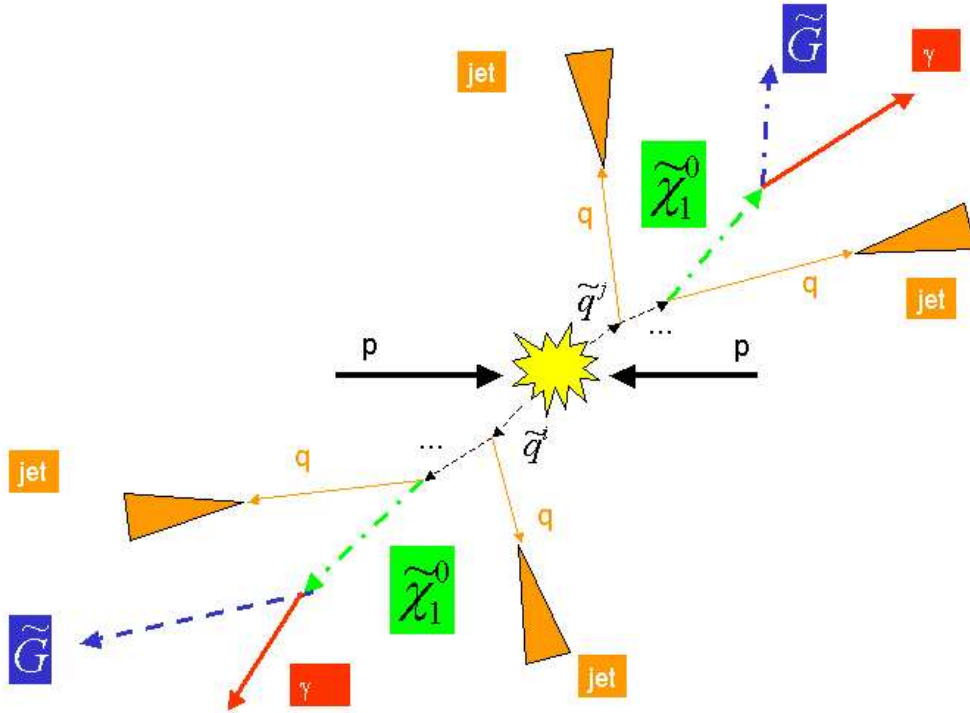
Figure 2.5: A schematic view of a GMSB event where the neutralino $\tilde{\chi}_1^0$ is the NLSP and it decays into $\tilde{\chi}_1^0 \rightarrow \tilde{G}\gamma$. A pair of generic squarks $(\tilde{q}^i, \tilde{q}^j)$ is produced in proton-proton (pp) collision at $\sqrt{14}$ TeV. Each of them starts a decay chain in which quarks q are generated. At the end, two NLSP $(\tilde{\chi}_1^0)$ are produced both decaying into LSP $(\tilde{G})$ and photon (γ).

Chapter 3

The Large Hadron Collider and the CMS experiment

This chapter gives a brief overview of the most important features of the Large Hadron Collider (LHC) and the CMS experiment. A concise description of the LHC and the phenomenology of proton-proton collisions at $\sqrt{s} = 14$ TeV are discussed, respectively, in sections 3.1 and 3.2. The descriptions of the CMS experiment and its main sub-detectors are given in section 3.3.

3.1 Overall design of the LHC

The Large Hadron Collider [24], currently under construction at the CERN laboratories of Geneve, is designed for proton-proton (pp) collisions at the center of mass energy of $\sqrt{s} = 14$TeV, with a bunch crossing every 25 ns [24] and a design luminosity of 10^{34} cm^{-2} s^{-1}. The LHC is being installed in the same circular underground tunnel (see figure 3.1), with the diameter of about 8.5 km, occupied until the year 2000 by the Large Electron Positron collider (LEP). It is planned to circulate the first beams in May 2008. First collisions at high energy are expected in mid-2008 with the first results from the experiments soon after.

The pp collision has been chosen, instead of the e^+e^- one of LEP, to reduce the synchrotron radiation, in order to accelerate the particles up to a very large energy. It was preferred to a $p\bar{p}$ collider because it allows to reach higher rate of events. In fact the low anti-proton production efficiency ($\approx 10^5$ protons are needed to create an anti-proton) and larger time needed to accumulate them, would make almost impossible to reach the high design luminosity of the LHC.
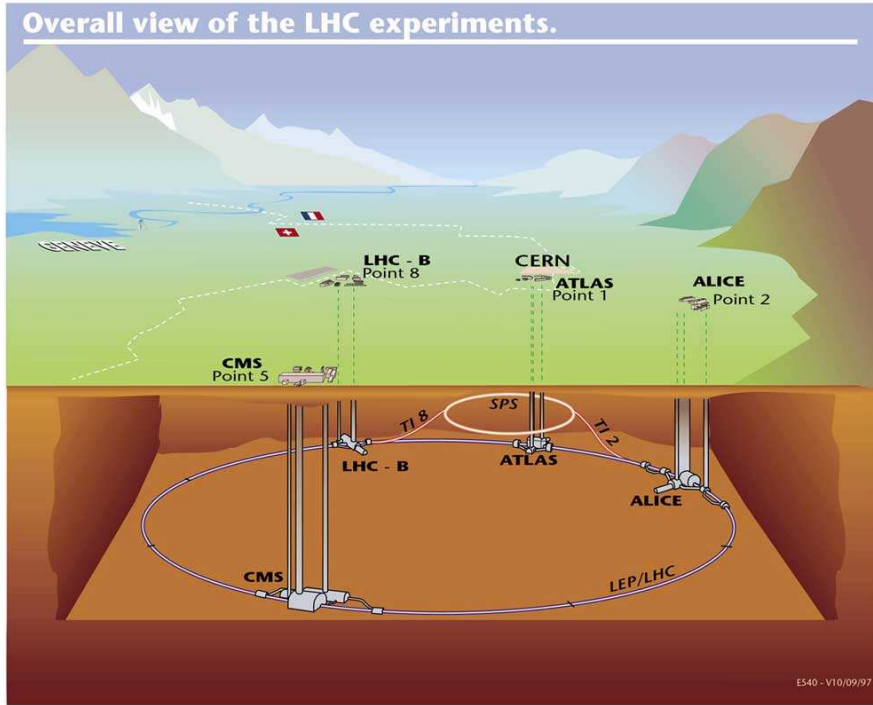
Figure 3.1: The LHC project.

The luminosity $\mathcal{L}$ is the parameter to quantify the performances of a collider, because the event rate R_i of a given process i, defined as the number of events occurring per unit of time, can be written as

$$R_i = \frac{dN_i}{dt} = \sigma_i \mathcal{L} \tag{3.1}$$

where σ_i is the cross section of the process i. The luminosity depends only on the machine parameters. Assuming a small crossing angle between the beams and Gaussian-shaped beam bunches, the luminosity $\mathcal{L}$ can be written as

$$\mathcal{L} = \frac{f n_b N^2}{4 \pi \sigma^2} \tag{3.2}$$

where f is the revolution frequency of particle bunches, n_b is the number bunches rotating in the accelerator, N is the number of protons in the two colliding bunches, σ is the RMS of beam profile distributions in the x/y plane orthogonal to the beam direction.

The LHC will operate at a bunch crossing rate of 40 MHz and at a design luminosity of $10^{34} \mathrm{cm}^{-2} \mathrm{s}^{-1}$, corresponding to the integrated luminosity in one

year of $\mathcal{L}_{int} = \int \mathcal{L}dt \approx 100 fb^{-1}$. However, it is expected that in the first years of operation, the LHC will run at the reduced luminosity of $2 \times 10^{33} \mathrm{cm}^{-2}\mathrm{s}^{-1}$. The two luminosity regimes are commonly called *low luminosity* and *high luminosity* scenarios. The LHC works as follows.

A small linear accelerator (Linac2) will bring the proton beams up to energy of 50 MeV and then the Proton Synchrotron Booster (PSB) will further accelerate protons up to 1.4 GeV. After passing through the Proton Synchrotron (PS) at 50 GeV, the beam will be finally injected in the Super Proton Synchrotron (SPS) where it will reach the energy of 450 GeV, the last stage before entering the LHC (see figure 3.2).
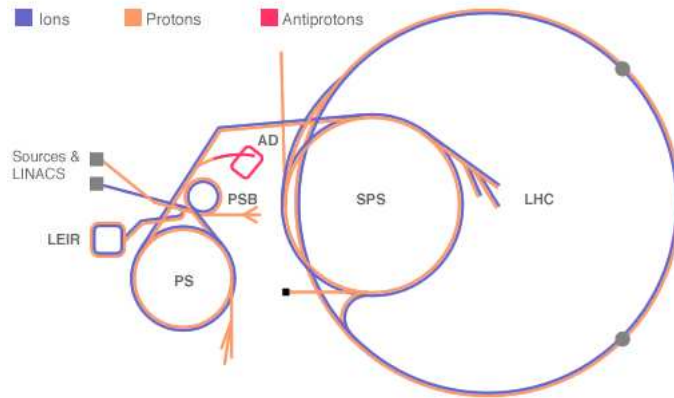
Figure 3.2: An overall view of particle accelerators at CERN.

In the LHC design, 1232 main dipole magnets (made of niobium-titanium super-conductor chilled with superfluid Helium at 1.9 K) generating a magnetic field up to 8.3 T, will be used to steer the particles into curvilinear trajectories (see figure 3.3). In addition, hundreds of quadrupoles, sextupoles and octupoles will be used for beam stability control.

The two beams will run in two contiguous pipes with vacuum inside, separated by 19.4 cm, that will be unified in proximity of the interactions points, where the experiments will be placed. Because of the high luminosity of the LHC, large thermal power will be generated near the pipes due to the synchrotron radiation, making necessary the presence of a suitable cooling system. For this reason also the pipes will be in contact with superfluid Helium at 1.9 K.

There will be two interaction points at high luminosity, where the two main experiments, ATLAS and CMS, will be placed. Two interaction points
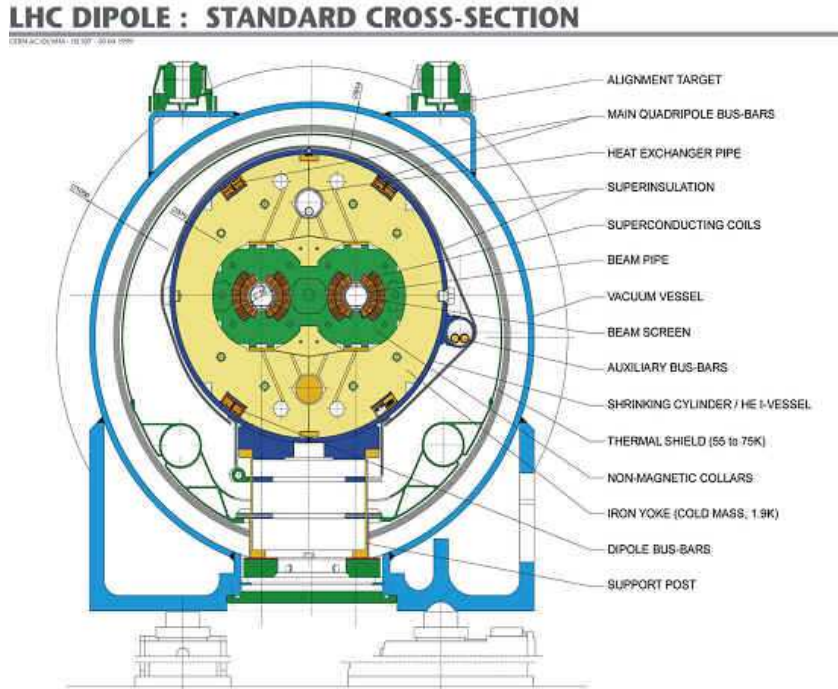
Figure 3.3: The cross section of a main dipole magnet of the LHC.

at low luminosity will be occupied by ALICE and LHCb experiments, optimized respectively for the heavy-ion physics and the b quark physics.

The main parameters of the nominal proton beam operation at the LHC are reported in table 3.1.

3.2 Phenomenology of proton-proton collisions

The general scheme of a pp interaction is shown in figure 3.4. When two protons collide at energies higher than their masses, the interaction involves their constituents, since the proton is resolved into its *partons* (quarks and gluons), carrying only a fraction x of the total momentum of the proton. The distributions of variable x for the different constituents are called Parton Density Functions (PDF) $f(x, Q^2)$, where Q^2 is the exchanged four-momentum during the interaction. At low Q^2, most of proton momentum is carried by the valence quarks, while at high Q^2, the PDFs are shifted towards lower values of x, so that the contribution of valence quarks and sea quarks is similar. This is seen in figure 3.5 which shows the CTEQ5L PDFs [25] at $Q^2 = 10 \text{ GeV}^2$, a low energy scale where the exchanged four-momentum is

LHC parameters	
Proton energy (collision)	7000 TeV
Proton energy (injection)	450 GeV
Ring circumference	26658.9 km
Bunch crossing time (b)	25 ns
Peak luminosity ($\mathcal{L}$)	$10^{34}\text{cm}^{-2}\text{s}^{-1}$
Dipole field at top energy	8.33 T
Number of collision points	4
Number of particles per bunch (N)	1.15×10^{11}
Number of bunches (n_b)	2808
RMS bunch length	7.55 cm
RMS beam size[1] (σ)	16.7 μm
Revolution frequency (f)	11.245 kHz
RF frequency	400.8 MHz

Table 3.1: The main parameters of the nominal proton beam operation for the high luminosity scenario.

Figure 3.4: The general schema of a pp interaction.

comparable with few times the proton mass, and $Q^2 = m_W^2$, the typical scale of electroweak interactions.

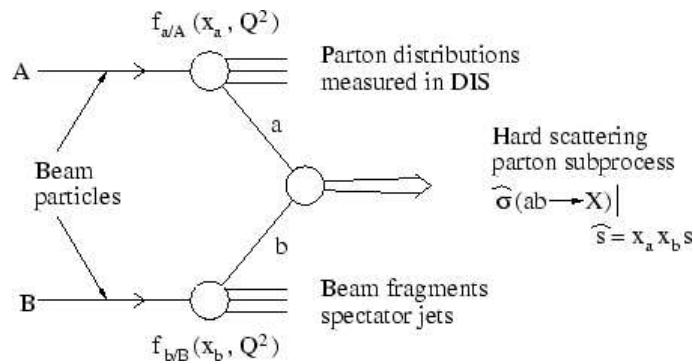The effective energy available for each interaction of the di-parton system is

$$\sqrt{\hat{s}} = \sqrt{x_a x_b s} \qquad (3.3)$$

where $s = 4E^2$ is the center of mass energy of the proton-proton system, E is the energy of both colliding protons and x_a and x_b are the fraction of proton energy carried by the two interacting partons (a and b). The cross section of a generic interaction $pp \rightarrow X$ can be written as

$$\sigma(pp \rightarrow X) = \sum_{a,b} \int dx_a dx_b f_a(x_a, Q^2) f_b(x_b, Q^2) \hat{\sigma}(ab \rightarrow X) \qquad (3.4)$$

where $\hat{\sigma}(ab \rightarrow X)$ is the cross section for elementary interaction between partons a and b at center of mass energy of $\sqrt{\hat{s}}$, and $f_a(x_a, Q^2)$ ($f_b(x_b, Q^2)$) represents the PDF for fraction x_a (x_b).

The variable $\hat{P}_T$ is often used in the description of two body parton processes $a + b \rightarrow c + d$; it represents the P_T in the rest frame of the hard process of one of the two partons in the final state.

Most predictions of the total cross section σ_{tot} at the LHC ($\sqrt{s} = 14$ TeV) show that [26]:

$$\sigma_{tot} \approx 100 \pm 10 \text{ mb} \quad . \qquad (3.5)$$

The inelastic interactions can be divided in two classes:

- Large distance collisions between the two incoming protons, where only a small momentum Q is transferred during the interaction. They are soft collisions with production of particles with large longitudinal momentum and small transverse momentum ($\hat{P}_T$ around 500 MeV). Since the scattering at large angle is suppressed, most of the particles escape detection along the beam pipe. This kind of processes is referred to as *minimum bias* events and represents the large majority of pp inelastic collisions.

- Head-on collisions at small distances between parton a from one proton and parton b from the other. In this hard scattering there is a transferred momentum larger than in minimum bias events and massive particles can be created, with higher $\hat{P}_T$ and large angles with respect to the beam line. These are the interesting physics events, but unfortunately they are rare. For example, the W (Z) production, with subsequent leptonic decay $W \rightarrow e\nu$ ($Z \rightarrow e^+e^-$), has a cross section at
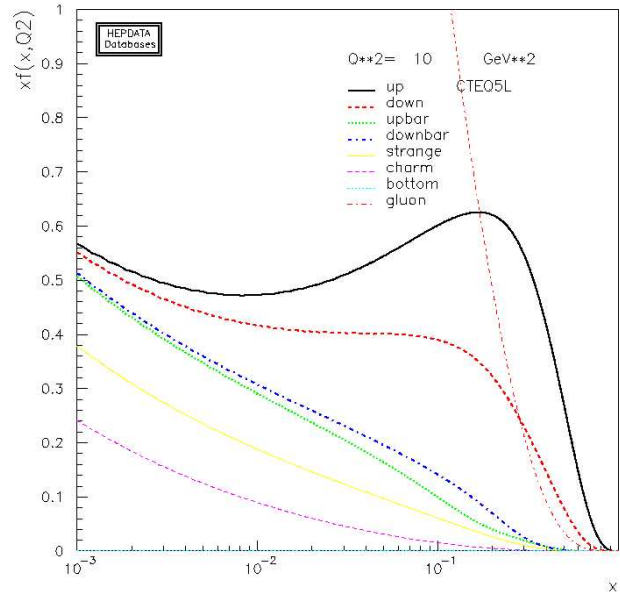
(a)
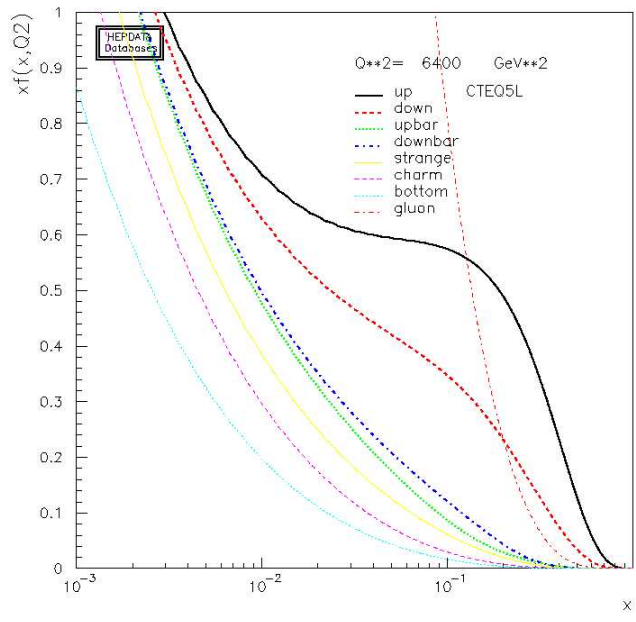
(b)

Figure 3.5: Parton Density Function CTEQ5L [25] for a proton with $Q^2 = 10$ GeV^2 (a) and $Q^2 = m_W^2$ (b)

the LHC of around 20 nb (2 nb), which results in an interesting event every about $5 \ 10^6$ ($50 \ 10^6$) pp interactions.

Table 3.2 shows the approximate rate of event at low luminosity for some physics processes at the LHC.

Process	Events/s	Event/year
$W \rightarrow e\nu$	40	4×10^8
$Z \rightarrow ee$	4	4×10^7
$t\bar{t}$	1.6	1.6×10^7
$b\bar{b}$	10^6	10^{13}
Higgs ($m = 120$ GeV)	0.08	8×10^5
Higgs ($m = 800$ GeV)	0.001	10^4
QCD jets ($P_T > 200$ GeV)	10^2	10^9

Table 3.2: Approximate event rates of some physics processes at the LHC for a luminosity of 2×10^{33}cm^{-2}s^{-1}. For this table one year is equivalent to 20 fb^{-1} [27].

On the other hand, the high luminosity has the drawback that the total event rate can become so high that several interactions overlap in the same bunch crossing (*pile-up*). The identification of an interesting high Q^2 interaction can be complicated by the presence, in the final state, of additional high P_T particles coming from pile-up events. The amount of pile-up can be roughly estimated by assuming the total inelastic cross section at LHC of $\sigma_{inelastic} \approx 80$mb and a bunch crossing time $b = 25$ ns. Considering that only a fraction $r \sim 80\%$ of the bunches will be filled, the average number of inelastic non-diffractive interactions per bunch crossing

$$\mu = \frac{\sigma_{inelastic} \cdot \mathcal{L}}{b \cdot r} \tag{3.6}$$

will be $\mu = 25$ ($\mu = 5$) at high (low) luminosity. This effect, that is limited in the low luminosity scenario, will become more and more important with the increasing of the LHC luminosity.

It is expected that the data produced at the LHC will elucidate the electroweak symmetry breaking mechanism, via the search of the Higgs boson, and provide evidence of new physics beyond the Standard Model. The experiments operating at the LHC will also be an instruments to perform precision measurements of the Standard Model parameters, thanks to the high event rate for the most of the SM processes.

The wide range of physics that is possible at the LHC requires a very careful design of the detectors. Section 3.3 is dedicated to the description of the CMS experiment and its main sub-detectors.

3.3   The CMS experiment

The Compact Muon Solenoid (CMS) is one of the two general purpose experiments which will tale data at the LHC (see figure 3.6) [28]. Its physics goals range from the search for the Higgs boson to the searches for new physics beyond the Standard Model, to the precision measurements of already known particles and phenomena [27].
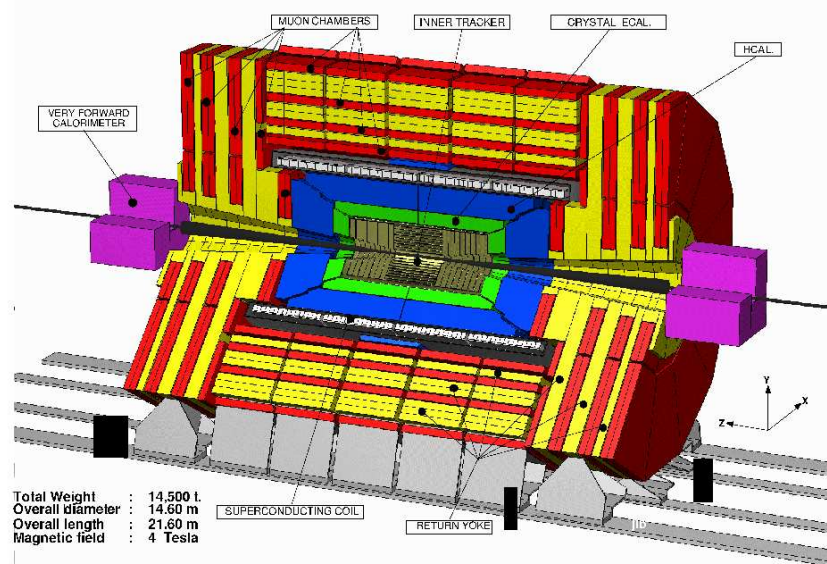
Figure 3.6: *A cross section layout of the CMS experiment.*

To achieve these goals excellent performances in photon and lepton reconstruction and particle identification are necessary. Besides, an optimal hermeticity and large geometric coverage calorimetry is required to detect invisible particles through missing energy measurements.

CMS has a central cylindrical section (the barrel) closed at both ends by disks which are orthogonal to the beam pipe (the endcaps). The central part of the detector is a 13 m long superconducting solenoid of 6 m diameter,

providing a 4 T axial magnetic field. The overall length of the detector is approximately 22 m, its width is 15 m and the total weight is about 12500 tons. The longitudinal view of one quarter of the detector is shown in figure 3.7 and the transverse view of the barrel region is given in fig 3.8.

The natural coordinate frame to describe the detector is a right handed Cartesian system with the x axis pointing toward the center of the LHC ring, the z axis directed along the beam axis and the y axis directed upward. Given the cylindrical symmetry of CMS, a convenient coordinate system is given by the triplet (r,ϕ,η), being r the distance from the z axis, ϕ the azimuthal coordinate with respect to the x axis and η the pseudorapidity, which is defined as $\eta = -\ln(\tan(\theta/2)$, where θ is the polar angle with respect to the z axis.

CMS consists of different subdetectors. Starting from the beam line there are

- the tracker, to measure the momentum of charged particles in the magnetic field and to identify the interaction vertex and the secondary vertexes;

- the electromagnetic calorimeter (ECAL), for an accurate measurement of the energy and of the position of photons and electrons;

- the hadronic calorimeter (HCAL), to measure the energy of both neutral and charged hadronic particles;

- the magnet, to bend the charged particles in order to allow the measurement of momentum;

- the muon system, to reconstruct the muonic tracks and to measure their momenta.

A brief description of each subdetector follows in the next sections. The trigger system, used for the online selection of interesting physical events, and the software tools will be also discussed. A detailed overview of the ECAL is given because this sub-detector is particularly important for the studies presented in this thesis.
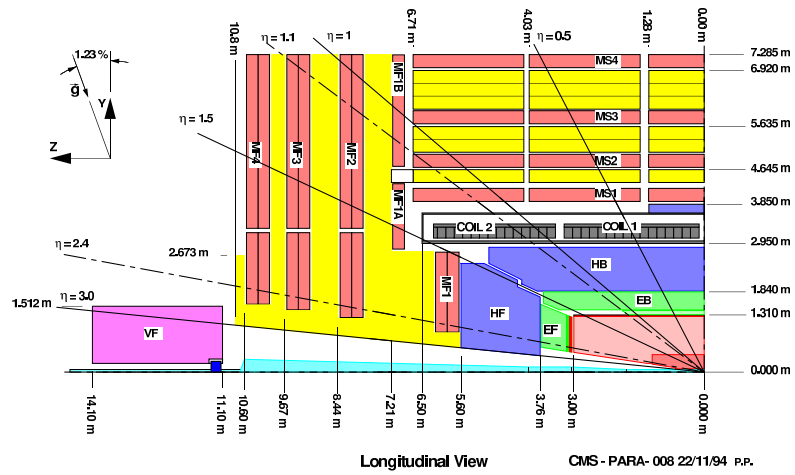
Figure 3.7: *Longitudinal view of one quarter of the CMS detector.*
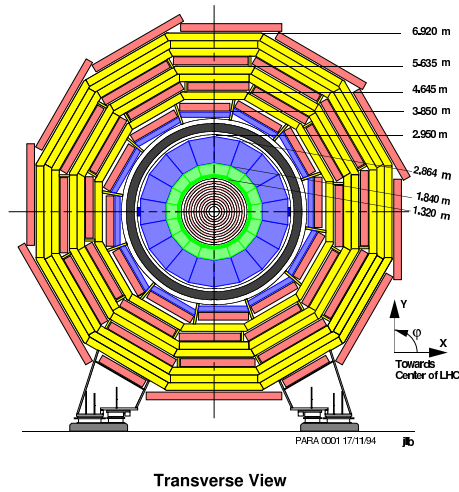
Figure 3.8: *Transverse view of the barrel region of CMS detector.*

3.3.1 Tracker

The tracker [29], placed within the magnetic field, is the subdetector which is closer to the interaction point. It is dedicated to track and vertex finding.

The silicon (Si) technology has been chosen for the whole tracker in order to provide good radiation hardness, high granularity and large hit redundancy to perform a good the pattern recognition.

The layout of the CMS tracker is shown in figure 3.9. Close to the interaction vertex, in the barrel region, are 3 layers of hybrid pixel detectors at a radius (r) of about 4, 7 and 10 cm. The size of the pixel is 100×150 μm^2. In the barrel part, the Si microstrip detectors are placed at r between 20 and 110 cm. The forward region has 2 pixel and 9 microstrip layers in each of the two endcaps. In order to avoid excessively shallow track crossing angles, the Inner Barrel is shorter than the Outer Barrel, and there are an additional three Inner Disks in the transition region between barrel and endcaps, on each side of the Inner Barrel. The total area of the Si detectors is around 200 m^2, providing a coverage up to $|\eta| = 2.5$. The material budget inside the active volume of the tracker increases from ≈ 0.4 X_0 at $\eta = 0$ to around 1 X_0 at $|\eta| = 1.6$, before decreasing to ≈ 0.6 X_0 at $|\eta| = 2.5$, as shown in figure 3.10.
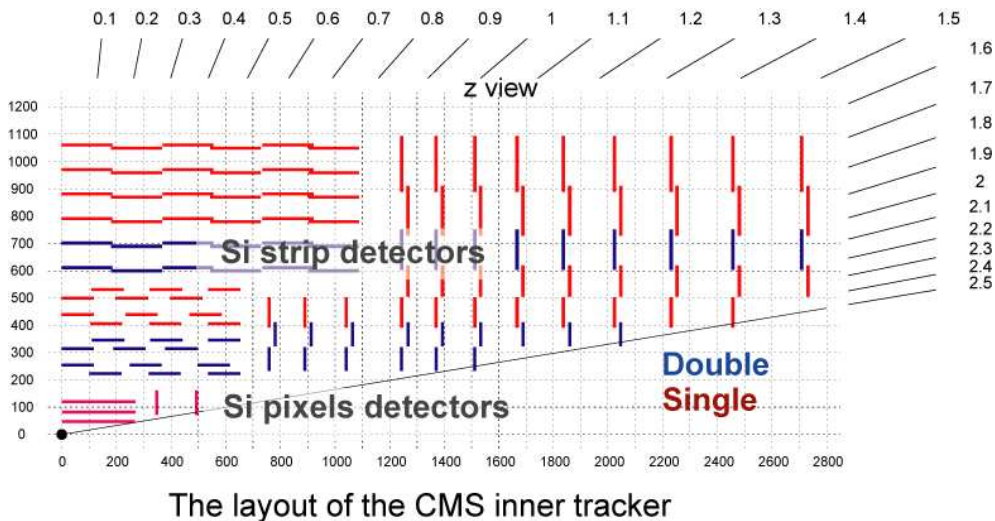
Figure 3.9: The tracker layout (1/4 of z view).
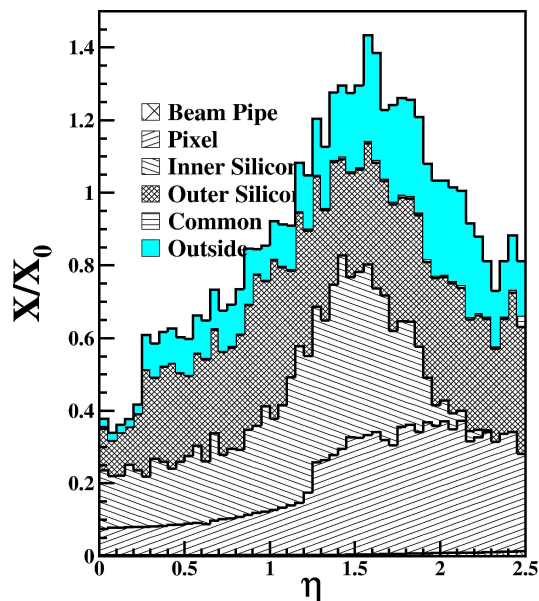
Figure 3.10: Amount of material (in radiation length X_0) in front of the ECAL, including that for tracker material, the beam pipe, the support structure and the cables, as a function of pseudo-rapidity [30].

3.3.2 Electromagnetic Calorimeter (ECAL)

The main goal of the electromagnetic calorimeter ECAL [30] is to precisely measure of the energy of electrons and photons, and contributes to the jet energy reconstruction. The main features of the ECAL are discussed in the following sub-sections.

ECAL layout and geometry

ECAL is a homogeneous calorimeter of almost 76000 Lead Tungstate $PbWO_4$ scintillating crystals divided into a barrel and two endcaps. A three dimensional view of the calorimeter is given in fig 3.11. The geometrical configuration in the transverse plane (y,z) is shown in figure 3.12.

The barrel ($|\eta| < 1.479$) consists of 36 supermodules, each one containing 20 crystals in $\phi \times 85$ crystals in η and covering an azimuthal arc of $20°$. The supermodules are divided along η in 4 modules made of submodules, which are the basic units of ECAL and which consist of 5×2 crystals each. The geometrical shape of the crystals slightly changes along η and there are 17 types of crystals, with length close to 230 mm and front face area of about 22×22 mm^2. The barrel granularity is $\Delta\phi\times\Delta\eta = 0.0175\times0.0175$, the crystals

45
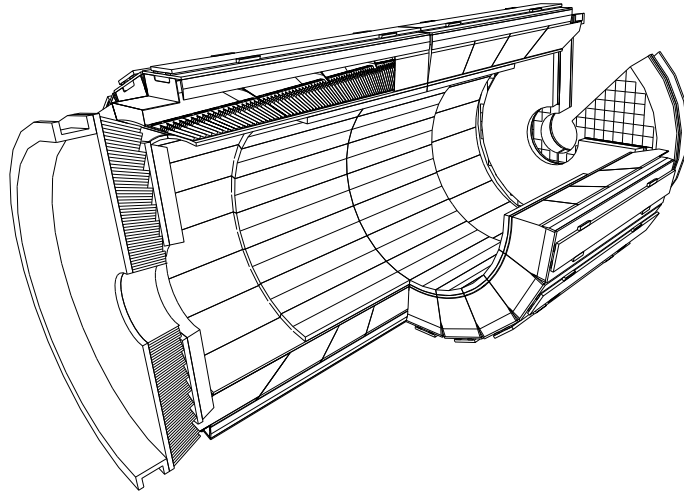
Figure 3.11: Three dimensional view of the ECAL.
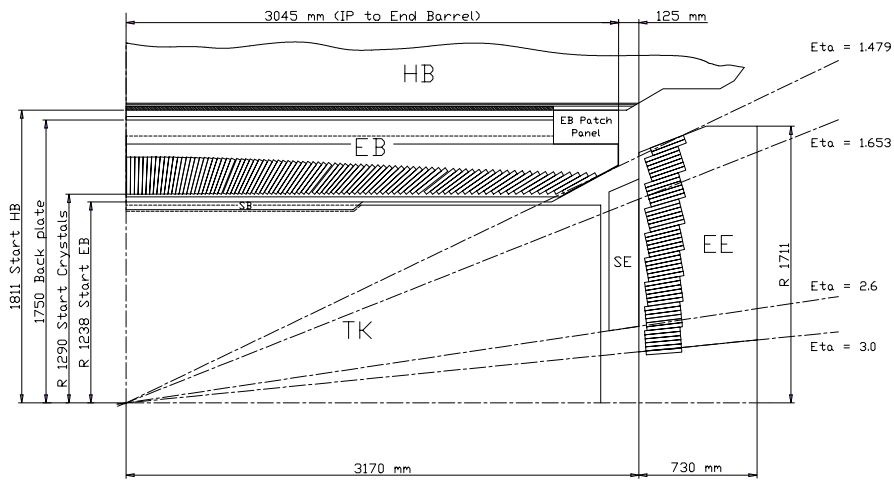
Figure 3.12: Transverse section through the ECAL, showing geometrical configuration.

46

are grouped into 5×5 arrays corresponding to the trigger towers. To avoid that cracks might align with the particles trajectories, the crystal axes are tilted by 3 degrees with respect to the direction from the interaction point, both in η and in ϕ.

The endcaps consist of two halves (*Dees*) and cover the pseudorapidity region $1.48 <| \eta | <3$. All the crystals have the same shape ($220 \times 24.7 \times 24.7$ mm^3) and they are grouped in structures of 5×5 crystals called supercrystals. The granularity varies from $\Delta\phi \times \Delta\eta$=0.0175$\times$0.0175 to 0.05$\times$0.05. As for the barrel, the crystals have a non pointing geometry.

To improve the π^0/γ separation and the vertex identification, a preshower is designed to cover the region between $| \eta | =$ 1.6 and $| \eta | =$ 2.6. It consists of two lead converters ($2X_0$ and X_0 thick) followed by silicon strips with a pitch of less than 2 mm. The strips following the two absorbers are disposed in orthogonal way. The preshower will operate at the temperature of -5°C.

Lead tungstate crystals

Different reasons brought to the choice of the PbWO$_4$ as active medium for ECAL. Its short radiation length ($X_0 = 0.89$ cm) and Moliere Radius ($R_M = 2.19$ cm) allow to build a compact and high granularity calorimeter. An important aspect is the fast response ($\sim$80% of the light is emitted within 25 ns), which is compatible with the high rate of events at the LHC. Finally the PbWO$_4$ has a good intrinsic radiation hardness, which makes it suitable to work in the hard LHC environment. The main drawback of the PbWO$_4$ crystals is the low light yield ($\approx 10^2\gamma$/MeV, only 0.1% with respect to NaI crystals), which makes an internal amplification for the photodetectors necessary.

An intensive Research and Development (R&D) work [31] has been done in recent years on the PbWO$_4$ crystals. It succeeded in improving the radiation resistance, transmission of the light and in reducing the light collection non uniformity along the crystal, in order to optimize the ECAL energy resolution.

The main parameters of the PbWO$_4$ crystals used in the ECAL are summarized in table 3.3.

Photodetectors

The photodetectors for ECAL have an intrinsic gain, have to be radiation hard, fast and able to operate in the strong CMS magnetic field. The Avalanche Photo-Diodes (APDs) [32] for the barrel and the Vacuum Photo-Triodes (VPTs) [33] for the endcaps have been chosen, because they match

$PbWO_4$ characteristics	
Density (g/cm^3)	8.28
Radiation length X_0 (cm)	0.89
Interaction length λ_{int} (cm)	22.4
Molière radius (cm)	2.19
Light decay time (ns) (% of light emitted)	25 (80%)
Maximum of emission (nm)	440
Light yield (γ/MeV)	$\approx$100
Rel. output (= 1 for NaI crystals)	0.01
Refractive index	2.3

Table 3.3: *Main characteristics of the $PbWO_4$ ECAL crystals.*

these characteristics.

The APDs are silicon devices insensitive to the 4 T magnetic field of the experiment and have an internal gain ($M = 50$ foreseen for CMS) essential for $PbWO_4$. Even if it is quite small, the APDs have an high quantum efficiency ($\sim$75% at 430 nm) which well matches the emission spectrum of the $PbWO_4$. Two APDs of 5×5 mm^2 surface are coupled to the back of each crystal in order to increase the acceptance to the scintillation photons, as shown in figure 3.13

The APDs affect all the terms of the energy resolution[2] which will be discussed later. The statistical fluctuations in the multiplication process influence the stochastic term of the energy resolution. The calorimeter noise is affected by the APD capacitance and by the leakage currents flowing on the surface and in the bulk of the APD. Finally the APD gain has a quite high dependence on the bias voltage ($\alpha_V = 1/M \cdot dM/dV = 3.1 \pm 0.1\%/V$) as well as on the temperature ($\alpha_T = 1/M \cdot dM/dT = -2.4 \pm 0.2\%/°C$). Thus, the photodetectors require a very stable power supply system, as gain fluctuations directly contribute to the constant term of the energy resolution. The contribution to the constant term, due to HV stability, should not exceed 0.2%. To satisfy this request, the voltage stability has to be of the order of 60-65 mV, for $M = 50$. The stability of the power supply for the APDs has been tested in detail in the last years; results are reported in the appendix A.

The APDs are seriously affected by the radiations. The damage is mainly due to the neutrons which create defects in the silicon increasing the leakage currents. Since the APDs can not survive the radiation doses of the endcaps,

---

[2]See equation 3.7
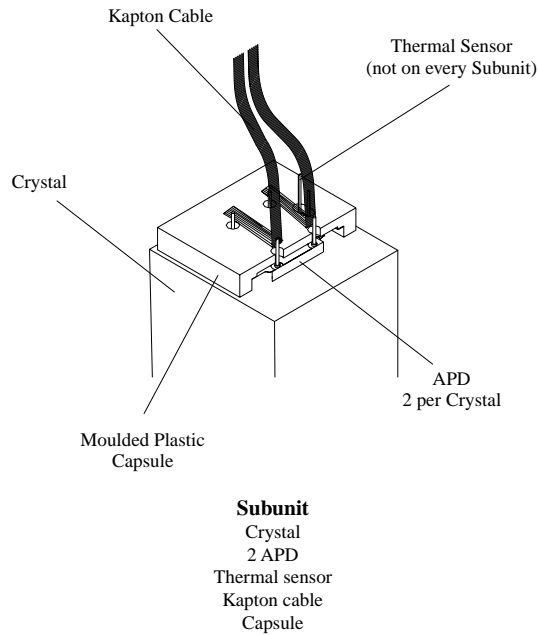
Figure 3.13: Subunit assembly.

the technology of the VPTs has been chosen for those regions. Details on VPTs can be found at reference [33].

Electronics readout

Important requirements are imposed on the Front-End (FE) electronics [34]. It has to be fast to match the 25 ns LHC crossing rate and it must keep the noise level below ∼50MeV per crystal; since it is placed on the detector it has to be also radiation hard. The schematic view of the FE system is shown in figure 3.14.

The electronics mirrors the trigger structure and its basic element is a group of 5×5 crystals called *trigger tower*. The signals coming from each photodetector are sent to a motherboard which hosts 5 Very Front End cards (VFE) and a Low Voltage Regulator card (LVR) providing the power for the VFE cards. Each VFE card houses 5 identical channels, where the signal from the photodetector is amplified, shaped and then sampled by a 12-bit sampling ADC working at 40MHz. Each channel of the VFE cards consists of a Multi Gain Pre-Amplifier MGPA, an ADC and a buffer. The MGPA provides three outputs at three different gains, which are digitized in parallel
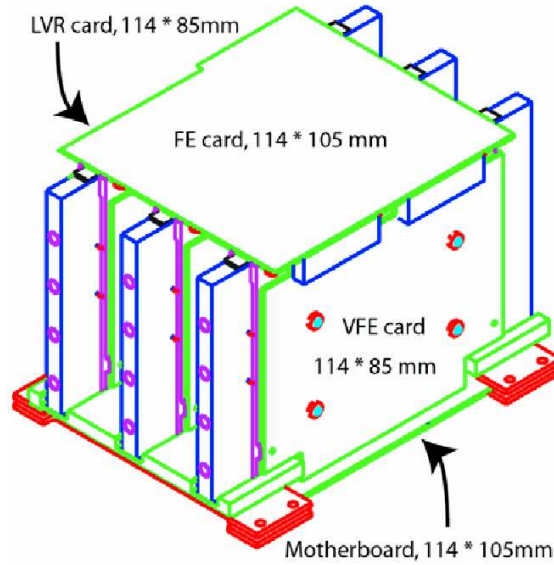
Figure 3.14: Front End system drawing with motherboard, VFE cards, LVR card, FE card and cooling system.

by four channel 12-bit ADC working at 40 MHz. The signals from the 5 VFEs are collected on the FE card, where sum of the data samples, corresponding to a group of 5×5 VFE channels, is performed. Part of the data are transmitted to the Level-1 trigger using a opto-hybrids on each FE card. All processed data are buffered in the FE card until Level-1 trigger decision is taken, and then, if the event is accepted, transmitted to the off-detector electronics and to the DAQ (data acquisition) system.

The energy resolution

The energy resolution of an homogeneous calorimeter is usually written as

$$\frac{\sigma_E}{E} = \frac{S}{\sqrt{E}} \oplus \frac{N}{E} \oplus C \tag{3.7}$$

where a, b and c represent respectively the *stochastic*, *noise* and *constant term* of the energy resolution. The different effects which contribute to each term are described below.

The **stochastic term** S includes the contribution of the Poissonian fluctuations in the number of electrons which are produced and collected. Contributions come from the light yield of the crystals, from the efficiency in the

light collection and from the quantum efficiency of the photodetectors. Important contributions also come from the fluctuations in the multiplication process inside the photodetectors, which are described by the excess noise factor F introduced so far. The target value for ECAL is $S = 0.027$ GeV$^{1/2}$ for the barrel and 0.057 GeV$^{1/2}$ for the endcaps, where the main contribution $(5\%/\sqrt{E(\text{GeV})})$ comes from the preshower sampling term. In the following the unit of measurement for the coefficient S is omitted, assuming that, in the equation 3.7, the energy E is measured in GeV.

The **noise term** N includes contributions from the electronic noise, both due to the photodetector and to the preamplifier, and from pile-up events. The contributions change at the different pseudorapidity and with the luminosity of the machine. The target values in the low and in the high luminosity phases are respectively 155 MeV and 210 MeV at $\mid \eta \mid = 0$, 205 MeV and 245 MeV at $\mid \eta \mid = 2$.

The **constant term** C is the dominating term at high energies and it includes many different contributions. Among them, the most important are:

- stability of the operating conditions, such as the temperature and the high voltage.

- presence of dead materials between the crystals and the rear and lateral leakage of the electromagnetic shower.

- longitudinal non uniformity of the crystal light yield.

- radiation damage of the crystals;

- channel intercalibration

The target value for the constant term of the CMS ECAL barrel is around 0.5%.

The energy resolution of the ECAL barrel has been studied using electrons of 20 to 250 GeV in a test beam [35]. The incident electron's energy is reconstructed by summing the energy in arrays of 3×3 channels. For electrons incident at the center of the studied 3×3 arrays of crystals, the mean stochastic term is 2.8%, the mean noise term is 125 MeV and the mean constant term is 0.3%. These values meet the design specifications of the detector. Figure 3.15 shows the energy resolutions of a crystal as a function of beam energy, together with the fitted resolution function curve described by equation 3.7.
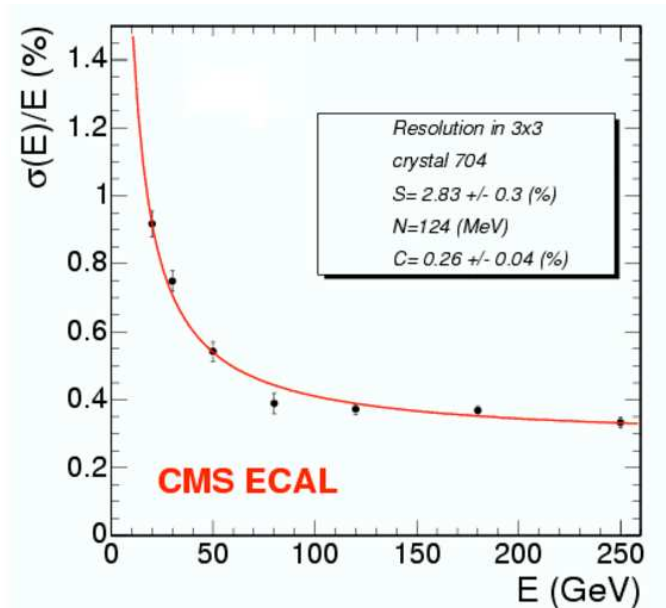
Figure 3.15: Energy resolution as a function of the energy for a 3×3 array of crystals centered on a specific ECAL crystal [35].

Calibration

The precision of the channel (crystal) intercalibration is an important issue for the calorimeter since it represents the dominant contribution to the constant term of the energy resolution. In the CMS collaboration, several methods have been investigated to precisely calibrate ECAL crystals ranging from the precalibration at laboratories to the Monte Carlo studies on the *in situ* measurements at the experiment.

The pre-calibration of the ECAL crystals is obtained by combining the results of three different calibration methods: a measurement of the light yield (precision around $\approx 4\%$) [36],[37], a precise inter-calibration with an electron beam (precision better than 0.5%) [37], and calibration using cosmic rays (precision around $2 - 3\%$) [38], [39].

During the LHC operation, the *in situ* calibration of the ECAL and fast monitoring will be crucial. The laser monitoring system [40] provides the corrections needed to account for changes in the crystal transparency induced by the radiation. At the beginning of the CMS operation, a very fast inter-calibration tool ("Energy Flow"), based on the ϕ symmetry of the released energy in a ring of crystals at a given pseudo-rapidity η, will be used to improve the pre-calibration [41].

To obtain a good global inter-calibration, this method must be combined with calibration algorithms using physics events, such as $Z \to e^+e^-$ [42] and $W \to e\nu$ [43] decays, to precisely inter-calibrate ECAL regions with different η (precision around $0.5 - 1\%$). The problem resides in the size of the sample that must be accumulated to reach the desired precision, i.e. ~ 1 fb^{-1} for the Z and > 5 fb^{-1} for the W, and the fact that calibration with W bosons requires the correct alignment of the tracking system.

The $\pi^0 \to \gamma\gamma$ decays, which are produced with a large cross section at the LHC, can be used to provide a fast *in situ* ECAL inter-calibration in the early days of the experiment. The feasibility of this calibration method has been study in detail using fully simulated QCD jet events; results are reported in the appendix B.

3.3.3 Hadron Calorimeter

The main goal of the hadron calorimeter HCAL [44] is to contribute to the reconstruction of events which involve both hadrons and invisible particles, by means of jet and missing energy reconstruction. High hermeticity and transverse granularity are necessary, together with a number of hadron interaction lengths sufficient to contain the energetic particles coming from high transverse momentum jets. A global overview of the hadron calorimeter system is shown in figure 3.16
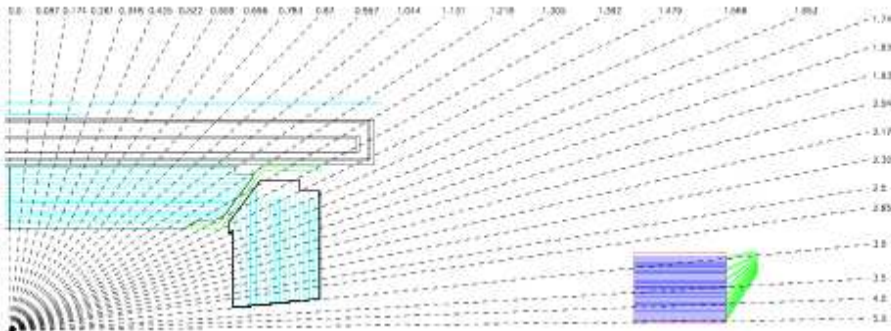
Figure 3.16: Overview of the CMS hadron calorimeter system.

The CMS central hadron calorimeter is placed inside the magnet and it consists of the barrel (HB) and two endcap (HE) disks. The barrel extends up to $\mid \eta \mid < 1.78$ and the two endcaps cover the pseudorapidity region between 1.305 and 3, partially overlapping the barrel. It's a sampling calorimeter with brass layers used as absorbers and plastic scintillators as active medium, while

the structural elements are made of stainless steel. The plastic scintillators are read by fibers which also act as wavelength shifters. The HB consists of 32 tower with a segmentation of $\Delta\eta \times \Delta\phi = 0.087 \times 0.087$ which matches the granularity of the ECAL trigger towers. The HE consists of 14 η towers with variable ϕ and η segmentations. Brass has been chosen as absorber instead of iron because it is easier to machine and it has a 10% shorter hadron interaction length. An HCAL tower with the corresponding ECAL trigger tower can be combined to form a Calo Tower, which is the basic calorimetry energy deposit used in several jet algorithms.

For low values of pseudorapidity the thickness of the HB can not ensure a satisfactory containment. To assure the necessary coverage in term of interaction lengths over the whole pseudorapidity range, an outer scintillator layer (HO) is placed outside the solenoid coil in the region up to $\mid \eta \mid < 1.305$ and two other scintillators are foreseen for the central region $\mid \eta \mid < 0.348$.

To improve the hermeticity, a separate very forward calorimeter (HF) is placed outside the magnet yoke, 11m away from the interaction point both in the forward and in the backward direction, extending the coverage up to $\mid \eta \mid = 5.191$. Due to the severe irradiation in the region, radiation hard quartz fibers have been chosen as active elements, interleaved with bulky steel working as absorber; the light is read out by means of photomultipliers.

The CMS calorimetric system is not compensated, being the response to the electromagnetic part of an hadron shower different from the response to the hadron part. The non compensation effects, which degrade both the linearity and the resolution, can be reduced by an appropriate weighting of the response of the ECAL and of the different layers of the HCAL. The hadronic energy resolution when combining informations from HCAL and ECAL is:

$$\frac{\sigma_E}{E} = \frac{1.00}{\sqrt{E/GeV}} \oplus 0.045 \tag{3.8}$$

The expected energy resolution for the HF is given for electrons and hadrons by

$$\frac{\sigma_E}{E} = \frac{1.38}{\sqrt{E/GeV}} \oplus 0.05 \qquad (electrons) \tag{3.9}$$

$$\frac{\sigma_E}{E} = \frac{1.82}{\sqrt{E/GeV}} \oplus 0.09 \qquad (hadrons) \tag{3.10}$$

3.3.4 Magnet

Both the tracker and the calorimeter system (ECAL+HCAL) are within a 4 T magnetic field which is generated by a solenoidal magnet coaxial to the

beam. The presence of the field allows the momentum measurement of the tracker thanks to the use of the curvature radius and at the same time reduces the effect of the pile-up by preventing the low energy particles to reach the ECAL barrel. Finally, the magnetic field in the return yoke is used for the reconstruction of the muon tracks in the muon chambers.

An overall view of the CMS magnet system is shown in figure 3.17. The CMS magnet system [45] consists of a superconducting coil housed in a vacuum tank and of a return yoke. The iron return yoke has a 12-sided cylindrical structure. The central part is divided in 5 coaxial rings, each one consisting of three layers where the muon chambers are hosted; the endcaps yokes instead are made of three disks, divided into 12 sectors. The superconducting coil is cooled down by liquid helium. It is housed in a vacuum tank which also works as supporting structure for the ECAL, the HCAL and the tracker. The main parameters of the magnet are given in table 3.4.

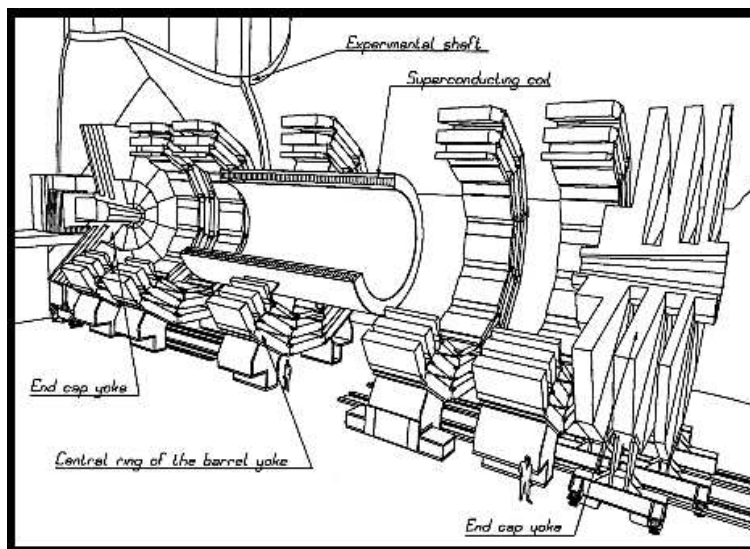Figure 3.17: Open view of the CMS magnet system with the names of the major project items.

3.3.5 Muon System

The muon system is the outermost of the CMS subdetectors. Its main goals are the identification of muons, thanks to their high penetrating power, and a precise measurement of their momentum, with the help of the information coming from the tracker. The muon system also works as trigger for events

The magnet parameters	
Magnetic field at the interaction point	4T
Coil length	12.48 m
Stored energy	2.70×10^9 J
Magnetic radial pressure	6.47×10^6 Pa
Axial compressive force at mid plane	148×10^6 N
Circulating current	20 kA

Table 3.4: *Some properties of the CMS solenoid.*

which involve muons and it provides a precise time measurement of the bunch crossing.

The CMS muon system [46] relies on three kinds of gaseous detectors: drift tubes (DT), cathode strip chambers (CSC) and resistive plate chambers (RPC). The DT and the CSC provide an excellent spatial resolution ($\approx$ 100μm) for the measurement of charged particle momentum; the RPC are used for trigger issues because of the very good timing. The active parts of the muon system are hosted into stations which are interleaved by the iron layers of the return yoke of the magnet. The longitudinal view of a quarter of the muon system is given in figure 3.18. The barrel extends up to $\mid \eta \mid < 1.3$, the endcaps up to $\mid \eta \mid < 2.4$. A detailed description of muon system can be found in [46].

3.3.6   Trigger

The trigger system is designed to reduce the total event rate of 10^9 Hz, expected for $\mathcal{L} = 10^{34}$cm^{-2}s^{-1}, to the order of 100 Hz, which is similar to the rate of interesting physics events at the LHC. As it was discussed in section 3.2, the total rate is dominated by minimum bias events. The trigger system therefore must largely reject the background and at the same time it must maintain high efficiency on interesting physics events at high P$_T$. This requires for the trigger a high level of complexity for the algorithms and at the same time the necessity to work fast. The trigger process is done in two main steps.

The **Level 1 trigger (L1)** reduces the rate to about 20 (100) kHz for the low (high) luminosity phase. The L1 trigger must be able to accept a new event every 25 ns. At a first level, the full data are stored in pipelines for a maximum of 3.2 μs, each one taking a decision in less than 25 ns. Since signal propagation delays are included in this pipeline data storage time, the
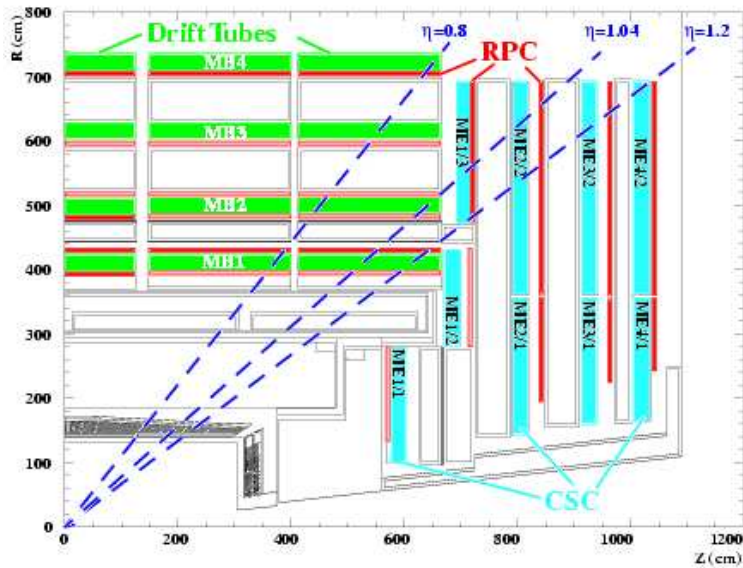
Figure 3.18: *Longitudinal view of one quarter of the CMS muon system.*

L1 decision about taking or discarding data from a particular bunch crossing has to be taken in less than 1 μs. If the first level trigger accepts the event, the data are moved to be processed by the HLT. To deal with the 25 ns bunch crossing rate, the L1 trigger has to take decisions in a time which is too short to read all the raw data from the whole detector, therefore it uses the calorimetric and muons information only. It is organized in a Calorimeter Trigger and a Muon Trigger; they both pass the information to the Global Trigger which takes a global decision.

The Calorimetric Trigger consists of trigger towers which match the granularity of ECAL and which are grouped in regions of 4 × 4 trigger towers. Four categories of objects (electrons and photons, central jets, forward jets and τ jets) are analyzed and the 4 candidates with highest transverse energy of each classes are passed to the Global Trigger, together with the total transverse energy and total missing energy vector of the event.

The Muon Trigger analyzes separately the three different detectors of the muon system (RPC,DT,CSC), and then it passes the four muon candidates with the highest track quality and P_T to the Global Trigger. The Global Trigger uses a logical combination of the data with the corresponding thresholds and it takes a decision.

The **High Level Trigger (HLT)** reduces the output rate down to 100 Hz.

The idea behind the HLT software is the regional reconstruction *on demand,* that means that only the objects which are in useful regions are reconstructed and the not interesting events are rejected as soon as possible. The HLT can be splitted into three logical levels. At the first one, only the full information of the muon system and of the calorimeters is used; at the second level the information from the tracker hits is added and finally, at a third level, the full information is available.

3.3.7   Simulation and reconstruction software

The reconstruction and analysis software of the CMS experiment has been revised in 2005. The old software ORCA [47] has given the way to the new framework CMSSW [48]. It has been done to better implement calibration and alignment strategies, ensure tracking and reproducibility of the reconstruction results, simplify and standardize the way physicists develop reconstruction algorithms, and facilitate interactive analysis. In the last two years, CMSSW was being in continuous evolution and this process is not already completed.

The work discussed in this thesis was being done in the period of transition between old and new framework. Both the study of the $\tilde{\chi}_1^0 \rightarrow \tilde{G}\gamma$ decay and the ECAL intercalibration with $\pi^0 \rightarrow \gamma\gamma$ decays, are based on the full simulation of the CMS detector within the old framework. The main reason concerns that, when these works started, reconstruction software was not yet fully validated for physics analyses and the available samples of simulated events was not sufficient to perform these studies.

The CMS reconstruction software ORCA (**O**bject-oriented **R**econstruction for **C**MS **A**nalysis) [47] is implemented in C++ and it is based on the Objected-Oriented technology [49]. It consists of the general framework CO-BRA [50] and of a set of packages which are used for the reconstruction of the different subdetectors. COBRA provides both the basic computing services, the tools and the utilities which are common to the many subdetectors. In the ORCA packages, the tools for the various subdetectors analysis tasks are developed.

The ORCA software is part of the CMS chain for the simulation and the digitization of the events, together with some other specific programs. The event generation uses CMKIN [51], which is usually interfaced to the PYTHIA [52] generator. The generated data are then simulated, i.e. propagated through the different subdetectors materials. The simulation is done with OSCAR [53], a C++ program based on GEANT4 [54] which describes both the active areas and the dead zones of each subdetector. Both signal

and pileup events are generated and separately simulated. They are then merged in the digitization phase, when the simulation of the noise and of the electronics is added. The pileup events are selected in a random way according to the desired luminosity. The ORCA software is used to simulate the response of detector electronics (digitization) in order to produce the input signals for the reconstruction process. The reconstruction algorithms and the tools for physics analysis are also developed using ORCA.

Chapter 4

Study of the $\tilde{\chi}_1^0 \to \tilde{G}\gamma$ decay

This chapter is dedicated to the study of the $\tilde{\chi}_1^0 \to \tilde{G}\gamma$ decay within GMSB models and the description of the main Standard Model (SM) backgrounds, using generator level quantities.

Section 4.1 describes the software tools used for generation of GMSB samples. Section 4.2 describes the decay modes and the kinematic properties of GMSB signal events. Finally the main sources of SM background are discussed in section 4.3.

4.1 Generator tools for GMSB events

The generation of GMSB events is done in two steps. In the first step, the software ISAJET (v7.69) [55] is used to generate the "SUSY Les Houches Accord" (SLHA) spectrum [56] containing supersymmetric model parameters, masses of SUSY particles, couplings, and branching ratios (BR). Then, SLHA spectra are used as input to PYTHIA (v6.2) [52], which calculates cross sections and performs quark showering and hadronization. The parton density function CTEQ5L [25] is used to model the internal structure of colliding protons at $\sqrt{s} = 14$TeV.

4.2 $\tilde{\chi}_1^0 \to \tilde{G}\gamma$ at generator level

In order to define the analysis strategy, this section describes the study of the $\tilde{\chi}_1^0 \to \tilde{G}\gamma$ decay at generator level. The input parameters given to ISAJET correspond to the set of parameters of GMSB SPS 8 line (see table 2.1). Five samples with different values of parameter Λ and fixed parameter $C_{grav} = 1$, corresponding to a very small $c\tau_{\tilde{\chi}_1^0} \approx 10^{-2}$ mm, are generated to study the

discovery potential of CMS detector in several SUSY mass scale scenarios. The number of generated events N_{gen}, the total SUSY cross section σ_{SUSY} at leading order, and the equivalent integrated luminosity $\mathcal{L}_{int}^{eq} = N_{gen}/\sigma_{SUSY}$ are reported in table 4.1 for signal samples, for each value of Λ. Plots and results shown in this section are obtained with the sample *GMSB_L140_ctau0*.

Sample name	Λ (TeV)	N_{gen}	σ_{SUSY} (fb)	$\mathcal{L}_{int}^{eq}$ (fb^{-1})
GMSB_L100_ctau0	100	4000	2885	~ 1.4
GMSB_L120_ctau0	120	4000	1050	~ 3.8
GMSB_L140_ctau0	140	9900	455	~ 21.7
GMSB_L160_ctau0	160	3800	215	~ 17.7
GMSB_L180_ctau0	180	4000	110	~ 36.3

Table 4.1: The value of GMSB parameter Λ, the number of generated events N_{gen}, the total SUSY cross section σ_{SUSY} at leading order and the equivalent integrated luminosity $\mathcal{L}_{int}^{eq}$ for different GMSB samples. Statistical uncertainties on cross sections are less than 2%.

4.2.1 Photon spectra from $\tilde{\chi}_1^0 \rightarrow \tilde{G}\gamma$ decay

Figure 4.1 shows the distribution of the number of photons in each event from neutralino decays when $\Lambda = 140$ TeV. There are two photons in the 77% of the events. This is consistent with the fact that there are two neutralinos in the event and $BR(\tilde{\chi}_1^0 \rightarrow \tilde{G}\gamma)^2 \sim (87.7\%)^2 \sim 77\%$. The fraction of events with two photons in the final state decreases as Λ increases, since $BR(\tilde{\chi}_1^0 \rightarrow \tilde{G}\gamma)$ decreases as well (see table 2.5).

Figures 4.2 and 4.3 show, respectively, the P_T and the η distribution of the first and the second highest transverse momentum photon of the event. The photon P_T spectrum is softer for GMSB models with lower Λ values because of the lighter neutralino mass. Around 80% of generated photons fall in the region $|\eta| < 1.5$, which corresponds to the barrel of the electromagnetic calorimeter. Therefore, this analysis requires at least two photons within the barrel, and with P_T of several tens of GeV.

4.2.2 Quark spectra from SUSY particles

Quarks are produced by the decay of SUSY particles and, after showering, hadronize to form high P_T jets which contribute to define the signature of
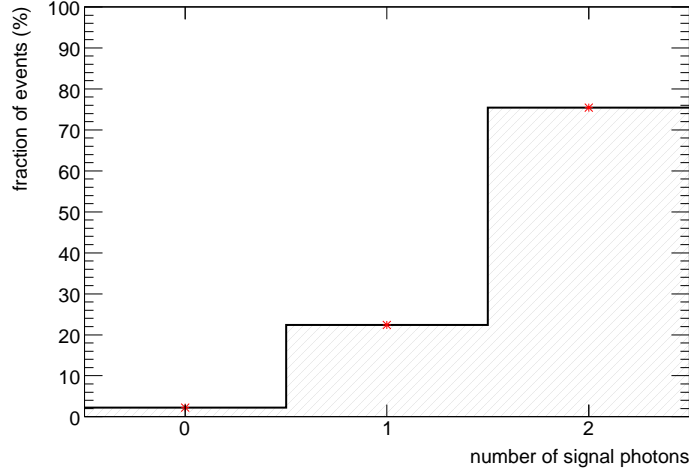
Figure 4.1: Number of generator photons in each event from neutralino decay for the signal sample *GMSB_L140_ctau0*.

signal events. The number of quarks in a signal event depends on the particular SUSY production process and the branching ratios of SUSY particles involved. The distribution of the number of primary quarks shows two contributions (see figure 4.4). The accumulation of events around five corresponds to events where there is a large multiplicity of primary quarks. In particular, the most likely decay chain is

$$gq \rightarrow \tilde{g} + \tilde{q} \tag{4.1}$$

where

$$\tilde{g} \quad \rightarrow \quad \tilde{\chi}_1^{\pm} qq \rightarrow \tilde{\chi}_1^0 W^{\pm} qq \tag{4.2}$$
$$\tilde{q} \quad \rightarrow \quad \tilde{g}q \rightarrow \tilde{\chi}_1^{\pm} qq \, q \rightarrow \tilde{\chi}_1^0 W^{\pm} qqq \tag{4.3}$$

then

$$gq \rightarrow 5q + 2W + 2\tilde{\chi}_1^0 \text{ (NLSP)} \tag{4.4}$$

where five quarks are produced from the prompt decay of SUSY particles. These quarks have a large transverse momentum and the distribution of η has a peak at low values, as shown in the figure 4.5.

In the remaining $\sim 40\%$ of the events there are no quarks from decay of SUSY particles. Two of the most representative decay chains of these events are

$$q\bar{q}' \quad \rightarrow \quad \tilde{\chi}_2^0 \tilde{\chi}_1^{\pm} \rightarrow H + W + 2\tilde{\chi}_1^0 \text{ (NLSP)} \qquad \text{and}$$
$$q\bar{q}' \quad \rightarrow \quad \tilde{\chi}_2^0 \tilde{\chi}_1^{\pm} \rightarrow \tilde{\tau}^{\pm}\tau^{\mp}\tilde{\chi}_1^0 W^{\pm} \rightarrow 2\tau + W + 2\tilde{\chi}_1^0 \text{ (NLSP)} \quad . \tag{4.5}$$
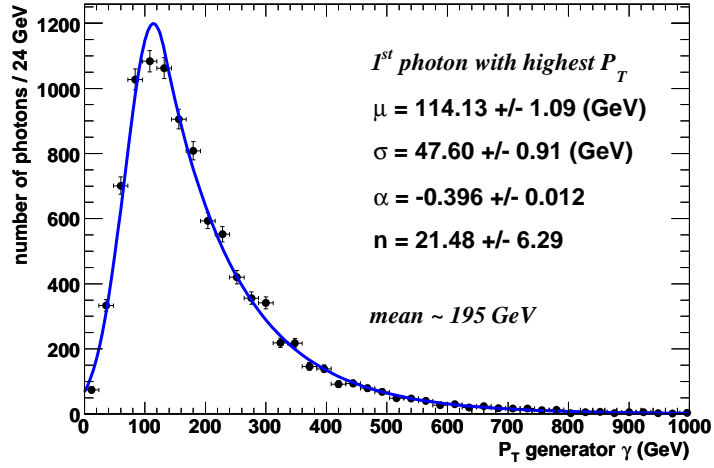
(a)
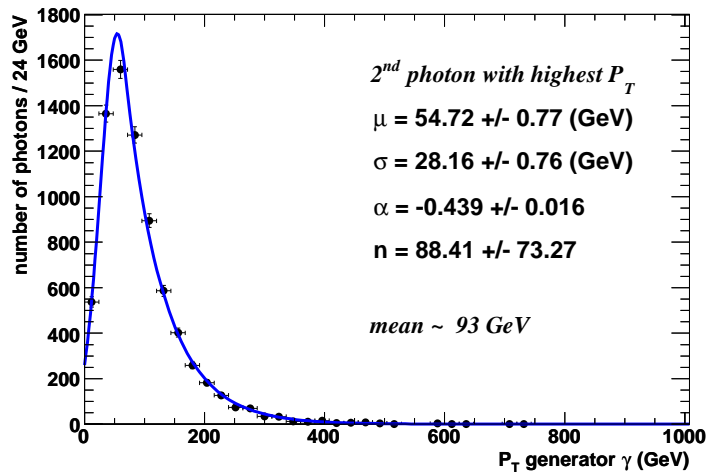
(b)

Figure 4.2: Distribution of P$_T$ of the first (a) and the second (b) highest transverse momentum photon of the event for the signal sample *GMSB_L140_ctau0.*
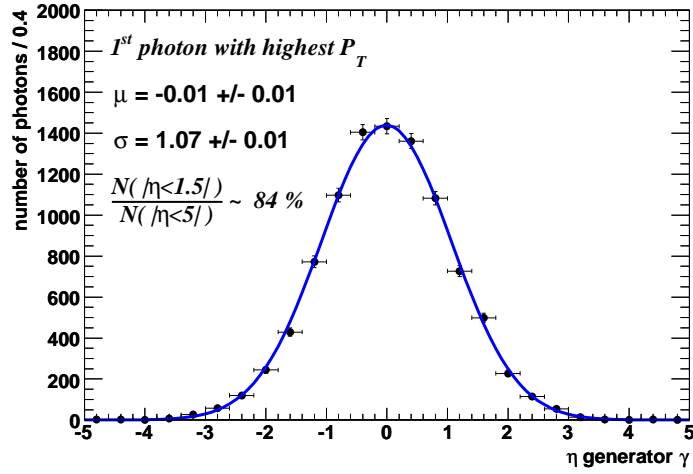
(a)
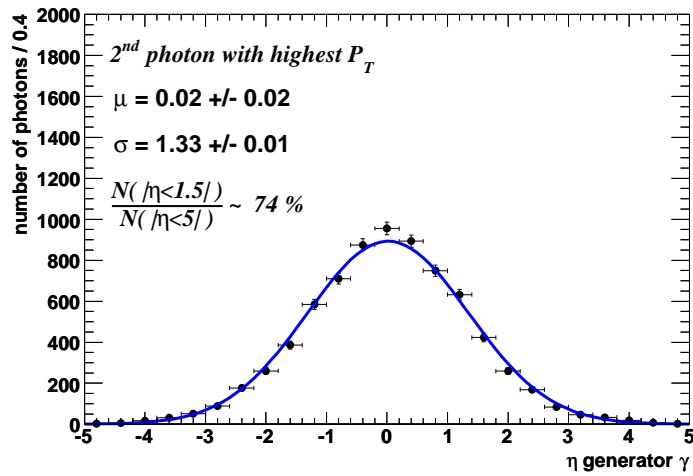
(b)

Figure 4.3: Distribution of η of the first (a) and the second (b) highest transverse momentum photon of the event for the signal sample *GMSB_L140_ctau0.*

Secondary quarks (and jets) with a softer P_T spectrum can be produced in all SUSY events, mostly by hadronic decays of W/Z bosons and τ leptons.
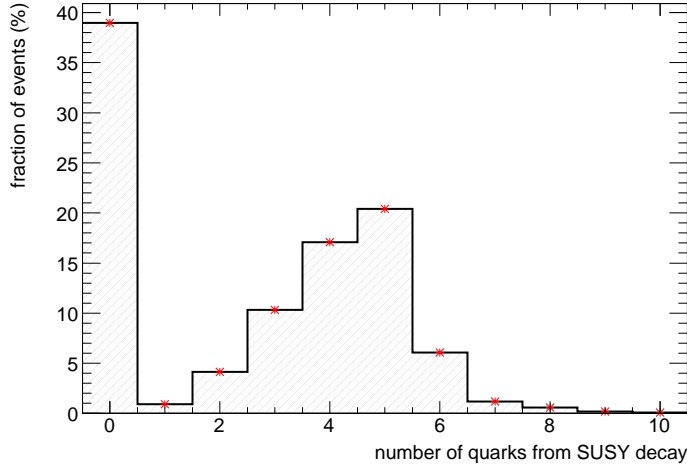
Figure 4.4: Number of quarks from the decay of SUSY particles for the signal sample *GMSB_L140_ctau0*.

4.2.3 Gravitinos and missing energy

The decay of the two neutralinos of a SUSY event produces two gravitinos. Gravitinos are light, stable, neutral and very weakly interacting, and hence they escape from direct detection, creating an imbalance of the transverse energy in the event. The missing transverse energy due to the two gravitinos (*grav*1 and *grav*2 in the formula below) is defined as

$$\not{E}_\text{T}^{grav} = \sqrt{(\text{E}_x^{grav1} + \text{E}_x^{grav2})^2 + (\text{E}_y^{grav1} + \text{E}_y^{grav2})^2} \tag{4.6}$$

where $\text{E}_x(\text{E}_y)$ is the $x(y)$ component of the gravitino momentum. The distribution of $\not{E}_\text{T}^{grav}$ for the signal sample *GMSB_L140_ctau0* is shown in figure 4.6. Thus, large reconstructed missing transverse energy ($\not{E}_\text{T}$) is expected in GMSB events.
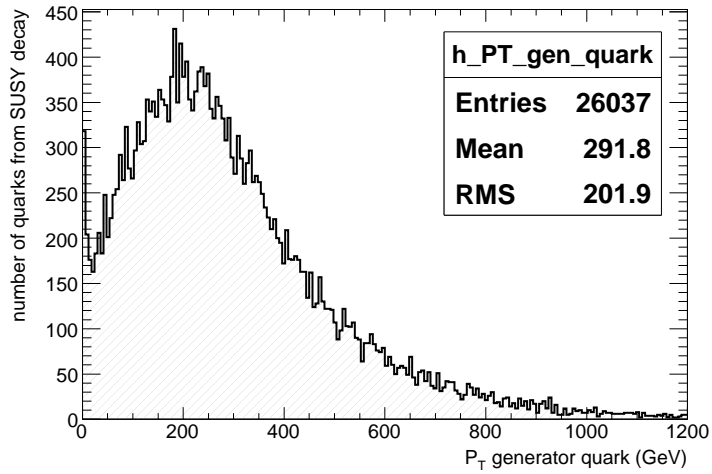
(a)

(b)
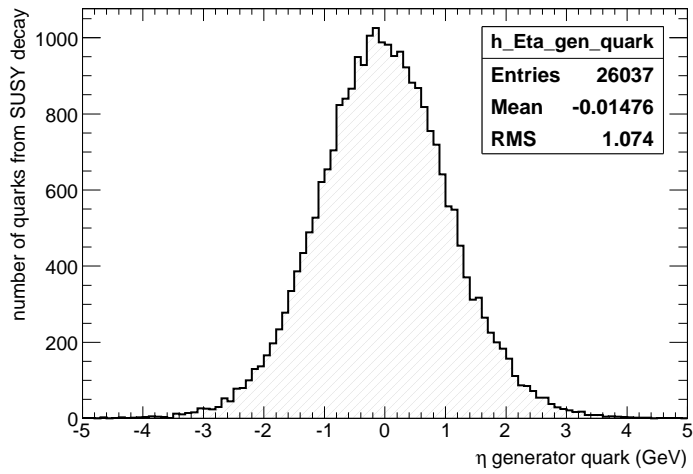
Figure 4.5: P_T(a) and η (b) distributions of quarks at generator level from the decay of SUSY particles for the signal sample *GMSB_L140_ctau0*.
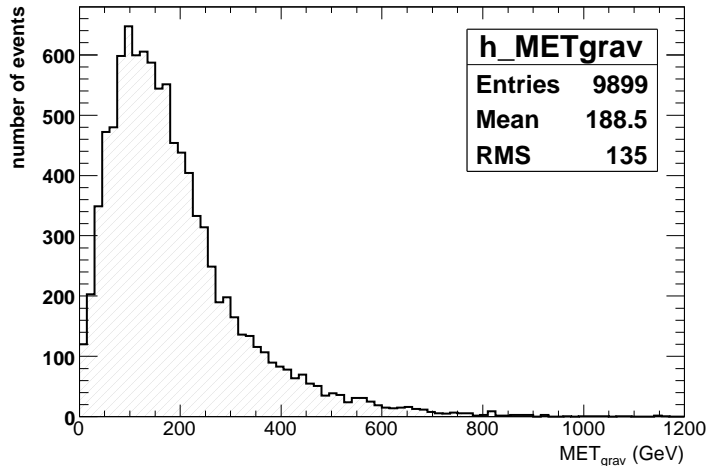
Figure 4.6: Distribution of missing transverse energy at the generator level carried away by the two gravitinos $\displaystyle{\not}{E}_{\mathrm{T}}^{grav}$ for the signal sample *GMSB_L140_ctau0*.

4.3 Sources of background

In this section the main backgrounds to SUSY events are discussed. Irreducible SM backgrounds, i.e. events with substantial $\displaystyle{\not}{E}_{\mathrm{T}}$ and two high P_T photons, are negligible. Furthermore there are no other SUSY processes that can mimic the experimental signature of $\tilde{\chi}_1^0 \to \tilde{\mathrm{G}}\gamma$ decay. The main backgrounds are instead reducible and arise from SM processes with misidentified photons and/or mismeasured $\displaystyle{\not}{E}_{\mathrm{T}}$. They can be divided in two different categories depending on the nature of $\displaystyle{\not}{E}_{\mathrm{T}}$ in the event:

QCD background - processes with no inherent $\displaystyle{\not}{E}_{\mathrm{T}}$

- QCD multi-jets
- direct photon production

ElectroWeak (EW) background - processes with intrinsic $\displaystyle{\not}{E}_{\mathrm{T}}$

- $t\bar{t}$
- $W + \mathrm{jet}$
- $Z + \mathrm{jet}$

- W + γ
- Z + γ
- WW, WZ, ZZ

The first category involves backgrounds with real/fake photons and fake $\not{E}_T$ due to detector mis-measurement; the second involves backgrounds with real/fake photons as well, while $\not{E}_T$ arise mostly from neutrinos produced by W and Z boson decays.

4.3.1 QCD background

QCD multi-jet events

QCD jet events represent the background with the largest total cross section for this analysis. Jets are produced by the hadronization of light quarks and gluons through the following processes:

- $q^i q^j \rightarrow q^i q^j$, $q^i \bar{q}^i \rightarrow q^j \bar{q}^j$, $q^i \bar{q}^i \rightarrow gg$

- $q^i g \rightarrow q^i g$, $gg \rightarrow q^i \bar{q}^i$, $gg \rightarrow gg$

- semi-hard interactions between the partons of incoming protons

where q^i is a generic light quark and $\imath$, $\jmath$ are different flavours of the quark. This symbols will be used also in the following sections.

Figure 4.7 shows the Feynman diagrams for two of these processes at the leading order: $q^i \bar{q}^i \rightarrow q^i \bar{q}^i$ and $gg \rightarrow gg$.

All these interactions are two body processes described at the tree-level with a cross section proportional to α_S^2. For the generation of Monte Carlo samples, no higher-order loop corrections are explicitly included in PYTHIA calculation. Nevertheless, multi-jet events can be generated by adding initial- and final-state QCD radiation through the PYTHIA parton shower evolution [52]. Figure 4.8 shows an example of initial- and final-state QCD radiation in the process $q^i \bar{q}^i \rightarrow q^i \bar{q}^i$.

QCD jet events are a background due to presence of fake reconstructed photons and fake $\not{E}_T$. A high energy $\pi^0 \rightarrow \gamma\gamma$, when isolated from charged particles inside a jet, can mimic the signature of a signal photon. QCD events have no intrinsic $\not{E}_T$ because neutrino production is suppressed. Anyway, a large reconstructed $\not{E}_T$ is possible mostly because of mis-reconstructed energy in the calorimeters, and energy lost in the detector cracks.
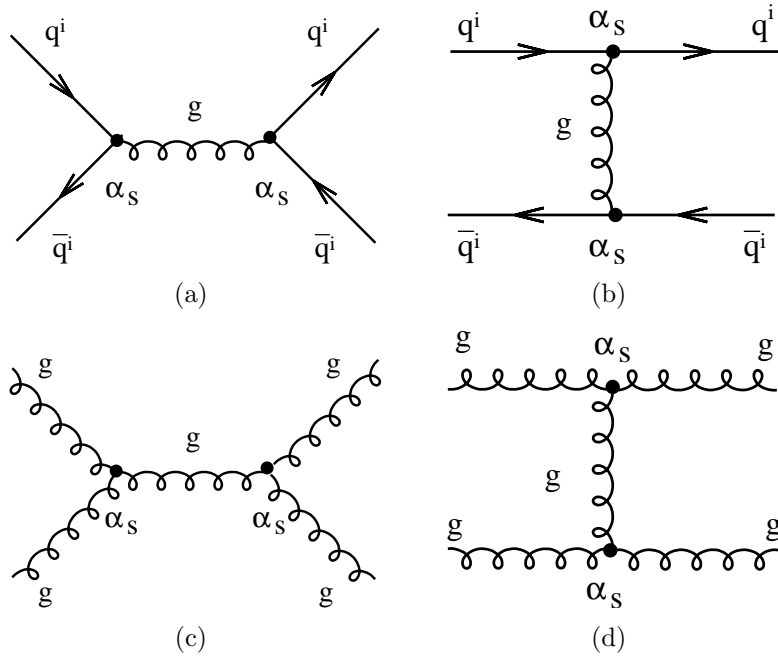
Figure 4.7: Feynman diagrams at the tree level of the QCD process $q^i\bar{q}^i \to q^i\bar{q}^i$ in the s-channel (a) and the t-channel (b) and of the QCD process $gg \to gg$ in the s-channel (c) and the t-channel (d).
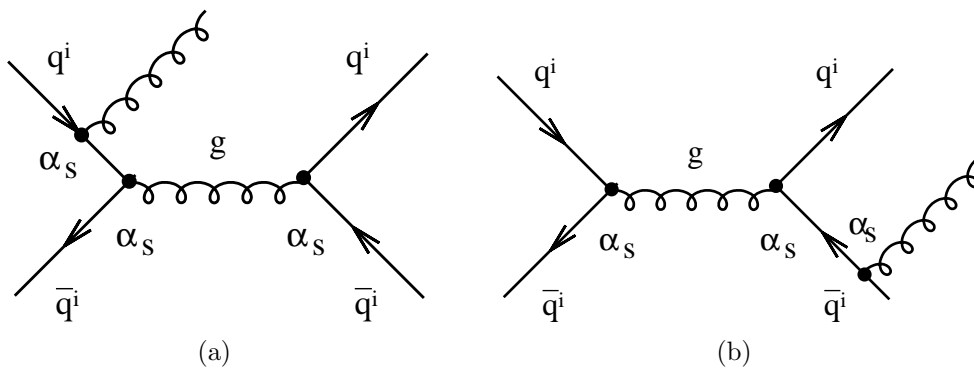
Figure 4.8: Initial- (a) and final-state (b) QCD radiation in the process $q^i\bar{q}^i \to q^i\bar{q}^i$.

70

QCD jet events generated in a wide $\hat{P}_T$[1] range are used for this analysis; the event sample size for each range, the cross section σ at leading order and the relative equivalent integrated luminosity $\mathcal{L}_{int}^{eq}$ are reported in table 4.2.

Direct photon production

QCD events with a direct photon production are described by the following processes:

- $q^i \bar{q}^i \rightarrow g\gamma$, $gg \rightarrow g\gamma$, $q^i g \rightarrow q^i \gamma$

- $gg \rightarrow \gamma\gamma$, $q^i \bar{q}^i \rightarrow \gamma\gamma$

In this work, both single- and double-photon production will be identified with the acronym "γ+jet".

At the LHC, $q^i g \rightarrow q^i \gamma$ and $q^i \bar{q}^i \rightarrow g\gamma$ are the main source of single-γ production. For γ-pair production the dominant processes is $gg \rightarrow \gamma\gamma$. Feynman diagrams for the processes $q^i g \rightarrow q^i \gamma$ and $gg \rightarrow \gamma\gamma$ are shown in figure 4.9. Another possible source of photons is the bremsstrahlung of incoming or outgoing quarks (see the example in figure 4.10), implemented in PYTHIA through the parton shower evolution [52].

(a)   (b)
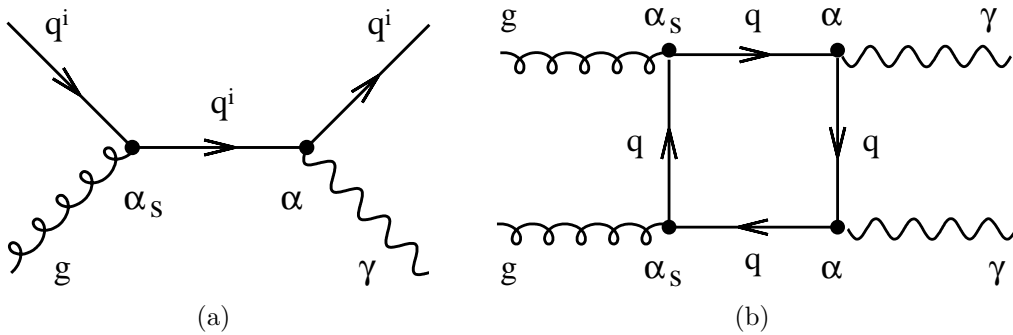
Figure 4.9: Feynman diagrams of the direct photon production processes $q^i g \rightarrow q^i \gamma$ (a) and $gg \rightarrow \gamma\gamma$ (b).

The γ+jet events represent an important background because of the presence of one or two real prompt photons in the final state; fake photons are produced by isolated $\pi^0 \rightarrow \gamma\gamma$ from the quark and gluon hadronization, Fake $\not{E}_T$ is also expected, due to the same resolution effects discussed for the QCD multi-jet events.

---

[1]See definition at section 3.4
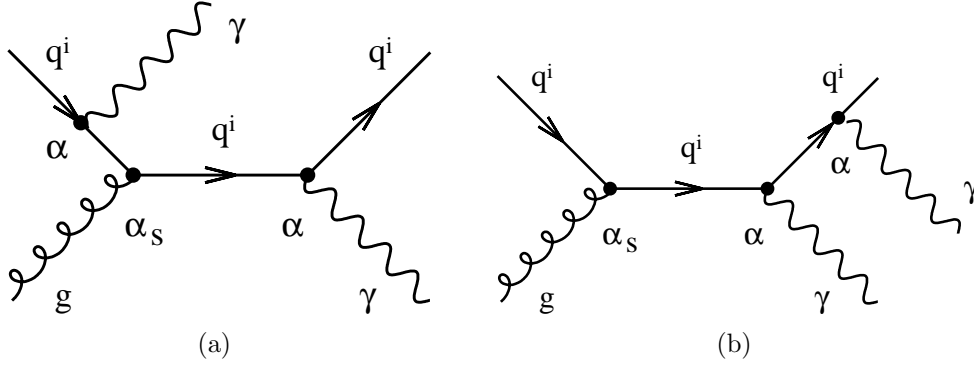
Figure 4.10: Initial- (a) and final-state (b) radiation in the process $q^i g \to q^i \gamma$.

Monte Carlo samples with $\hat{P}_T > 40$ GeV are used for this analysis because, for lower $\hat{P}_T$ values, the low energy photons produced do not contribute to the fake photon rate; the event sample size, the cross section σ at leading order and the equivalent integrated luminosity are reported in table 4.2.

4.3.2 ElectroWeak (EW) background

$t\bar{t}$ background

Given the large cross section at LHC (≈ 800 pb) compared to the signal one, the production of $t\bar{t}$ pairs is one of the dominant reducible backgrounds of this analysis. The $t\bar{t}$ events are mainly produced through the following processes:

- $gg \to t\bar{t}$

- $q^i \bar{q}^i \to t\bar{t}$

The relative Feynman diagrams at the leading order are shown in figure 4.11. The top quark decays nearly 100% of the times in into a W boson and a b quark.

Most of fake photons come from mis-measured electrons (where track reconstruction has failed) produced in the leptonic decays of W boson. Isolated $\pi^0 \to \gamma\gamma$, produced by the hadronization of light quarks from hadronic W decays, give another small contribution to fake photon rate. Large $\not{E}_T$ is due to high energy neutrinos produced by leptonic W decays with a branching ratio of $BR(W \to l\nu) \sim 30\%$.

Dataset name	N_{gen}	σ (fb)	$\mathcal{L}^{eq}_{int}$ (fb)$^{-1}$
QCD jets background			
qcd_30_50	90000	1.56e+11	$5.7 \cdot 10^{-7}$
qcd_50_80	195000	2.09e+10	$9.3 \cdot 10^{-6}$
qcd_80_120	289000	2.95e+09	$9.8 \cdot 10^{-5}$
qcd_120_170	290000	4.99e+08	$5.8 \cdot 10^{-4}$
qcd_170_230	370000	1.01e+08	$3.6 \cdot 10^{-3}$
qcd_230_300	392500	2.38e+07	$1.6 \cdot 10^{-2}$
qcd_300_380	294000	6.38e+06	$4.6 \cdot 10^{-2}$
qcd_380_470	198500	1.89e+06	0.1
qcd_470_600	197250	6.90e+05	0.3
qcd_600_800	98000	2.02e+05	0.5
qcd_800_1000	96750	3.57e+04	2.7
qcd_1000_1400	9800	1.08e+04	0.9
qcd_1400_1800	44250	1.05e+03	42
qcd_1800_2200	32750	1.45e+02	226
qcd_2200_2600	5000	2.38e+01	210
qcd_2600_3000	2500	4.28e+00	584
qcd_3000_3500	990	8.40e-01	1180
qcd_3500_4000	480	9.70e-02	4950
γ+jet background			
gj_bg40	94000	6.19e+07	$1.5 \cdot 10^{-3}$

Table 4.2: Number of generated events N_{gen}, the cross section σ at leading order and the relative equivalent integrated luminosity $\mathcal{L}^{eq}_{int}$ for the QCD background samples in different $\hat{P}_T$ bins.

Figure 4.11: Feynman diagrams at the leading order for the process $gg \to t\bar{t}$ in the s-channel (a) and the t-channel (b) and for the process $q'\bar{q}' \to t\bar{t}$ (c).

Leptonic and semi-leptonic decays of B hadrons, produced by the hadronization of the b quarks, give a small contribution to the fake photon rate and to the $\not{E}_T$ of the event, because of the softer P_T spectrum of the decay products.

All W decays are allowed in the generation of $t\bar{t}$ events; the event sample size, the cross section σ at leading order and the relative equivalent integrated luminosity are reported in table 4.3.

W+jet and Z+jet background

The production of W+jet and Z+jet events is another major reducible background. W+jet and Z+jet events are produced through the following main processes:

- $q^i g \to q^j W \quad , \quad q^i \bar{q}^j \to gW$

- $q^i g \to q^i Z \quad , \quad q^i \bar{q}^i \to gZ$

Feynman diagrams of these processes at the leading order are shown in figure 4.12 and 4.13, respectively for W+jet and Z+jet production.
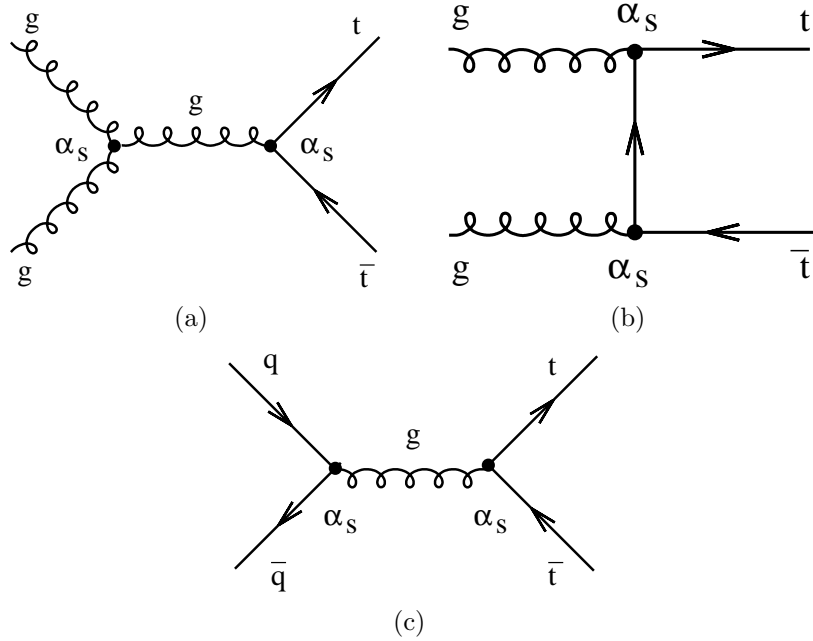
Figure 4.12: Feynman diagrams at the leading order for the process $q^i g \rightarrow q^j W$ in the s-channel (a) and in the t-channel (b), and for the process $q^i \bar{q}^j \rightarrow g W$ (c).

W+jet and Z+jet events can be a background due to presence of fake photons and real $\not{E}_T$.

For the W+jet background, fake photons come from mis-measured electrons (where track reconstruction has failed), or from isolated $\pi^0 \rightarrow \gamma\gamma$, produced by hadronic W decays and by the hadronization of gluons and quarks of the hard process. Real $\not{E}_T$ is due to the high energy neutrinos produced in $W \rightarrow l\nu$ decays.

In the Z+jet events, fake photons come from the mis-measured electrons in $Z \rightarrow e^+e^-$ decays and from high energy $\pi^0 \rightarrow \gamma\gamma$ isolated from jets. Real $\not{E}_T$ can be produced by the $Z \rightarrow \nu\nu$ decays.

The W+jet and Z+jet events generated in a wide $\hat{P}_T$ range are used for this analysis; the event sample size for each range, the cross section σ at leading order and the relative equivalent integrated luminosity $\mathcal{L}_{int}^{eq}$ are reported in table 4.3.

Dataset name	N_{gen}	σ (fb)	$\mathcal{L}^{eq}_{int}$ (fb)$^{-1}$
$t\bar{t}$ background			
$t\bar{t}$ inclusive	2233500	4.92e+05	4.5
W+jet background			
Wjets_0_20	360000	1.11e+08	$3.2 \cdot 10^{-3}$
Wjets_20_50	510000	2.73e+07	$1.9 \cdot 10^{-2}$
Wjets_50_85	760000	1.01e+07	$7.5 \cdot 10^{-2}$
Wjets_85_150	548000	4.30e+06	0.1
Wjets_150_250	278000	1.20e+06	0.2
Wjets_250_400	179000	2.63e+05	0.7
Wjets_400_700	97000	4.88e+04	2
Wjets_700_1100	77000	4.89e+03	15.7
Wjets_1100_1600	48750	5.91e+02	82.5
Wjets_1600_2200	18750	8.27e+01	227
Z+jet background			
Zjets_0_20	196000	3.16e+07	$6.2 \cdot 10^{-3}$
Zjets_20_50	286000	5.16e+06	$5.5 \cdot 10^{-2}$
Zjets_50_85	390000	1.45e+06	0.3
Zjets_85_150	283500	5.76e+05	0.5
Zjets_150_250	147000	1.62e+05	0.9
Zjets_250_400	98000	3.66e+04	2.7
Zjets_400_700	49000	6.97e+03	7
Zjets_700_1100	34000	7.13e+02	47.7
Zjets_1100_1600	20000	8.50e+01	235
Zjets_1600_2200	9750	1.18e+01	826

Table 4.3: Number of generated events N_{gen}, the cross section σ at leading order and the relative equivalent integrated luminosity $\mathcal{L}^{eq}_{int}$ for the Electro-Weak (EW) background samples in different $\hat{P}_T$ bins.
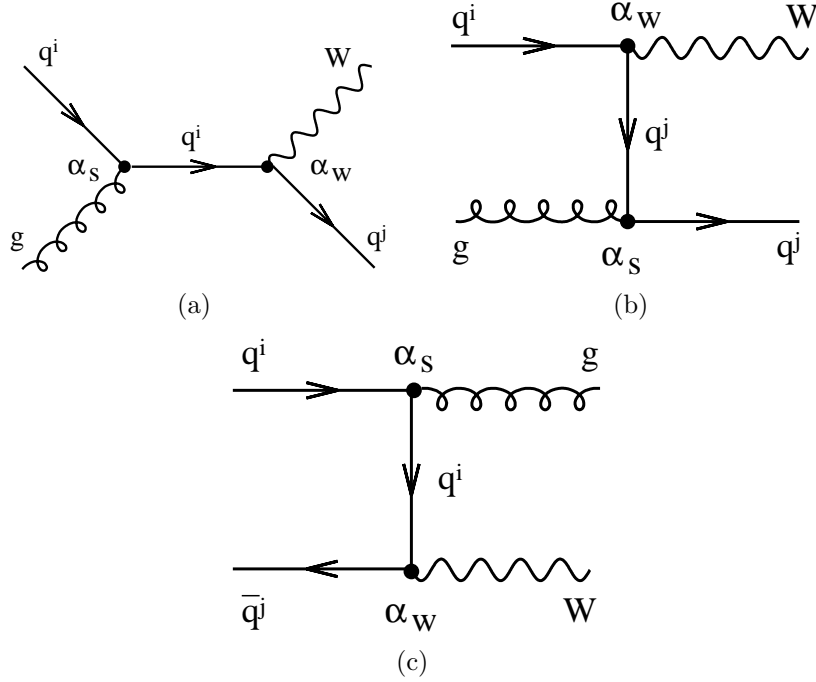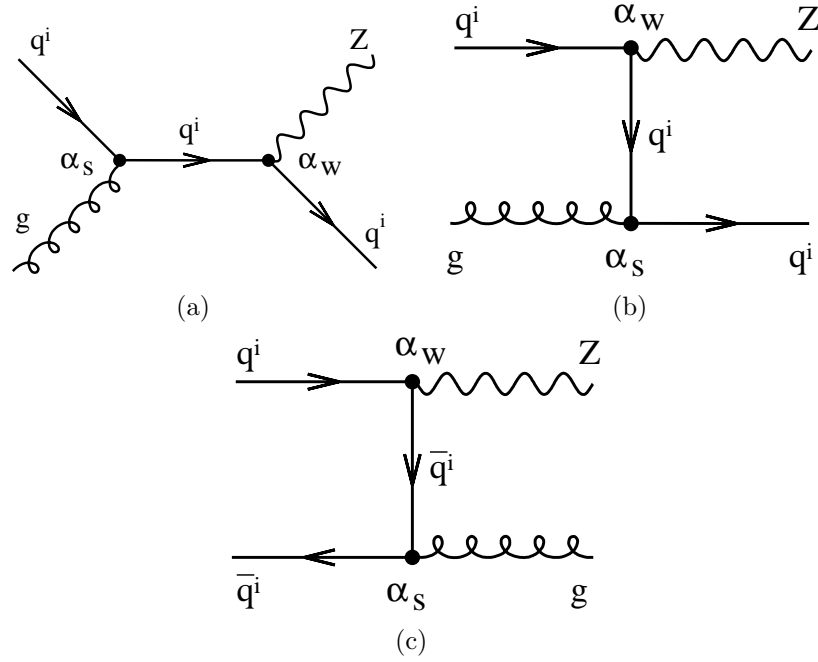
Figure 4.13: Feynman diagrams at the leading order for the process $q^i g \rightarrow q^i Z$ in the s-channel (a) and in the t-channel (b), and for the process $q^i \bar{q}^i \rightarrow gZ$ (c).

4.3.3 Other sources of background

Other sources of background are represented by the processes:

- WW, WZ, ZZ ;

- W+γ, Z+γ .

WW, WZ, ZZ background

Figure 4.14 shows the main Feynman diagrams at the leading order, which describe the tree processes under discussion. Fake photons and real $\not{E}_T$ come, respectively, from mis-reconstructed electrons and neutrinos, produced by both W and Z leptonic decays. For the ZZ production, the s-channel is not possible, since the SM predicts the absence of ZZZ and $ZZ\gamma$ vertexes.

Table 4.4 shows the inclusive cross section at leading order of WW, WZ and ZZ processes, including the $t\bar{t}$ cross section as a reference. It can be noted that WZ and ZZ cross sections are about 10 times smaller than WW
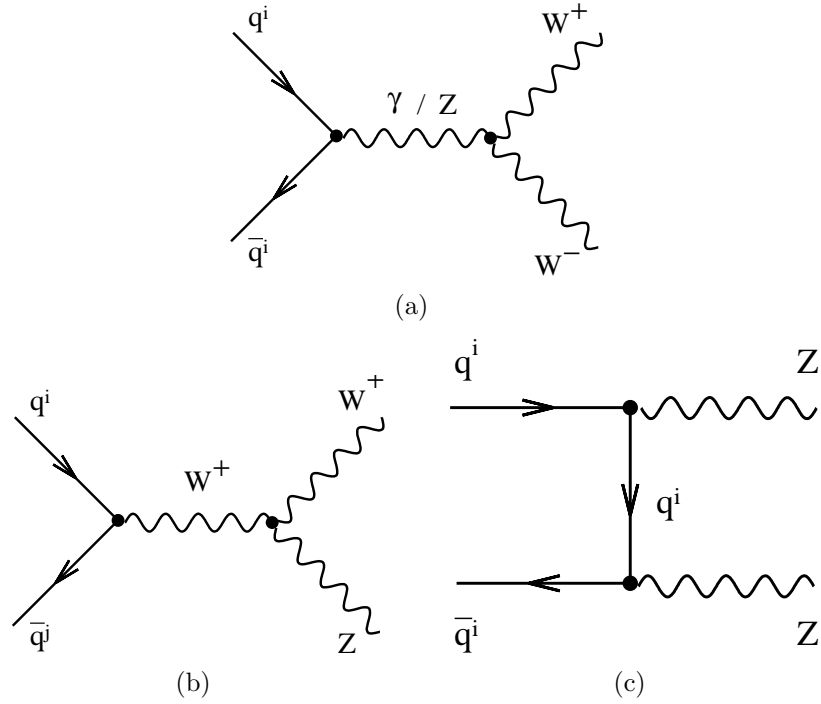
Figure 4.14: Some Feynman diagrams at the leading order for the WW (a), WZ (b) and ZZ (c) processes.

Process	σ (fb)
WW inclusive	$1.9 \; 10^5$
WZ inclusive	$2.7 \; 10^4$
ZZ inclusive	$1.1 \; 10^4$
$t\bar{t}$ inclusive	$8.0 \; 10^5$

Table 4.4: Inclusive cross section σ at the leading order for the production of WW, WZ, ZZ and $t\bar{t}$ processes at the LHC.

one. Thus, the impact of WZ and ZZ processes on this analysis can be neglected with respect to the WW background. The WW cross section is about 4 times smaller than $t\bar{t}$ one. An existing MC study on the search for GMSB using high energy photons [57], indicates that the WW background contamination at high $\not{E}_T$ values is negligible with respect to $t\bar{t}$ events. Nevertheless, since the selection criteria used in [57] are different from the ones applied in this analysis, more detailed studies, with fully simulated events, are needed to understand the impact of WW background after the full selection.

A pair of W bosons can be also produced by the one-loop gluon fusion process, as shown in the Feynman diagrams in 4.15. This process is not included in the generator used to estimate the WW cross section reported in table 4.4. The $gg \rightarrow WW$ cross section is lower than $q\bar{q} \rightarrow WW$ one, because $gg \rightarrow WW$ is not a tree level process. However the P$_T$ of decay products is expected to be larger, as discussed in detail in [58]. For this reason, the $gg \rightarrow WW$ deserves more detailed investigations in future upgrades of the analysis.
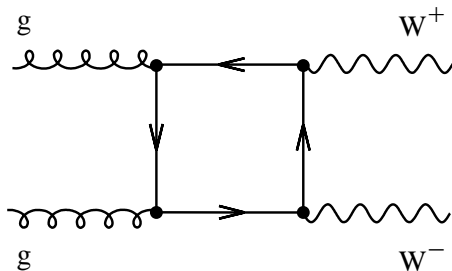
Figure 4.15: A Feynman diagram for the WW production by one-loop gluon fusion

$W+\gamma$ and $Z+\gamma$ background

Figure 4.16 shows two examples of Feynman diagrams at leading order, which describe these tree processes. As diagrams show, the matrix elements of $W+\gamma$ and $Z+\gamma$ processes are proportional to $\alpha_W \times \alpha$. Being purely electroweak processes, they have a cross section suppressed with respect to the $W+$jet and $Z+$jet events, whose matrix elements are of the order $\alpha_W \times \alpha_S$.

The $W+\gamma$ and $Z+\gamma$ events can contribute mainly through the following decay processes

$$pp \quad \rightarrow \quad W\gamma \rightarrow e\nu\gamma \tag{4.7}$$
$$pp \quad \rightarrow \quad Z\gamma \rightarrow e^+e^-\gamma \tag{4.8}$$
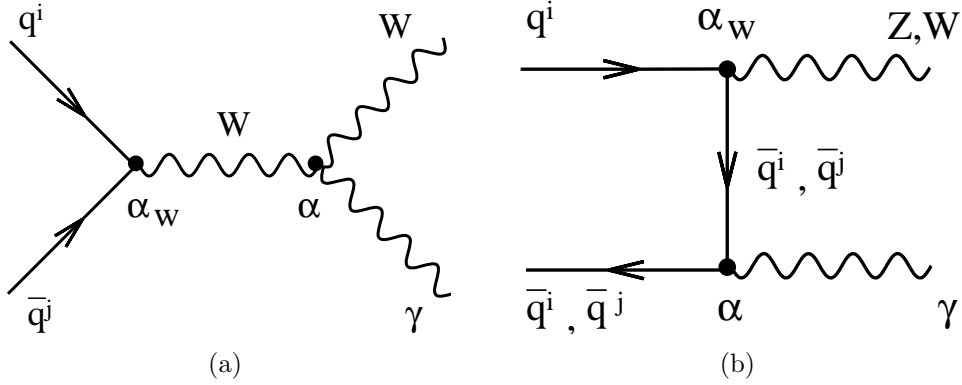
Figure 4.16: Two of the possible tree level diagram for $W+\gamma$ and $Z+\gamma$ events.

where at least one of the electrons from W and Z decays are mis-reconstructed (track reconstruction is failed) and so identified as photons. The event kinematics and the final state are similar to the ones of W+jet and Z+jet background; the main difference consists in the fact that a real photon, instead of a fake one from the jet, is produced.

The cross section σ for these processes at LHC is calculated in the paper [59] and reported in table 4.5. The following acceptance cuts, on the photon transverse momentum P_T^γ, on the transverse momentum of all electrons P_T^{ele}, and, where at least one neutrino is present, on the missing transverse energy P_T^{miss} in the event, are applied in the theoretical calculation: $P_T^\gamma > 50$ GeV ($P_T^\gamma > 100$ GeV) for the $W+\gamma$ ($Z+\gamma$) production, $P_T^{ele} > 20$ GeV, and $P_T^{miss} > 50$ GeV ($P_T^{miss} > 100$ GeV) for the $W+\gamma$ ($Z+\gamma$) production.

Process	σ (fb)	P_T^γ (GeV)	P_T^{miss} (GeV)	P_T^{ele} (GeV)
$pp \to W\gamma \to e\nu\gamma$	≈ 125	50	50	20
$pp \to Z\gamma \to e^+e^-\gamma$	≈ 40	100	-	20

Table 4.5: Cross section σ at the leading order for $W+\gamma$ and $Z+\gamma$ production at the LHC, where high energy leptons and neutrinos are produced from vector boson decays. The acceptance cuts on P_T of decay products, used in the theoretical calculation, is also shown.

With a P_T threshold similar to the one used in the final selection of this analysis (see table 5.3), the cross section of $W+\gamma$ and $Z+\gamma$ events is of the same order of magnitude of the GMSB events ($\mathcal{O}(100-1000)$ fb model dependent).

Since, for this background, the cross section of the processes in equations 4.7 and 4.8 needs to be multiplied for the probability to mis-identify an electron for a photon, the contribution of $W+\gamma$ and $Z+\gamma$ events is expected to be small.

All the background sources discussed in this section have been not included in the background estimates and final sensitivity of this analysis discussed in section 5.7, because the relative samples of fully simulated events was not available. As discussed so far, their impact on the analysis is expected to be small. These samples can be included in future upgrades to have a more detailed description of the background contamination.

4.3.4   Preselection of background events

The background samples used for this study are taken from the official Monte Carlo production of CMS (see section 3.3.7 for details about the software tools used). Since small efficiency is expected for backgrounds, a large number of events need to be processed to have a representative background sample for this analysis.

While signal events have high P_T photons and quarks in the final state, background events have most of the energy of the event deposited at low values of pseudo-rapidity. To save processing time while reconstructing the events and disk space needed to store data, a filter at generator level is applied before the reconstruction process. As detailed so far, most of background events can have a signature similar to the signal because of $e^\pm, \pi^0, \eta$ mis-identified as photons. Then, the filter is based on the selection of events where there is at least one $\gamma, e^\pm, \pi^0, \eta^0$ with $P_T^{gen} > 40$ GeV, being P_T^{gen} the transverse momentum of the particles at generator level. The value of P_T threshold at 40 GeV represents a loose cut compared with the typical photon P_T cut of the analysis (≈ 100 GeV).

Chapter 5

Measurement of the $pp \rightarrow 2\tilde{\mathbf{G}} + 2\gamma + X$ channel

In this chapter, the analysis strategy for the measurement of GMSB $\tilde{\chi}_1^0 \rightarrow \tilde{G}\gamma$ decays is presented. The signal events are characterized by the presence of two high P_T photons, large $\not{E}_T$ due to the two gravitinos and high P_T jets in the final state, as discussed in section 2.5.2. The reducible background is represented by QCD processes (multi-jets and events with direct photon production), and by Electro-Weak (EW) processes, mainly $t\bar{t}$, W+jet and Z+jet events.

The study of the $\tilde{\chi}_1^0 \rightarrow \tilde{G}\gamma$ decay and SM backgrounds using generator level quantities, discussed in chapter 4, is a useful starting point to define a set of reconstructed quantities which discriminate signal from background, e.g. the P_T and the η of the photons and the photon isolation criteria. The selection criteria are optimized, using a multi-dimensional optimization for the selection variables which are correlated. Given that the kinematics of the event and the cross section depend on the parameter Λ of GMSB model, the optimization is performed for different Λ values.

Since the $\not{E}_T$ is the most discriminating variable between signal and background, the $\not{E}_T$ distribution is used to extract the signal yield using a maximum likelihood fit and it is not included in the selection. This approach, compared to a cut&count technique, offers the advantages that the systematics can be taken into account in the modeling of the $\not{E}_T$ shapes, which can be obtained directly from data using control samples. In addition, the background normalization is extracted from the fit itself.

This chapter is organized as follows:

- the description of the reconstructed photons used in this analysis is presented in section 5.1;

- the effect of converted photons on this analysis is discussed in section 5.2;

- the missing transverse energy reconstruction is discussed in section 5.3;

- the jet reconstruction is discussed in section 5.4;

- the event selection using reconstructed object is discussed in section 5.5;

- the determination of signal and background yields by using a likelihood fit to the $\not{E}_T$ distribution of selected events is described in section 5.6.;

- the result of the signal extraction is presented in section 5.7;

- the background estimate from the data is discussed in section 5.8.

5.1 Photon reconstruction

5.1.1 Monte Carlo truth matching

A simple algorithm is used to match reconstructed photons with a generator photons. Three quantities are used: the energy, the pseudorapidity and the coordinate of the photons.

A reconstructed photon is matched with a generator photon if $\Delta R = \sqrt{\Delta\eta^2 + \Delta\phi^2} < 0.2$ and $0.8 < E^\gamma_{reco}/E^\gamma_{gen} < 1.05$, where $\Delta\eta = \eta^\gamma_{reco} - \eta^\gamma_{gen}$, $\Delta\phi = \phi^\gamma_{reco} - \phi^\gamma_{gen}$ and E^γ_{reco} (E^γ_{gen}), η^γ_{reco} (η^γ_{gen}), ϕ^γ_{reco} (ϕ^γ_{gen}) are the energy, the pseudorapidity, and the ϕ coordinate of the reconstructed (generator) photon, respectively. To avoid having more than one associated candidates, the reconstructed candidate with the minimum ΔR, is chosen.

5.1.2 Photon energy and position reconstruction

The photon energy is reconstructed by summing the energy deposited in a cluster of ECAL. Dedicated algorithms, called superclustering algorithms, are used to recover the energy of photons which convert in an e^+e^- pair in tracker material. There are two superclustering algorithms: Hybrid and Island. A short description is outlined in the following. Details are given in [60].

Hybrid - The Hybrid algorithm starts with a search for seeds, i.e. crystals with a transverse energy above 1 GeV. Then, $\phi \times \eta = 1 \times 3$ crystal dominoes are made, each with their central crystal aligned in η with the

seed crystal. If the energy of the central crystal of a domino is greater than 1 GeV, then a 1×5 domino is used. This domino seeking proceeds in ϕ direction up to ± 10 crystals from the original seed. Dominoes with energy less than 0.1 GeV are eliminated. The dominoes within 10 crystal in ϕ are then clustered to form a supercluster. The main motivation is that, due to the magnetic field, the e^+e^- pair from photon conversions is mostly aligned in η, but separated in ϕ. Each distinct cluster of dominoes is required to have a seed domino with energy greater than 0.35 GeV.

Island - The algorithm loops over seeds, crystals with transverse energy above 0.5 GeV, ordered by decreasing energy. Seeds adjacent to higher energy ones are removed. Starting from the most energetic seed position, the algorithm moves in both directions in ϕ and collects all crystals until it sees a rise in the energy, or an empty crystal (hole). The algorithm then moves one step in η and makes another ϕ search (the same procedure is repeated in the opposite η direction). The η-steps are stopped when a rise in energy, or a hole, is encountered. All the collected crystals are marked as belonging to that one cluster and cannot be used anymore. All clusters in a narrow η window along the ϕ direction are collected to form a supercluster.

The Hybrid algorithm is used in the barrel and the Island algorithm in the endcaps. The position of the impact point of the photon is obtained by calculating the energy mean position of the crystals in the supercluster using log weights.

Figure 5.1 shows the distributions of the ratio $E^{\gamma}_{reco}/E^{\gamma}_{gen}$, for barrel and endcaps. The distribution is fitted with a "Crystal Ball" probability density function

$$f_{CB}(x; \alpha, n, \mu, \sigma) \;=\; N \cdot \left\{ \begin{array}{ll} exp\left(\frac{-(x-\mu)^2}{2\sigma^2}\right), & \text{for} \quad \left|\frac{x-\mu}{\sigma}\right| < \alpha \\ A \cdot \left(B - \frac{x-\mu}{\sigma}\right), & \text{for} \quad \left|\frac{x-\mu}{\sigma}\right| \geq \alpha \end{array} \right. \quad (5.1)$$

where

$$A \;=\; \left(\frac{n}{|\alpha|}\right)^n \cdot exp\left(-\frac{|\alpha|^2}{2}\right)$$

$$B \;=\; \frac{n}{|\alpha|} - |\alpha|.$$

N is a normalization factor while μ, σ, n and α are parameters which are fitted with to the data. The relative width of the Gaussian component of the

distribution is $\sigma/\mu \sim 0.7 - 0.8\%$ both for the barrel and the endcaps; these values are compatible with the design energy resolution expected for high energy photons measured by ECAL (see section 3.3.2). Both the 3 % shift in the mean μ and the tail in the distribution are caused by energy losses in the clustering process. No correction is applied on the supercluster energy since such a shift in the global photon energy scale is not relevant for this analysis.

5.1.3 Photon isolation criteria

A photon can be considered isolated when there is small hadronic activity around it. In this analysis, isolation requirement, based on both tracker and calorimetry measurements, is one of the most important tools to reduce the background to prompt photons, both at trigger level (see section 5.5.1) and at offline analysis level. In signal events ($\tilde{\chi}_1^0 \to \tilde{G}\gamma$), the two photons are isolated whereas, in the reducible background processes (such as $pp \to$ jets and $pp \to \gamma +$ jet), at least one of the reconstructed photon is a π^0 which is produced in a jet and, in general, it is not well isolated. In a jet, these reconstructed high E_T electromagnetic showers are usually close to additional particles. These charged pions and kaons can be detected in the tracker. The hadron calorimeter offers an information that is partially redundant with the tracker measurements; in fact charged pions and kaons measured in the tracker will deposit relevant fraction of their energy in HCAL. It is also important to detect charged particles which are not efficiently reconstructed in the tracker (in particular at high η), or neutral hadrons like neutrons or K_L^0.

The two isolation variables used in this analysis are described in the following.

$\sum \mathbf{P}_T^{trk}$ - The scalar sum of the P_T of the reconstructed tracks inside a cone of size $\Delta R = 0.3$ around the photon supercluster. Tracks are reconstructed using the Combinatorial Track Finder algorithm [29].

$\mathbf{H/E}$ - The ratio between the HCAL energy (H) in the tower immediately behind the supercluster and the ECAL supercluster energy (E).

Figure 5.2 shows that these isolation variables have a good discriminating power between the signal and the background.

5.1.4 Photon cluster shape

The transverse shape of the cluster can be used to discriminate between signal photons and background isolated $\pi^0 \to \gamma\gamma$, that represent an important
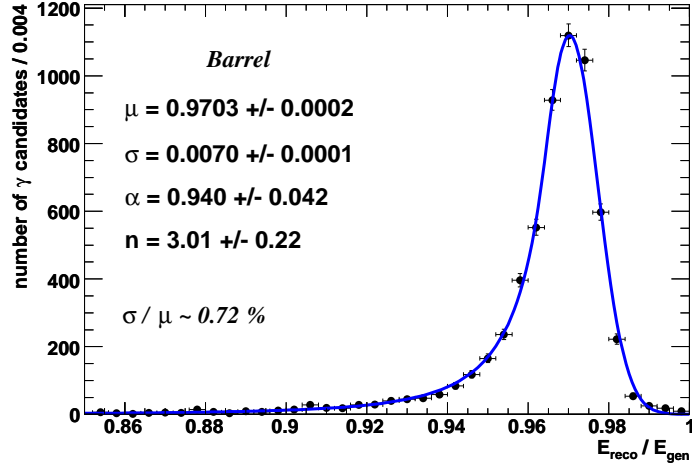
(a)
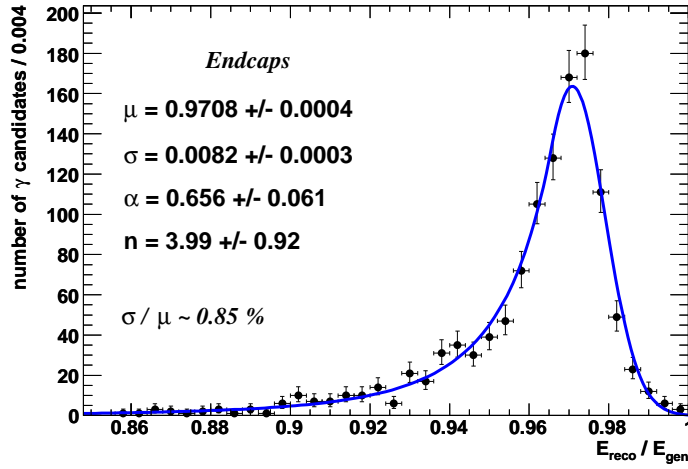
(b)

Figure 5.1: Distributions of the ratio between the reconstructed photon energy (E^{γ}_{reco}) and the energy of matched generator photons (E^{γ}_{gen}) of the signal sample *GMSB_L140_ctau0*, for both the barrel (a)) and the endcaps(b). Fit results using a "Crystal Ball" function (see equation 5.1) are superimposed. Single photon HLT selection, described in section 5.5.1, is applied.
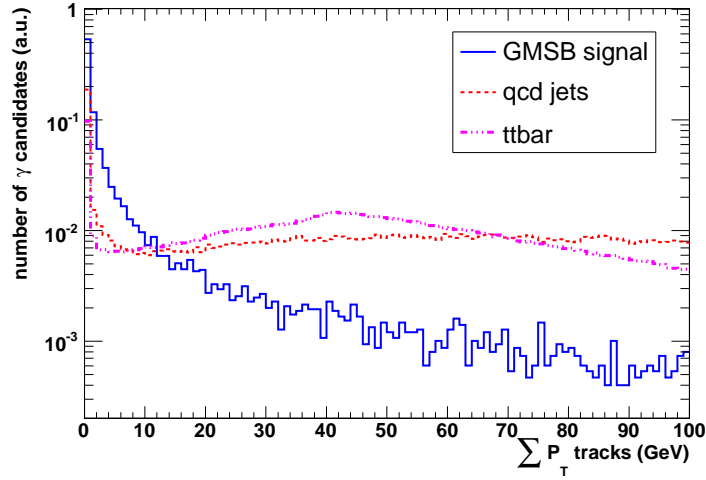
(a)
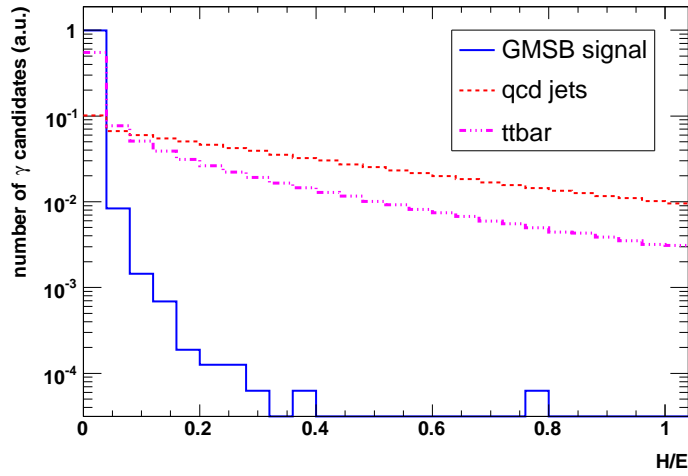
(b)

Figure 5.2: The distributions of the photon isolation variables $\sum P_T^{trk}$ (a) and H/E (b) for signal and background photon candidates. For backgrounds, all superclusters with $P_T > 20$ GeV are considered. The samples *GMSB_L140_ctau0*, *qcd_jet_470_600* and $t\bar{t}$ *inclusive* have been used, respectively, for the GMSB signal, the qcd jets and the $t\bar{t}$ background.

contribution to the fake photon rate. The lateral profile of the energy deposit in ECAL is narrow for photons and symmetric with respect to the impact point, while an isolated π^0 decaying to photons is characterized by two close electromagnetic energy deposits and no reconstructed tracks in front of them. The energy deposit of a π^0 is therefore distributed along many ECAL crystals and the shape of the energy deposits is eccentric. The major axis connects the positions of the two photons from π^0 decay when hitting the ECAL surface. The minimum angular separation θ_{12}^{min} between photons from π^0, which is also the one with the largest probability to occur, is

$$\theta_{12}^{min} = \arctan\left(\frac{2m_{\pi^0}}{\sqrt{E_{\pi^0}^2 - m_{\pi^0}^2}}\right) \tag{5.2}$$

where E_{π^0} (m_{π^0}) is the energy (mass) of the π^0. For high energy candidates the two signatures (γ and $\pi^0 \to \gamma\gamma$) are very similar because θ_{12}^{min} decreases with the increasing π^0 energy and the two photons are almost collinear.

The spatial distribution of the energy deposit in the ECAL can be characterized by the covariance matrix [61]

$$COV_{\phi\eta} = \begin{pmatrix} S_{\phi\phi} & S_{\phi\eta} \\ S_{\eta\phi} & S_{\eta\eta} \end{pmatrix} \tag{5.3}$$

where

$$S_{\mu\nu} = \frac{1}{E_\gamma} \sum_{i=1}^{N} E_i \cdot (\mu_i - \langle\mu\rangle) \cdot (\nu_i - \langle\nu\rangle) \quad . \tag{5.4}$$

The value N is the number of crystals associated to the photon candidate, μ and ν indexes represent the ϕ and η coordinates of the cluster, E_i is the energy deposited in the crystal i, $E_\gamma = \sum_{i=1}^{N} E_i$ and $\langle\mu\rangle = \sum_{i=1}^{N} \mu_i \cdot E_i/E_\gamma$ (the same for $\langle\nu\rangle$). The covariance matrix is diagonalized, which is equivalent to finding the major and minor axes of the energy deposit ellipse, using the following relation

$$COV_{\phi'\eta'} = \begin{pmatrix} S_{major} & 0 \\ 0 & S_{minor} \end{pmatrix} \tag{5.5}$$

where

$$
\begin{aligned}
S_{major} &= \frac{S_{\phi\phi} + S_{\eta\eta} + \sqrt{(S_{\phi\phi} - S_{\eta\eta})^2 + 4S_{\phi\eta}^2}}{2} \\
S_{minor} &= \frac{S_{\phi\phi} + S_{\eta\eta} - \sqrt{(S_{\phi\phi} - S_{\eta\eta})^2 + 4S_{\phi\eta}^2}}{2}
\end{aligned}
$$

The energy deposit can be characterized by the cluster shape asymmetry Δ defined as

$$\Delta = \frac{S_{major} - S_{minor}}{S_{major} + S_{minor}} \qquad (5.6)$$

5.2   Study on converted photons

A large number of photons originating from the primary interaction vertex converts in an e^+e^- pair in the tracker material ($\sim 40\%$ of photons). Figure 5.3 shows the amount of material budget in front of the ECAL. The study described in this section is devoted to quantify the effect of converted photons on this analysis, in terms of energy resolution and reconstruction efficiency.

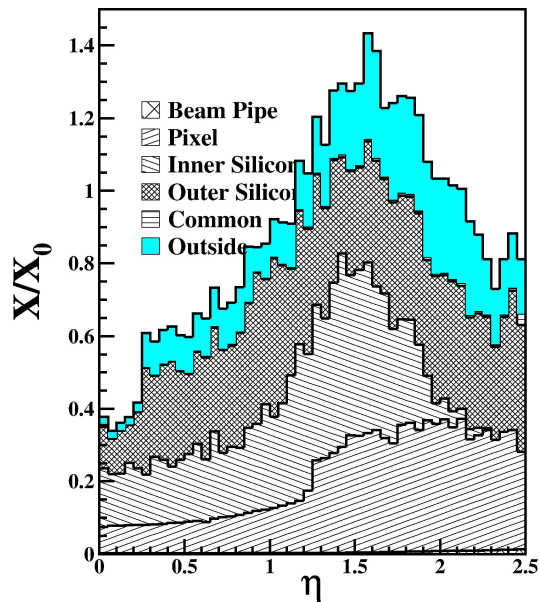Figure 5.3: Amount of material (in radiation length X_0) in front of the ECAL, including that for tracker material, the beam pipe, the support structure and the cables, as a function of pseudo-rapidity [30].

The electron and the positron generated by the photon conversion are bent by the magnetic field and they can deposit their electromagnetic energy in different ECAL regions. If the separation between them is large enough,

two clusters are reconstructed. Thus, the cluster with the highest energy is associated to the initial single photon. As a result, the photon energy resolution is degraded because part of the energy is carried away by the other cluster.

Given the large P_T of the photons from neutralino decay (see figure 4.2), the e^+e^- pair is not very separated because of the large Lorentz boost. In this case, superclustering algorithms almost completely recover the energy of converted photons. In the ECAL barrel, the distribution of $E_{reco}^\gamma/E_{gen}^\gamma$ does not differ significantly between converted and unconverted signal photons (see figure 5.4 a). In the endcaps, differences in the tails are observed (see figure 5.4 b). The contribution of this effect to the analysis is marginal because only 15% of signal photons fall in the endcaps.

A second effect is that an isolated photon which converts in the tracker material, can be rejected by the isolation criteria if at least one of the two (almost collinear) e^+e^- tracks are reconstructed. If a photon converts in the tracker material far from the pixel layers, no tracks are reconstructed, since the tracking algorithms is designed for prompt tracks originating from primary vertex.

The following quantities are used in this study: the reconstruction efficiency ε_{reco}, defined as the number of reconstructed photons (with or without the isolation requirement applied) matched with a generator photon, divided by the total number of generator photons; the radius R_{conv}, defined as $R_{conv} = \sqrt{x_{conv}^2 + y_{conv}^2}$, where x_{conv} (y_{conv}) is the x (y) position of the simulated conversion vertex in CMS reference system. The following isolation criteria have been used for this study: $\sum P_T^{trk} < 9$ GeV and H/E < 0.1.

The plot in figure 5.5 shows ε_{reco} as a function of radius R_{conv} for photons from the $\tilde{\chi}_1^0$ decay. As expected, without photon isolation, the reconstruction efficiency is very high (about 95%) and independent from R_{conv}. If offline isolation criteria are applied, the efficiency decreases, due to the rejection of photons not well isolated from jets. More interesting is the additional efficiency drop $\delta\varepsilon_{0-25}^{conv} \sim 25\%$ in the R_{conv} range between 0 and 25 cm, compared to the other bins and to the unconverted photons, which are reported in the negative bin of the histogram. This drop is due to the track veto for early converted photons, as discussed above.

An naïve estimate of the total efficiency loss for early conversions is

$$\delta\varepsilon_{tot}^{conv} = \delta\varepsilon_{0-25}^{conv} \times f_{0-25}^{conv} \sim 25\% \times 10\% = 2.5\% \qquad (5.7)$$

where f_{0-25}^{conv} is the fraction of generated photons which convert in the interval 0 cm $< R_{conv} < 25$ cm and correspond to $\sim 10\%$.

In conclusion, a dedicated reconstruction algorithm for converted photon
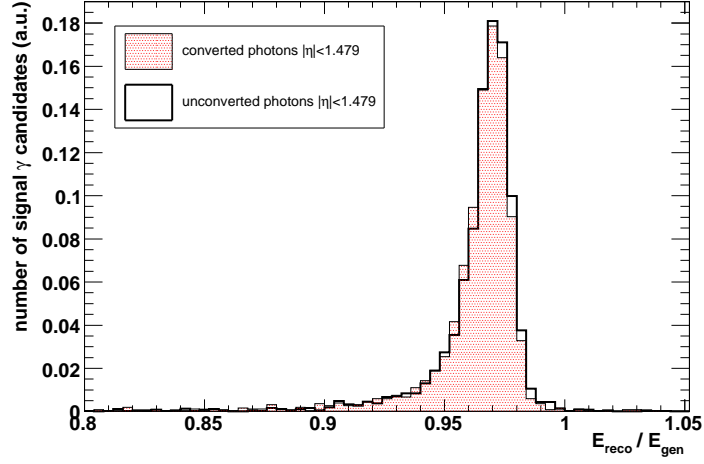
(a) Barrel
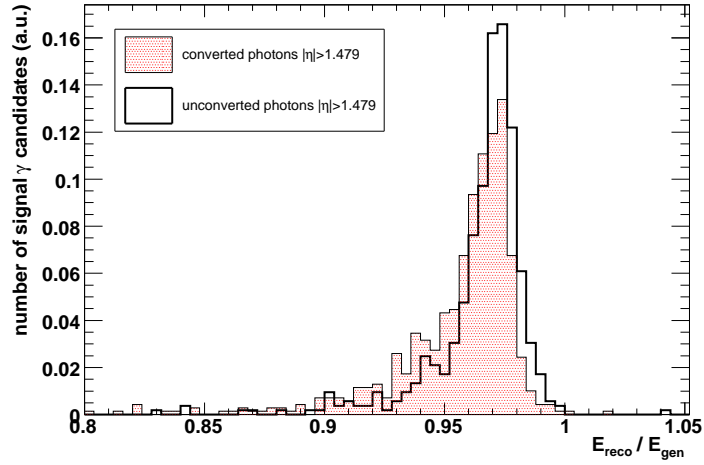
(b) Endcaps

Figure 5.4: The distribution of the ratio between reconstructed energy E^{γ}_{reco} and the true MC energy E^{γ}_{gen} of signal photons in the barrel (a) and in the endcaps (b) for the signal sample *GMSB_L140_ctau0*. The filled (empty) histogram is for converted (unconverted) photons. No photon isolation criteria are applied. Hybrid (Island) algorithm is applied in the barrel (endcaps).
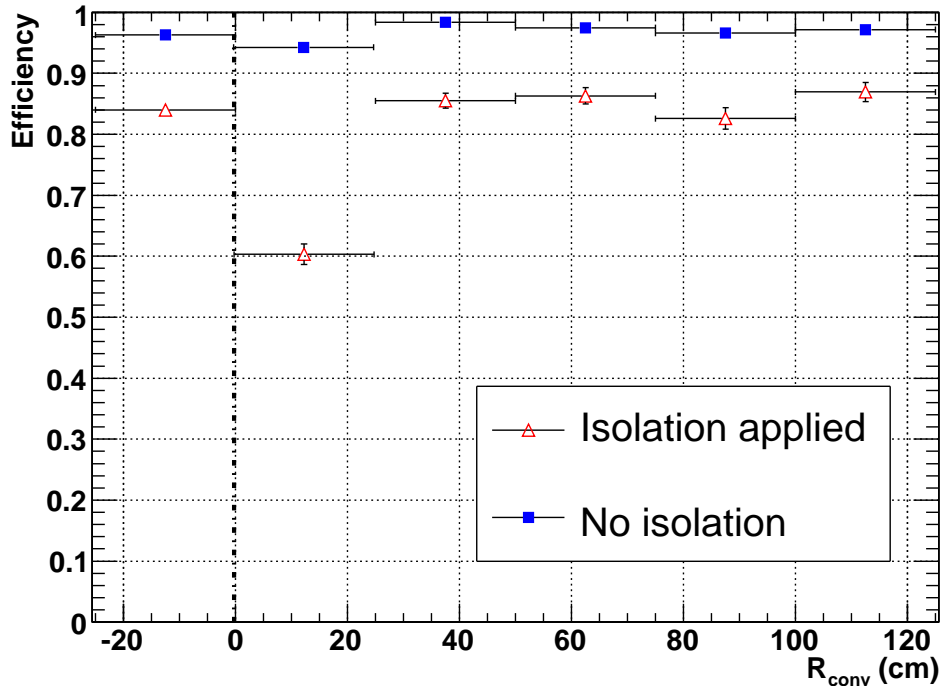
Figure 5.5: Reconstruction efficiency ε_{reco}as a function of conversion radius R_{conv}, with/without offline isolation criteria applied. The negative bin corresponds to the unconverted photons. Single photon HLT selection efficiency is included both in numerator and denominator values for ε_{reco}calculation.

is not used in this analysis, since it cannot significantly improve the energy resolution and the reconstruction efficiency of photons from the $\tilde{\chi}_1^0$ decay.

5.3   Missing Transverse Energy

The CMS detector has been designed to cover as much solid angle as possible with calorimetric detectors, to measure the energy of the visible particles of the event. The total energy balance allows to identity the presence of high energy neutrinos or other weakly-interacting stable particles (such as the gravitino of the GMSB models) through apparent missing energy in the event. While it is not possible to measure the longitudinal component of the missing energy because of the particles falling in the beam pipe, the missing transverse energy can be extracted with a good accuracy.

The missing transverse energy ($\not{E}_{\mathrm{T}}$) is determined from the transverse vector sum over calorimeter towers n having energy E_n, polar angle θ_n and azimuthal angle ϕ_n:

$$\hat{\not{E}}_{\mathrm{T}} = -\sum_n (E_n \sin\theta_n \cos\phi_n \hat{i} + E_n \sin\theta_n \sin\phi_n \hat{j}) = -\not{E}_{\mathrm{x}}\hat{i} + -\not{E}_{\mathrm{y}}\hat{j} \qquad (5.8)$$

where the index n runs over all calorimeter towers and $\hat{i}$ ($\hat{j}$) is the versor of x (y) axis in the CMS reference system [62].

The measurement of $\not{E}_{\mathrm{T}}$ is degraded by the difference between photon and pion response in the combined ECAL plus HCAL system, which is a non compensating calorimeter, and by the bending of low energy tracks by the 4 T magnetic field. On the other hand, the excellent cell segmentation, the hermeticity, and good forward coverage of CMS improve the measurement of $\not{E}_{\mathrm{T}}$. Jet and muon energy corrections are not used in this analysis but will be considered in the future.

The $\not{E}_{\mathrm{T}}$ resolution in CMS is expected to be dominated by calorimeters. For this reason the uncertainty can be parametrized in the following way

$$\sigma_{\not{E}_{\mathrm{T}}} = A\sqrt{\sum \mathrm{E}_T} \oplus B \oplus C \sum \mathrm{E}_T \qquad (5.9)$$

where $\sum \mathrm{E}_T$ is the scalar transverse sum (or total visible E_T) of the event is defined as the scalar sum

$$\sum \mathrm{E}_T = \sum_n E_n \sin\theta_n \qquad (5.10)$$

The A term is due to the statistical sampling of the calorimeters, the B term is due to electronic noise and the constant C term is due to other systematic effects, such as non-linearities, detector cracks and dead material. The current estimate of these parameters, for QCD events, are $A = 0.97$ GeV$^{1/2}$, $B = 3.8$ GeV and $C = 1.2\%$ [63].

In this analysis, the reconstructed ($\not{E}_{\mathrm{T}}$) is calculated using individual calorimeter cells as input objects to the algorithm. The $\not{E}_{\mathrm{T}}$ at generator level ($\not{E}_{\mathrm{T}}^{gen}$) is obtained using the energy of generator level particles, not including the contribution from neutrinos and gravitinos. Figure 5.6 shows the correlation between reconstructed $\not{E}_{\mathrm{T}}$ and generator-level $\not{E}_{\mathrm{T}}^{gen}$ for signal events. The $\Delta\phi = \phi_{\not{E}_{\mathrm{T}}} - \phi_{\not{E}_{\mathrm{T}}^{gen}}$ separation between the reconstructed and the generator-level missing transverse energy vectors is shown in figure 5.7.
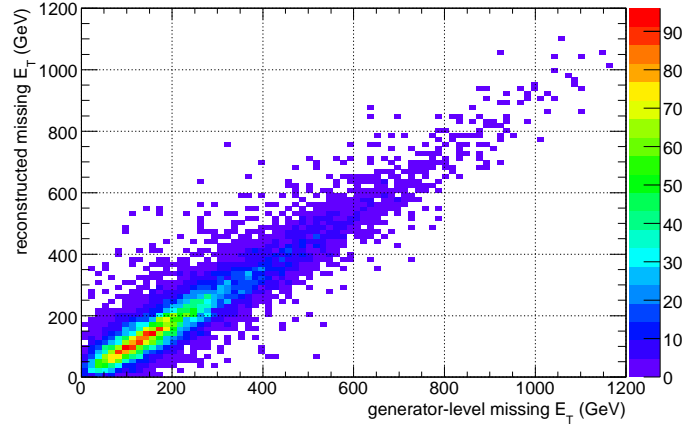
Figure 5.6: Correlation between reconstructed and generator-level missing transverse energy of the event for the signal sample *GMSB_L140_ctau0*.
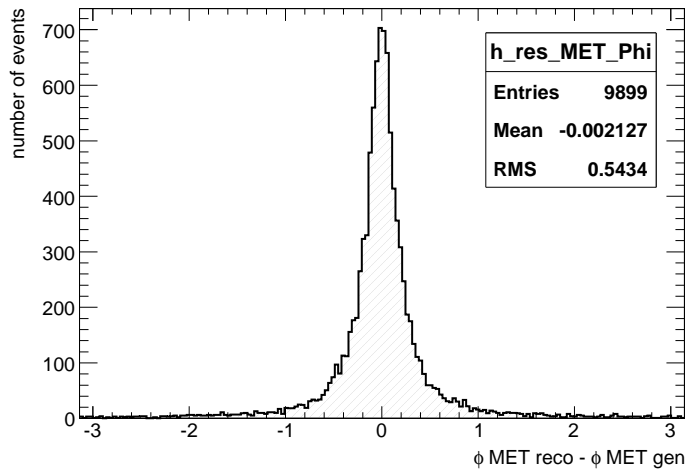

Figure 5.7: Distribution of $\Delta\phi = \phi_{\not{E}_T} - \phi_{\not{E}_T^{gen}}$ angular separation between reconstructed and generator-level missing transverse energy vectors of the event for the signal sample *GMSB_L140_ctau0*.

5.4 Jet reconstruction

5.4.1 Calorimeter towers

The ECAL and HCAL calorimeter towers are used as input for several jet clustering algorithms. Readout cells in HCAL and ECAL are arranged in a tower pattern in η,ϕ space. The cells in the barrel region have a segmentation of $\Delta\eta \times \Delta\phi = 0.087 \times 0.087$ for the HCAL and $\Delta\eta \times \Delta\phi = 0.0174 \times 0.0174$ for the ECAL, becoming progressively larger in the endcaps and forward regions. Since the ECAL granularity is much finer than HCAL, calorimeter towers are formed by adding energy deposits in the (η,ϕ) bins of ECAL corresponding to the of the individual HCAL cells. The energy associated with a tower is calculated as the sum of all contributing readout cells which pass a given energy threshold. For the purpose of jet clustering, the towers are treated as massless particles, with the energy given by the tower energy, and the direction defined by the interaction point and the center of the tower itself.

5.4.2 Jet clustering algorithm

The Iterative Cone (IC) algorithm [64] is used to reconstruct jets for this analysis. In this algorithm, an E_T-ordered list of input calorimetric towers is created. A cone of size R in η, ϕ space is cast around the input object with the largest transverse energy above a specified seed threshold. The calorimeter towers within the cone are used to calculate a proto-jet energy and direction, using the following relations:

$$
\begin{aligned}
\mathrm{E}_T &= \sum \mathrm{E}_T^i \\
\eta &= \frac{1}{\mathrm{E}_T} \sum \mathrm{E}_T^i \eta^i \\
\phi &= \frac{1}{\mathrm{E}_T} \sum \mathrm{E}_T^i \phi^i
\end{aligned}
$$

The computed direction is used to seed a new proto-jet. The procedure is repeated until both the energy and the direction remain stable between two following steps. Then the reconstructed jet is created and the constituents are removed from the input objects list. This is done until all the towers with energy above the threshold are used. For this analysis, the cone size has been set to $R = 0.5$. The calorimeter towers (ECAL+HCAL) with $E_T > 1$ GeV have been used as input seeds and reconstructed jets have been required to have $E_T > 10$ GeV.

5.4.3 Jet cleaning algorithm

A reconstructed high P_T photon, depositing all its energy in the ECAL and no energy in HCAL, can be identified as a jet by using the clustering algorithm described so far. In order to avoid double counting in the collections of reconstructed jets, a simple jet cleaning procedure is applied to keep jet candidates separated from reconstructed photons. Reconstructed jets with at least one reconstructed photon in a cone of $\Delta R = 0.1$ around the direction of the jet itself, are removed from the list. Figure 5.8 shows the distribution of the number of reconstructed jets with $P_T > 50$ GeV in signal events, before and after the jet cleaning procedure described so far. Since there are two high P_T photons in most of signal events, there is a shift of about two bins between the two distributions.
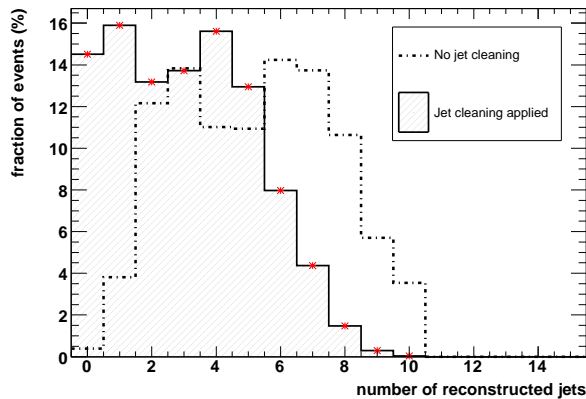

Figure 5.8: Number of reconstructed jets with $P_T > 50$ GeV in signal events before (dotted) and after (filled) the jet cleaning procedure, for the sample *GMSB_L140_ctau0*.

5.5 Event selection

5.5.1 Online HLT selection

All events passing the Level-1 trigger are read out and processed in the High Level Trigger (HLT) farm to reduce the rate of events to about 100 Hz. Because of the presence of two high P_T photons in signal events, both single and double photon triggers have been investigated.

The selection of photons and electrons at HLT level proceeds in three steps. The first step, Level-2, uses only calorimeter information. The energy in the ECAL is clustered to form superclusters (see section 5.1.2) and an E_T (η) threshold is applied on the corrected supercluster energy (position). The second step, Level-2.5, uses the information from pixel detectors. Hits are sought consistent with a track pointing to the supercluster. If the required hits are not found, the candidate is considered for the photon triggers, otherwise it is a possible electron candidate. In the final-step, Level-3, the full tracker information is used for electron reconstruction and for photon isolation.

The photon isolation variables that are used at HLT level are:

Track isolation , number of tracks with P_T larger than 1.5 GeV inside a cone with $\Delta R < 0.3$ around the photon candidate;

ECAL isolation , total E_T of all island basic clusters with $\Delta R < 0.3$ around the photon candidate, excluding those belonging to the supercluster itself;

HCAL isolation , total transverse energies of HCAL towers within $\Delta R < 0.3$ around the photon candidate.

A summary of HLT selection criteria, for a luminosity of 2×10^{33} cm^{-2}s^{-1} is reported in table 5.1, both for single and double photon triggers. The selection for double photon trigger is looser since there is the requirement of an additional photon. The single photon HLT is finally used because of the slightly higher efficiency on signal events and the larger background rejection compared to the double photon trigger.

Since in signal events multiple jets are present, some hadronic activity close to signal photons is possible. This introduces a loss of efficiency of the isolation criteria. Figure 5.9 shows the selection efficiency for signal events after the three levels of single photon HLT. Signal efficiency is high after Level-1/Level-2 triggers ($\sim 100/93\%$) while drops to 40% at Level-3 because of the isolation requirements on HLT photons.

To recover this inefficiency, triggers with relaxed energy and isolation thresholds are needed. Such triggers were not available for this analysis, but they are currently being implemented in the new computing model of the experiment. The use of these relaxed triggers is one of the possible future upgrades of this analysis.

Variable	Single photon	Double photon
$|\eta|$	< 2.5	< 2.5
E_T	> 80 GeV	> 30, 20 GeV
Track isolation	= 0	< 3
HCAL isolation (barrel)	< 6 GeV	< 8 GeV
HCAL isolation (endcaps)	< 4 GeV	< 6 GeV
ECAL isolation	< 1.5 GeV	< 2.5 GeV

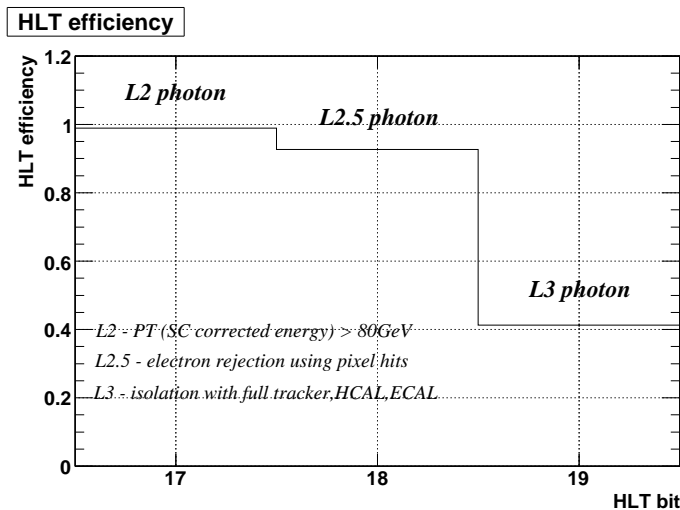Table 5.1: HLT cuts for the single and double photon streams [65].

Figure 5.9: Signal efficiency after the three level of single photon HLT selection.

5.5.2 Offline selection variables

Several reconstructed variables have been investigated to discriminate between signal and background events. Since the variables are in general correlated, each of them is displayed using a reduced sample obtained by applying

99

loose not-optimized cuts, shown in table 5.2, on the other variables, except the one under study. This is done to check the real discriminating power of each variable. The sample *GMSB_L140_ctau0* is used in the following plots. All distributions are normalized to unity.

HLT	$\sum P_T^{trk}$	H/E	$P_T^{1st\gamma}$/ $P_T^{2nd\gamma}$	$|\eta^{1st\gamma}|/|\eta^{2nd\gamma}|$
single γ	< 9 GeV	< 0.1	> 80/10 GeV	< 1.479

Table 5.2: Not optimized loose selection criteria

P_T of photons

Two high P_T photons are expected to be produced in a large fraction of the neutralino decays, as discussed in section 4.2.1. Real photons and high energy isolated π^0s from background events have a softer P_T spectrum. For this reason, the P_T of the first ($P_T^{1st\gamma}$) and second ($P_T^{2nd\gamma}$) reconstructed photons with highest transverse momentum of the event represent good discriminating variables. Figure 5.10 shows the distributions of $P_T^{1st\gamma}$ and $P_T^{2nd\gamma}$. The drop of events below 80 GeV, in the $P_T^{1st\gamma}$ distribution, is due to the P_T threshold applied at HLT. The P_T resolution for signal photons reconstructed both in barrel and endcaps is around 2%, as shown in figure 5.12.

η of photons

As discussed in section 4.2.1, about 80% of photons from neutralino decay hit the ECAL barrel, while background photons have a flatter η distribution. The distribution of η, both for the first ($\eta^{1st\gamma}$) and second ($\eta^{2nd\gamma}$) reconstructed photons with highest transverse momentum of the event, is shown in figure 5.11. [1]

Jet multiplicity

In signal events several high P_T jets are produced either from the fragmentation of quarks generated by the decay of SUSY particles or from hadronic decays of W/Z bosons and τ leptons. On the other hand, background events

---

[1] A non-physical asymmetry is observed in the η distribution of reconstructed photons. This is due to a known bug in the reconstruction software used. In particular, it concerns the reconstruction of tracks used for photon isolation. However, the impact of this asymmetry in the final estimate of this analysis is expected to be small.

are characterized by a lower jet multiplicity. Figure 5.13 shows the distribution of the number of reconstructed jets with $P_T > 50$ GeV, for signal and background events.

P_T and η of reconstructed jets

In signal events, the fragmentation of quarks from SUSY particles (with masses around several hundreds of GeV) produces high P_T jets in the central region of the calorimeter. For background events the jet P_T spectrum is softer. The P_T and η distributions of the first and the fourth reconstructed jets with highest transverse momentum for signal and background events are shown in figure 5.14 and figure 5.15, respectively. Only jets with $P_T > 25$ GeV are considered.

Missing transverse energy

Missing transverse energy is one of the most discriminating variables between signal and background as shown in figure 5.16. In signal events the large $\not{E}_T$ is a consequence of the two high P_T gravitinos escaping detection. The background events, in particular QCD events, have a small $\not{E}_T$. Some EW events can have a large $\not{E}_T$ due to the presence of high energy neutrinos from W/Z leptonic decays.

The $\not{E}_T$ resolution depends on the quality of the energy measurements in the calorimeters, as discussed in equation 5.9. Figure 5.17 shows the distribution of the $\not{E}_T$ residuals ($\Delta_{\not{E}_T} = \not{E}_T - \not{E}_T^{gen}$) for signal and background events. For GMSB events, the RMS of the $\Delta_{\not{E}_T}$ distribution is around 50 GeV with an almost symmetric shape. It has to be noted that this spread must be compared with the typical values of $\not{E}_T^{gen}$ of several hundreds GeV.

The same distribution, displayed in logarithmic scale (figure 5.18), shows the presence of large tails for both QCD and EW events, determining a contamination of the signal region, which extends at large values of the reconstructed $\not{E}_T$. This is a possible source of systematic errors in the extraction of signal events at high $\not{E}_T$. Detailed studies are needed to understand the origin of these tails and the kinematics of such pathological events.
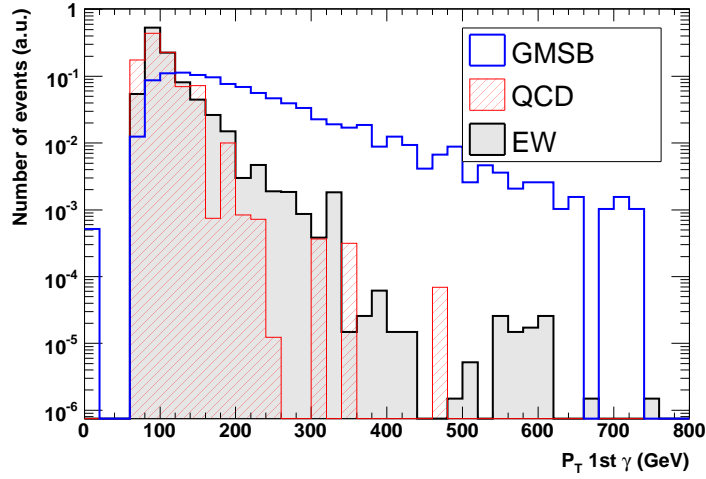
(a)
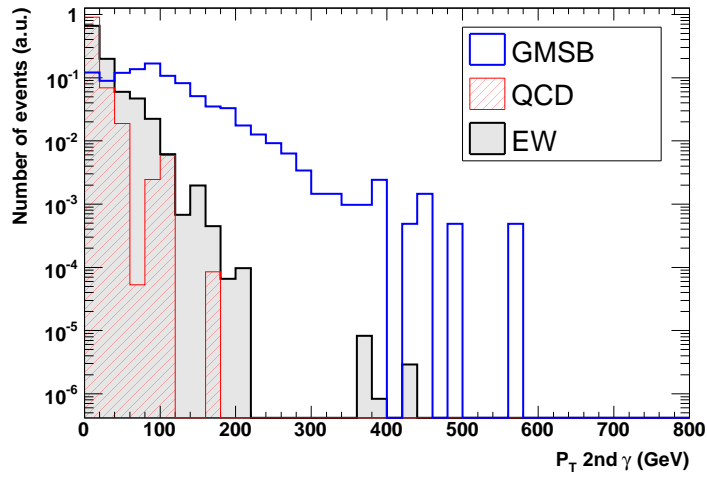
(b)

Figure 5.10: The distribution of P$_T$ of first (a) and second (b) photon with highest transverse momentum for signal and background events. Loose selection criteria of table 5.2 are applied, except the one on the variable under study.

102
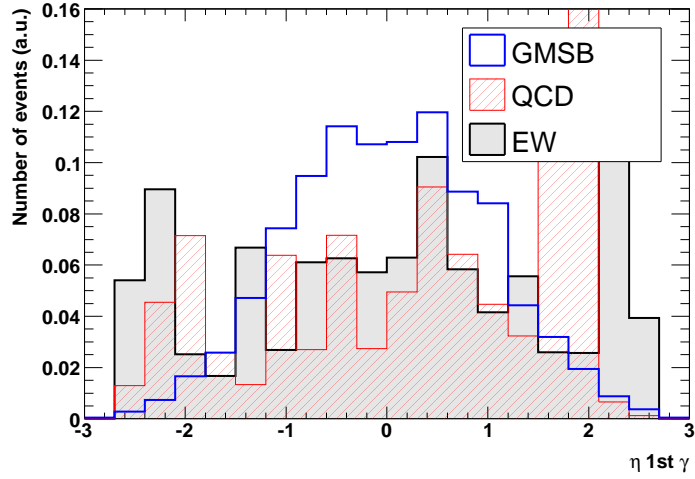
(a)
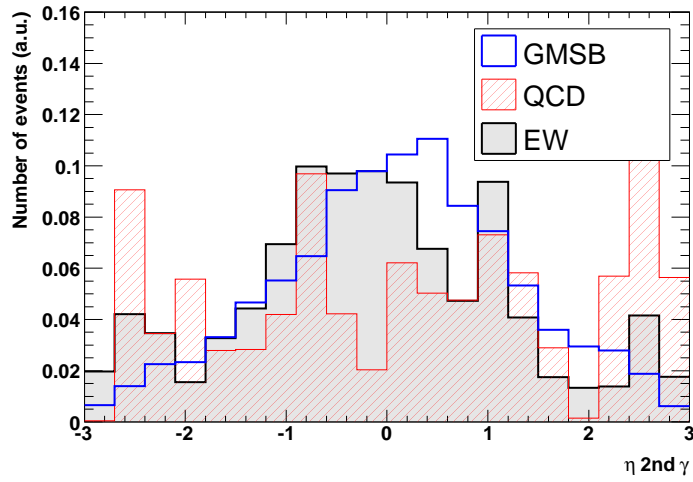
(b)

Figure 5.11: The distribution of η of first (a) and second (b) photon with highest transverse momentum for signal and background events. Loose selection criteria of table 5.2 are applied, except the one on the variable under study.

103

Figure 5.12: Distribution of P_T^{reco}/P_T^{gen} for signal photons reconstructed both in the barrel and in the endcaps.
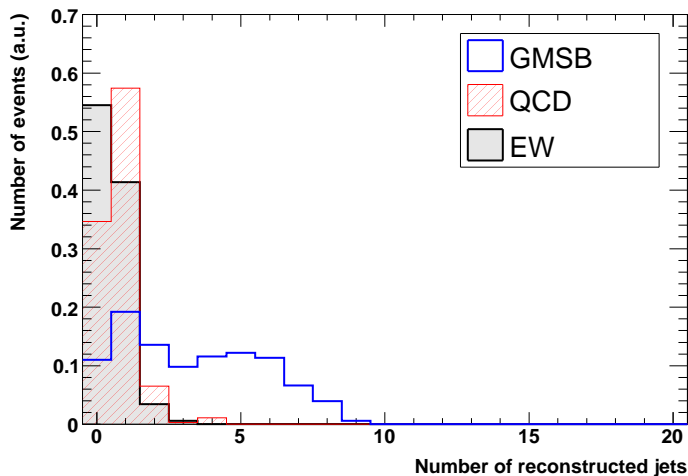
Figure 5.13: Number of reconstructed jets for signal and background events. Loose selection criteria of table 5.2 are applied.
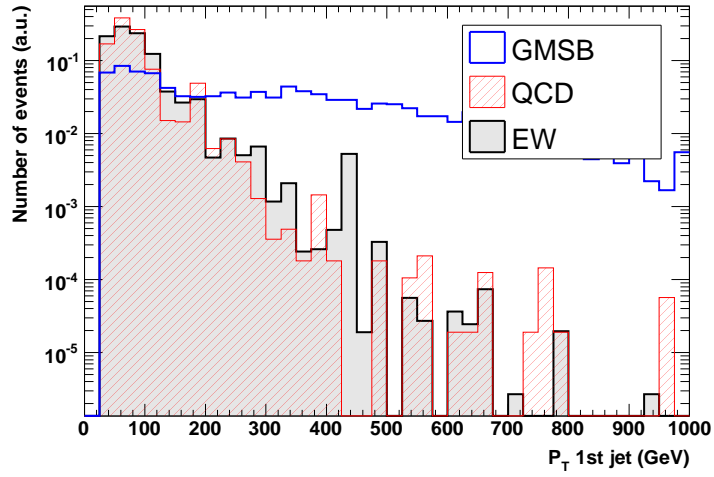
(a)
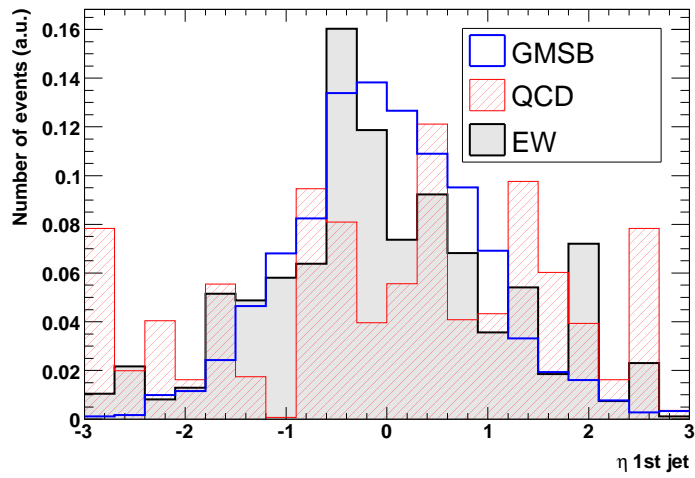
(b)

Figure 5.14: The distribution of P$_T$ (a) and η (b) of the reconstructed jet with highest transverse momentum for signal and background events. Loose selection criteria of table 5.2 are applied.
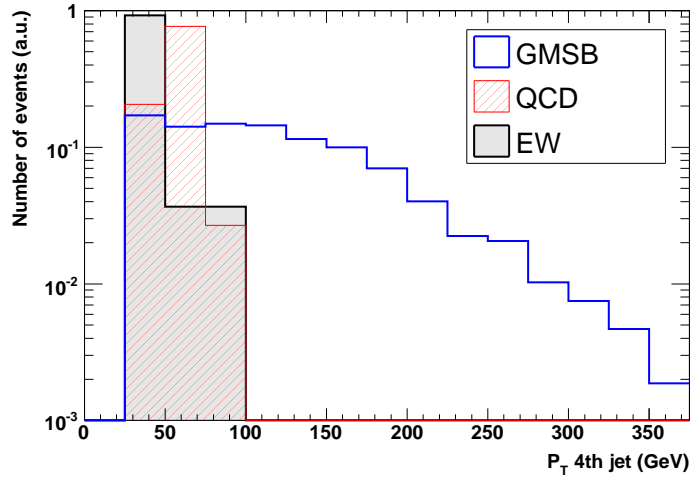
(a)
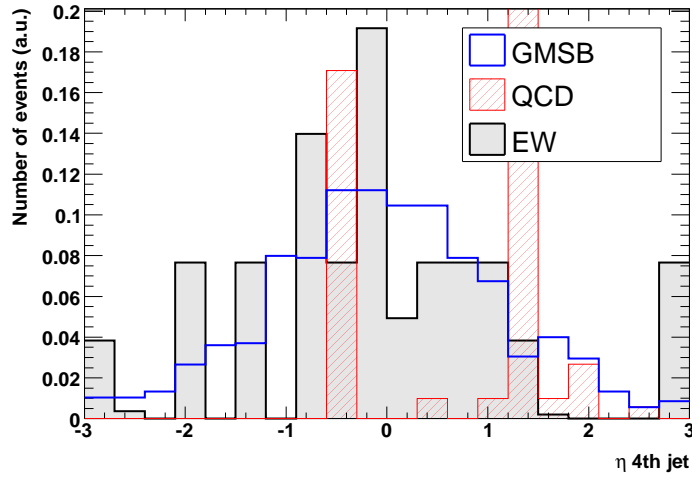
(b)

Figure 5.15: The distribution of P_T (a) and η (b) of the fourth reconstructed jet with highest transverse momentum for signal and background events. Loose selection criteria of table 5.2 are applied. The requirement of at least 4 reconstructed jets in the event reduces the background statistics, compared to figure 5.14.
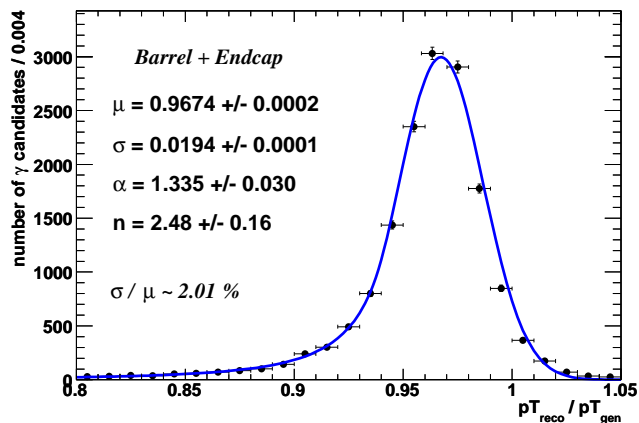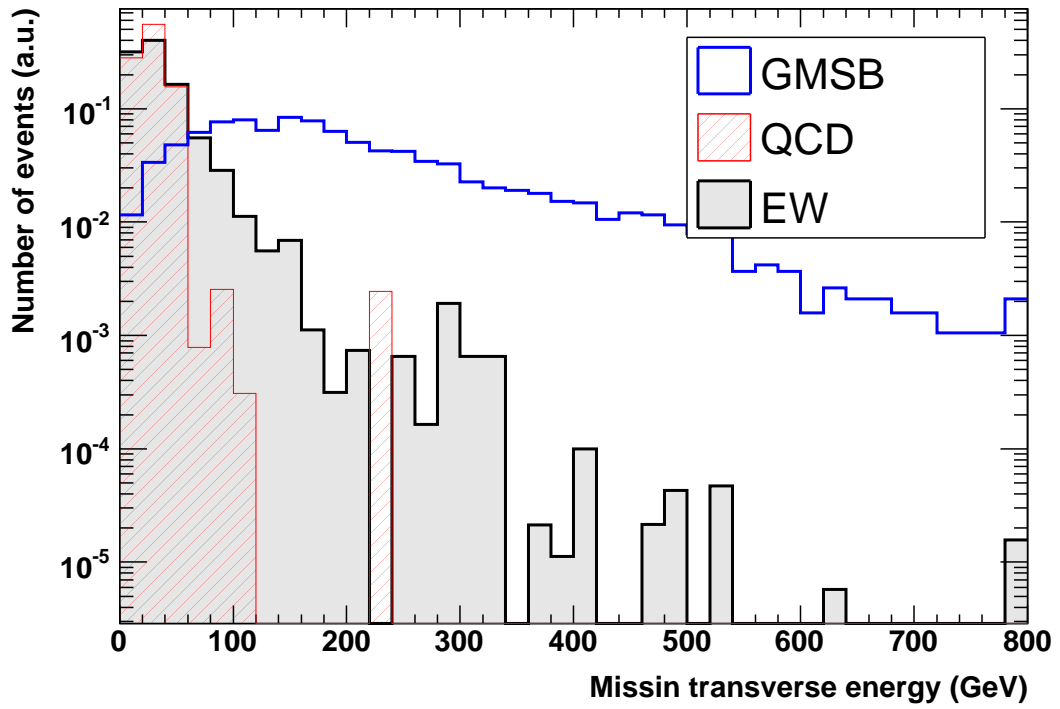
Figure 5.16: Distribution of the missing transverse energy of the event for signal and background events. Loose selection criteria of table 5.2 are applied.
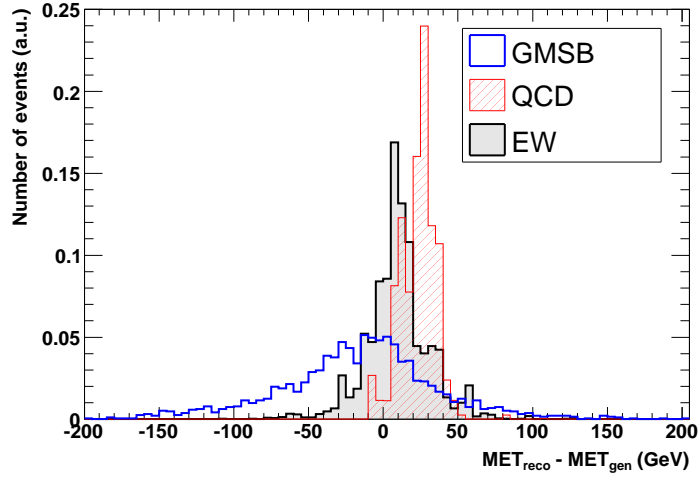
Figure 5.17: Distribution of the residual $\displaystyle{\not}E_T - {\not}E_T^{gen}$ for signal and background events. Loose selection criteria of table 5.2 are applied.
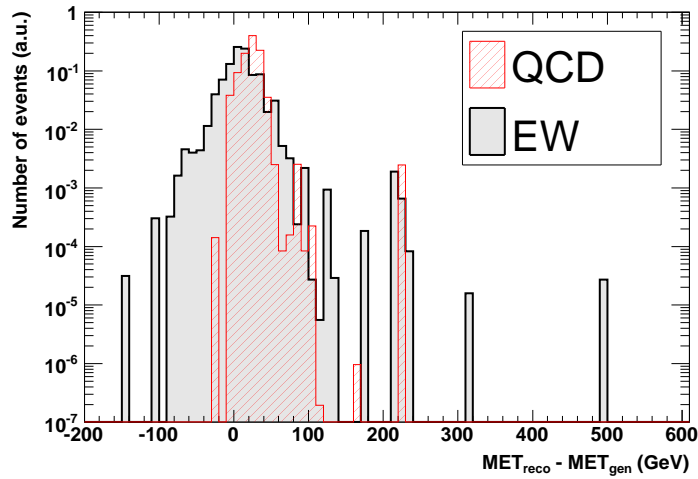
Figure 5.18: Distribution of the residual $\displaystyle{\not}E_T - {\not}E_T^{gen}$ in log scale for background events. Loose selection criteria of table 5.2 are applied.

5.5.3 Optimization of selection criteria

The variables discussed so far are, in general, correlated thus requiring and optimization of the selection criteria. The optimization is based on the minimization of the the ratio $\sigma_{GMSB}^{rel} = \sigma^{GMSB}/N_{GMSB}$, where N_{GMSB} and σ^{GMSB} are, respectively, the number of signal events and its relative statistical uncertainty, both extracted using the likelihood fit to $\not{E}_T$ distribution described in section 5.6.

For the variable Δ (defined in section 5.1.4), which is mostly uncorrelated with the others, the optimization is performed by varying, in a given range, the threshold X on the variable under study, and fixing the thresholds of the remaining ones to reasonable values.

For the pair of variables $(P_T^{1^{st}\gamma}, P_T^{2^{nd}\gamma})$ and $(\sum P_T^{trk}, H/E)$, which are strongly correlated, an optimization in a two-dimensional space is performed. The method is similar to the one-dimensional case, but with the difference that both the thresholds of the two variables are varied at the same time. As an example, figure 5.19 shows the correlation between $P_T^{1^{st}\gamma}$ and $P_T^{2^{nd}\gamma}$ (a) and the results of the optimization in the two-dimensional space (b). The selected criteria for $P_T^{1^{st}\gamma}$ and $P_T^{2^{nd}\gamma}$ correspond to the bin with the minimum value in figure 5.19 (b).

Since the kinematics and the cross section of the signal events depend on Λ, the optimization is repeated for different Λ values.

The optimized selection criteria are reported in table 5.3. Two high P_T isolated photons are required to be reconstructed in the barrel. Photons in the endcaps are not considered, because of the large background contamination and the small fraction of signal photons at high η values. The asymmetry Δ is not included in the final selection, since at high energies it does not provide any discriminating power between signal photons and π^0s from background events. The P_T and the η of the first and fourth reconstructed jet with highest transverse momentum of the event can contribute to further discriminate signal from background. It has been decided to not include them, since they are in general very affected by systematics. This is preferable in the first stage of the experiment, when detector related uncertainties are not fully understood.

$\not{E}_T$ resulted to be the most discriminating variable. Because of this it is used to extract signal yield in the likelihood fit and it is not included in the selection.
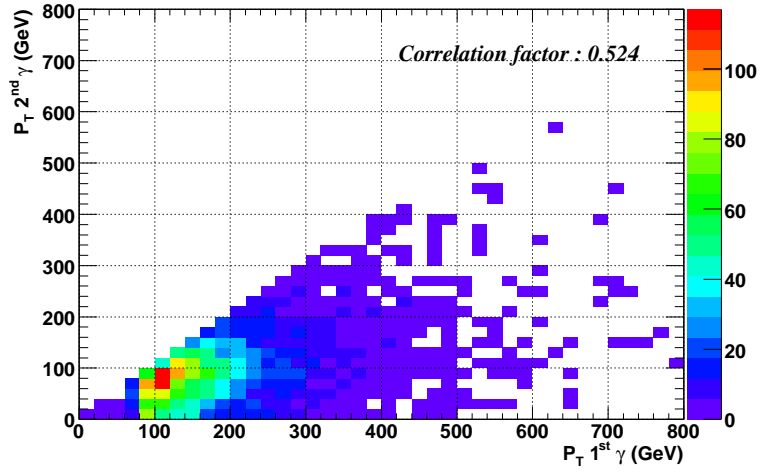
(a)
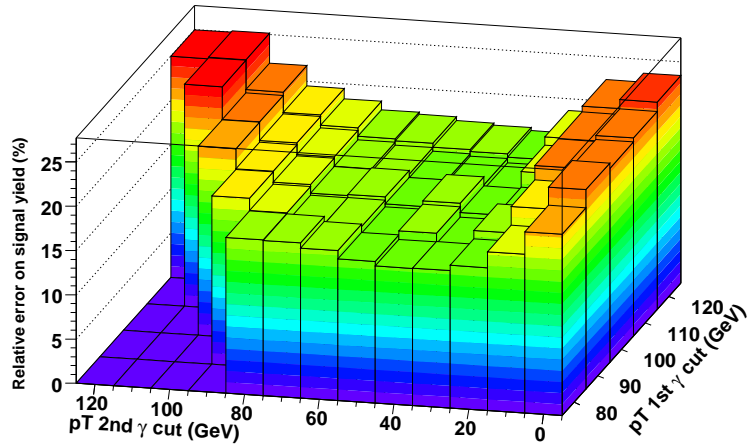
(b)

Figure 5.19: The scatter plot of $P_T^{1st\gamma}$ versus $P_T^{2nd\gamma}$ (a) and the relative error $\varepsilon_{N_s}^{rel}$ on the determination of number of signal events for different pairs of cuts in the $P_T^{1st\gamma}$ vs $P_T^{2nd\gamma}$ space (b). The cuts on the other discriminating variables are fixed.

Λ (TeV)	HLT	$\sum \mathrm{P}_T^{trk}$	H/E	$\mathrm{P}_T^{1^{st}\gamma}$/ $\mathrm{P}_T^{2^{nd}\gamma}$	$|\eta^{1^{st}\gamma}|/|\eta^{2^{nd}\gamma}|$
$100, 120, 140$	single γ	< 9 GeV	< 0.1	> 90/30 GeV	< 1.479
$160, 180$	single γ	< 9 GeV	< 0.1	> 110/30 GeV	< 1.479

Table 5.3: Optimized selection criteria of $\gamma\gamma$ sample for different GMSB samples (see table 4.1).

5.5.4 Selection efficiency

The expected number of selected events with 1 fb^{-1} of integrated luminosity and the relative efficiencies, are reported, in tables 5.4/5.5 for $\Lambda = 100, 120, 140$ TeV, and in tables 5.6/5.7, for $\Lambda = 160, 180$ TeV.

The drop of signal efficiency ($\varepsilon_{HLT} \approx 35 - 40\%$) is observed after the single photon HLT selection. This is mostly due to the photon isolation, as shown in section 5.5.1. Offline isolation criteria further reduce the signal efficiency to $\approx 25 - 35\%$. The signal efficiency after the full selection ranges between 13% and 18% for different values of Λ.

The background is dominated by γ+jet and QCD events, which represent $\sim 95\%$ of the total number of selected events. The selection criteria on HLT and $\mathrm{P}_T^{2^{nd}\gamma}$ are the most powerful requirements to reject background. Given the limited MC sample statistics, the statistical uncertainty on the background selection efficiency is large, $\approx 20\%$ for EW background and more than 50% for QCD background.

	N								
Dataset	$\Lambda = 100$	$\Lambda = 120$	$\Lambda = 140$	γ+jet	QCD jets	$t\bar{t}$	W+jet	Z+jet	All bkg
$N_{ev}(1\ \mathrm{fb}^{-1})$	2.88E+3	1.05E+3	4.55E+2	6.19E+7	1.80E+11	4.92E+5	1.54E+8	3.90E+7	1.81E+11
MC preselection	–	–	–	4.79E+7	2.71E+8	9.68E+4	9.53E+6	2.55E+6	3.31E+8
single γ HLT	1.02E+3	4.04E+2	1.88E+2	1.57E+6	6.23E+5	5.91E+2	1.95E+4	6.26E+3	2.22E+6
At least 2 γ (iso hcal)	1.01E+3	4.01E+2	1.86E+2	8.89E+5	3.19E+5	5.19E+2	1.07E+4	5.31E+3	1.22E+6
At least 2 γ (iso trk)	8.15E+2	3.20E+2	1.45E+2	2.75E+5	1.16E+5	2.27E+2	4.16E+3	2.56E+3	3.98E+5
$|\eta^{1^{st}\gamma}| < 1.479$	6.82E+2	2.75E+2	1.25E+2	1.61E+5	4.90E+4	1.49E+2	1.47E+3	8.88E+2	2.13E+5
$|\eta^{2^{nd}\gamma}| < 1.479$	5.21E+2	2.06E+2	9.58E+1	9.15E+4	3.75E+4	1.00E+2	9.97E+2	4.84E+2	1.31E+5
$\mathrm{P}_T^{1^{st}\gamma} > 90$ GeV	4.70E+2	1.90E+2	9.03E+1	4.54E+4	1.21E+4	6.84E+1	4.72E+2	2.92E+2	5.83E+4
$\mathrm{P}_T^{2^{nd}\gamma} > 30$ GeV	3.74E+2	1.57E+2	7.64E+1	3.95E+3	6.98E+2	1.08E+1	1.04E+2	9.20E+1	4.85E+3
Total $\gamma\gamma$ selection	374 ($\pm$4%)	157 ($\pm$4%)	76 ($\pm$2%)	3950 ($\pm$41%)	698 ($\pm$57%)	11 ($\pm$14%)	104 ($\pm$25%)	92 ($\pm$23%)	4855 ($\pm$34%)

Table 5.4: Number of selected events N, after the application of $\gamma\gamma$ selection requirements, for the GMSB signal with $\Lambda = 100, 120, 140$ TeV and the Standard Model backgrounds. $N_{ev}\left(1\ \mathrm{fb}^{-1}\right)\left(= \mathcal{L}_{int} \cdot \sigma\right)$ is the total number of events for an integrated luminosity $\mathcal{L}_{int} = 1\ \mathrm{fb}^{-1}$, expected at LHC without any selection. Number of events after cuts are rescaled to $\mathcal{L}_{int} = 1\ \mathrm{fb}^{-1}$ as well. Relative statistical uncertainty on the number of events after total selection is reported in brackets.

	ε								
Dataset	$\Lambda = 100$	$\Lambda = 120$	$\Lambda = 140$	γ+jet	QCD jets	$t\bar{t}$	W+jet	Z+jet	All bkg
MC preselection	–	–	–	77.4%	0.2%	19.7%	6.2%	6.5%	0.2%
single γ HLT	35.4%	38.5%	41.3%	3.3%	0.2%	0.6%	0.2%	0.2%	0.7%
At least 2 γ (iso hcal)	99.0%	99.3%	98.9%	56.6%	51.2%	87.8%	54.8%	84.8%	55.2%
At least 2 γ (iso trk)	80.7%	79.8%	78.0%	30.9%	36.4%	43.7%	39.0%	48.3%	32.5%
$|\eta^{1^{st}\gamma}| < 1.479$	83.7%	85.9%	86.2%	58.5%	42.2%	65.6%	35.2%	34.6%	53.4%
$|\eta^{2^{nd}\gamma}| < 1.479$	76.4%	74.9%	76.6%	56.8%	76.4%	67.1%	68.0%	54.5%	61.4%
$P_T^{1^{st}\gamma} > 90$ GeV	90.2%	92.2%	94.3%	49.6%	32.2%	68.4%	47.3%	60.2%	44.7%
$P_T^{2^{nd}\gamma} > 30$ GeV	79.6%	82.6%	84.6%	8.7%	5.8%	15.8%	22.0%	31.6%	8.3%
ε_{sel}	13.0%	15.0%	17.0%	6.4E-5	3.9E-9	2.2E-5	6.7E-7	2.4E-6	2.7E-8
$\sigma_{\varepsilon_{sel}}$	0.5%	0.6%	0.4%	2.6E-5	2.2E-9	3.0E-6	1.7E-7	5.4E-7	9.1E-9

Table 5.5: Selection efficiency ε for different requirements of $\gamma\gamma$ selection, for the GMSB signal with $\Lambda = 100, 120, 140$ TeV and the Standard Model backgrounds. The efficiencies are shown after the application of the selection requirements in cascade, starting from the top to the bottom of each column. For each requirement, the efficiency is defined as the number of events passing that cut divided by the number of events selected by all the cuts previously applied. The last two rows show the total selection efficiency ε_{sel} and its statistical uncertainty $\sigma_{\varepsilon_{sel}}$.

Dataset					N			
	$\Lambda = 160$	$\Lambda = 180$	γ+jet	QCD jets	$t\bar{t}$	W+jet	Z+jet	All bkg
N_{gen}	3800	4000	94000	2606770	2233500	2876500	1513250	9324020
$N_{ev}(1 \text{ fb}^{-1})$ Ntot	2.15E+2	1.10E+2	6.19E+7	1.80E+11	4.92E+5	1.54E+8	3.90E+7	1.81E+11
MC preselection	–	–	4.79E+7	2.71E+8	9.68E+4	9.53E+6	2.55E+6	3.31E+8
single γ HLT	9.38E+1	5.06E+1	1.57E+6	6.23E+5	5.91E+2	1.95E+4	6.26E+3	2.22E+6
At least 2 γ (iso hcal)	9.24E+1	4.99E+1	8.89E+5	3.19E+5	5.19E+2	1.07E+4	5.31E+3	1.22E+6
At least 2 γ (iso trk)	7.29E+1	3.83E+1	2.75E+5	1.16E+5	2.27E+2	4.16E+3	2.56E+3	3.98E+5
$|\eta^{1^{st}\gamma}| < 1.479$	6.34E+1	3.26E+1	1.61E+5	4.90E+4	1.49E+2	1.47E+3	8.88E+2	2.13E+5
$|\eta^{2^{nd}\gamma}| < 1.479$	5.04E+1	2.55E+1	9.15E+4	3.75E+4	1.00E+2	9.97E+2	4.84E+2	1.31E+5
$P_T^{1^{st}\gamma} > 110$ GeV	4.44E+1	2.27E+1	2.11E+4	8.96E+3	3.39E+1	2.58E+2	1.17E+2	3.05E+4
$P_T^{2^{nd}\gamma} > 30$ GeV	3.81E+1	1.96E+1	1.32E+3	6.38E+2	5.72E+0	7.10E+1	4.30E+1	2.08E+3
Total $\gamma\gamma$ selection	38 ($\pm$3%)	20 ($\pm$3%)	1320 ($\pm$70%)	638 ($\pm$62%)	57 ($\pm$19%)	71 ($\pm$28%)	43 ($\pm$17%)	2080 ($\pm$49%)

Table 5.6: Number of selected events N, after the application of $\gamma\gamma$ selection cuts, for the GMSB signal with $\Lambda = 160, 180$ TeV and the Standard Model backgrounds. $N_{ev}\left(1 \text{ fb}^{-1}\right)(= \mathcal{L}_{int} \cdot \sigma)$ is the total number of events for an integrated luminosity $\mathcal{L}_{int} = 1 \text{ fb}^{-1}$, expected at LHC without any selection. Number of selected events are rescaled to $\mathcal{L}_{int} = 1 \text{ fb}^{-1}$ as well. Relative statistical uncertainty on the number of events after total selection is reported in brackets.

	ε							
Dataset	$\Lambda = 160$	$\Lambda = 180$	γ+jet	QCD jets	$t\bar{t}$	W+jet	Z+jet	All bkg
MC preselection	–	–	77.4%	0.2%	19.7%	6.2%	6.5%	0.2%
single γ HLT	43.6%	46.0%	3.3%	0.2%	0.6%	0.2%	0.2%	0.7%
At least 2 γ (iso hcal)	98.5%	98.6%	56.6%	51.2%	87.8%	54.8%	84.8%	55.2%
At least 2 γ (iso trk)	78.9%	76.8%	30.9%	36.4%	43.7%	39.0%	48.3%	32.5%
$|\eta^{1^{st}\gamma}| < 1.479$	87.0%	85.1%	58.5%	42.2%	65.6%	35.2%	34.6%	53.4%
$|\eta^{2^{nd}\gamma}| < 1.479$	79.5%	78.2%	56.8%	76.4%	67.1%	68.0%	54.5%	61.4%
$P_T^{1^{st}\gamma} > 110$ GeV	88.1%	89.0%	23.1%	23.9%	33.9%	25.9%	24.2%	23.3%
$P_T^{2^{nd}\gamma} > 30$ GeV	85.8%	86.3%	6.3%	7.1%	16.9%	27.5%	36.6%	6.8%
ε_{sel}	18.0%	18.0%	2.1E-5	3.5E-9	1.2E-5	4.6E-7	1.1E-6	1.1E-8
$\sigma_{\varepsilon_{sel}}$	0.6%	0.6%	1.5E-5	2.2E-9	2.2E-6	1.3E-7	1.9E-7	5.6E-9

Table 5.7: Selection efficiency ε for different cuts of $\gamma\gamma$ selection, for the GMSB signal with $\Lambda = 160, 180$ TeV and the Standard Model backgrounds. The efficiencies are shown after the application of the selection requirements in cascade, starting from the top to the bottom of each column. For each requirement, the efficiency is defined as the number of events passing that cut divided by the number of events selected by all the cuts previously applied. The last two rows show the total selection efficiency ε_{sel} and its statistical uncertainty $\sigma_{\varepsilon_{sel}}$.

5.6 Determination of signal using a likelihood fit

In this section, the likelihood fit to determine signal and background yields is discussed. It has been chosen to extract the signal from the $\displaystyle{\not}E_{\mathrm{T}}$ distribution since it is the best variable to discriminate signal from background. Therefore, an excess of events in the $\displaystyle{\not}E_{\mathrm{T}}$ distribution, compared to the expectation of the SM, can be directly attributed to the signature of SUSY events. This approach offers many advantages. For instance the systematics on $\displaystyle{\not}E_{\mathrm{T}}$ resolution are more under control and the background shape can be obtained from data. In addition the background normalization is extracted from the fit itself.

The $\displaystyle{\not}E_{\mathrm{T}}$ distribution ($h_{\gamma\gamma}(\displaystyle{\not}E_{\mathrm{T}})$) is parametrized as the sum of tree components, one for the GMSB signal and two for QCD and EW backgrounds

$$h_{\gamma\gamma}(\displaystyle{\not}E_{\mathrm{T}}) = N_{GMSB} \cdot h_{GMSB}(\displaystyle{\not}E_{\mathrm{T}}) + N_{EW} \cdot h_{EW}(\displaystyle{\not}E_{\mathrm{T}}) + N_{QCD} \cdot h_{QCD}(\displaystyle{\not}E_{\mathrm{T}}) \quad (5.11)$$

where $h_{GMSB}(\displaystyle{\not}E_{\mathrm{T}})$, $h_{EW}(\displaystyle{\not}E_{\mathrm{T}})$ and $h_{QCD}(\displaystyle{\not}E_{\mathrm{T}})$ are, respectively, the Probability Density Functions (PDF) of signal, EW and QCD component, while N_{GMSB}, N_{EW} and N_{QCD} are, respectively, the yields of signal, EW and QCD component. The shape of the PDFs is given by a binned distribution of simulated events. The normalization of each component are left as free parameters in a likelihood fit to data.

5.7 Results of signal yield

The fit is applied to Monte Carlo samples of signal and background events which pass the selection, described in section 5.5.4, and the number of selected events is normalized to 1 fb^{-1}. The display of the fit result is shown in figure 5.20. The distributions are plotted in bins of $\displaystyle{\not}E_{\mathrm{T}}$ with variable width, and the bin contents correspond to the number of events in that bin divided by the corresponding bin width. The uncertainties on the fitted yields in each bin of $\displaystyle{\not}E_{\mathrm{T}}$ correspond to Poissonian errors. The fitted number of signal events (N_{GMSB}) with the relative statistical fit error (σ_{GMSB}) are reported in table 5.8, for different signal samples.
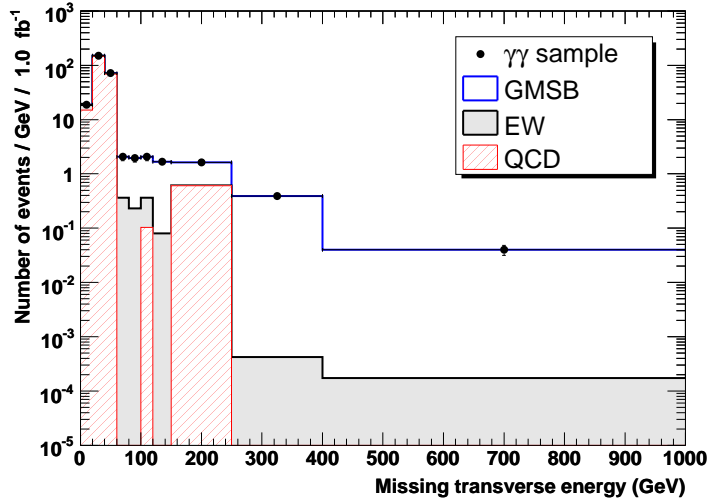
(a)
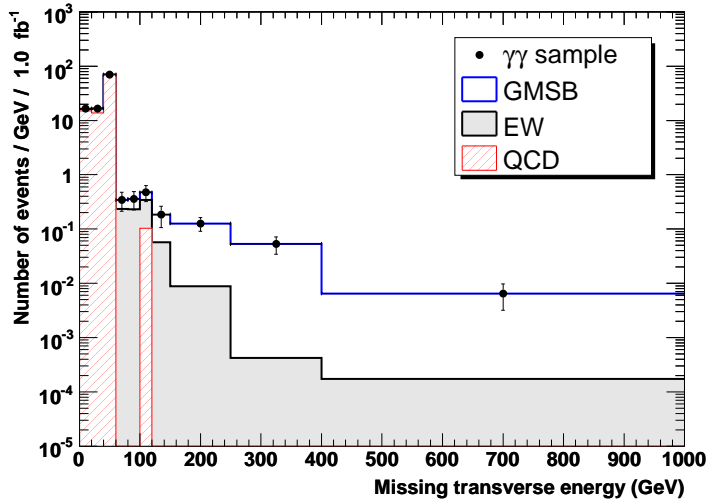
(b)

Figure 5.20: Result of the fit for two GMSB scenarios (a) $\Lambda = 100$ TeV, (b) $\Lambda = 160$ TeV, with $\mathcal{L}_{int} = 1$ fb^{-1}. Hashed area is the QCD component; filled area is the EW component; empty area is the GMSB component. Number of selected events is normalized to 1 fb^{-1}.

Λ (TeV)	$N_{GMSB} \pm \sigma_{GMSB}$	σ_{GMSB}^{rel}
100	374.2 ± 23.5	$\sim 6\%$
120	157.2 ± 16.0	$\sim 10\%$
140	76.3 ± 11.8	$\sim 15.5\%$
160	38.0 ± 7.6	$\sim 20\%$
180	19.5 ± 5.6	$\sim 29\%$

Table 5.8: Number of signal events N_{GMSB} and its relative statistical uncertainty σ_{GMSB} extracted from fit results with $\mathcal{L}_{int} = 1$ fb^{-1}, for GMSB signal samples at different Λ. σ_{GMSB}^{rel} is the relative statistical uncertainty on measured signal yield.

5.8 Background estimate from data

Two different approaches are proposed to estimate, respectively, the amount of EW and QCD background, directly from data. These two procedures are discussed in the following.

5.8.1 EW control sample

The shape of the $\not{E}_{\mathrm{T}}$ distribution $h_{EW}(\not{E}_{\mathrm{T}})$, used in the likelihood fit described so far (see equation 5.11), can be estimated directly from data using a control sample. The basic idea is to select events which are completely independent from the $\gamma\gamma$ sample, but have $\not{E}_{\mathrm{T}}$ shape and resolution similar to the EW component of the photon sample.

As discussed in section 4.3.2, in the EW background most of the energetic fake photons come from the mis-reconstructed electrons from W/Z decays. A good control sample can be obtained by using the same selection criteria applied for the $\gamma\gamma$ sample, but requiring that the reconstructed electromagnetic object with highest transverse energy of the event is identified as an electron instead of a photon. In this simple approach, the supercluster is identified as an electron if there is only one track in a ΔR cone of 0.1 around the position of the energy deposit, with $\mathrm{P}_T^{sc}/\mathrm{P}_T^{track} < 2$, where P_T^{sc} is the P_T of the supercluster and P_T^{track} is the transverse momentum calculated by the tracker; these are very simple cuts for the electron identification, which can be improved using additional variables and optimizing the selection criteria. In addition, the single photon HLT requirement is replaced by the single electron one, with an additional veto on the single photon trigger bit. The control sample, called $e\gamma$, is therefore completely independent from the $\gamma\gamma$ sample, by construction.

For EW events, the $\not{E}_{\mathrm{T}}$ distributions of the $e\gamma$ sample and the $\gamma\gamma$ sample are expected to be very similar in shape, since the failure of the electron track reconstruction is not correlated, in principle, with the rest of the event. With the available Monte Carlo statistics, a good agreement between the two distributions is observed (see figure 5.21).

It is important to check that QCD events do not contaminate the EW control sample. The production of high P_T electrons in QCD processes is strongly suppressed and fake electrons can come only from mis-reconstructed jets. QCD events are almost fully rejected by the electron isolation criteria at HLT level and by the offline selection requirements. For this reason, the $e\gamma$ sample is enriched in EW events, as shown in figure 5.22; with the available statistics, no QCD events are present in the $e\gamma$ sample. On the other hand, given that electrons can be produced also in the decay of SUSY particles, a small contamination of signal events is observed in the $e\gamma$ sample, mostly at large values of $\not{E}_{\mathrm{T}}$.
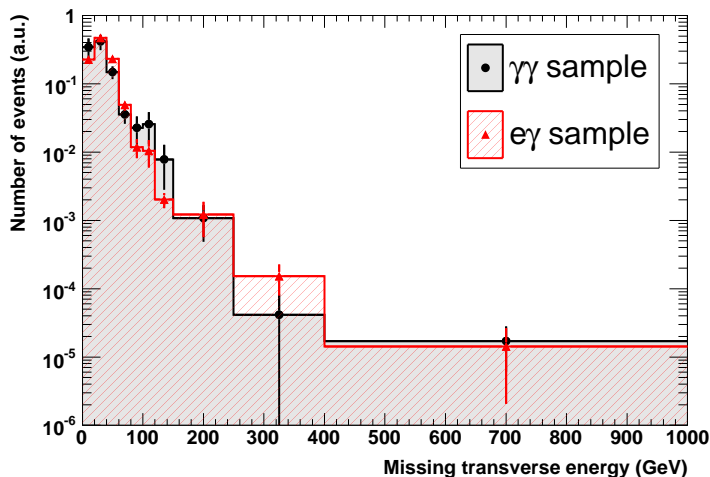

Figure 5.21: Comparison the $\not{E}_{\mathrm{T}}$ distribution of EW events between $e\gamma$ and $\gamma\gamma$ sample. Statistical errors are reported. Distributions are normalized to unity.

5.8.2   QCD control sample

For QCD background, $\pi^0 \to \gamma\gamma$ coming from jet fragmentation can be mis-reconstructed as fake photons. At energies of several tens of GeV, an isolated
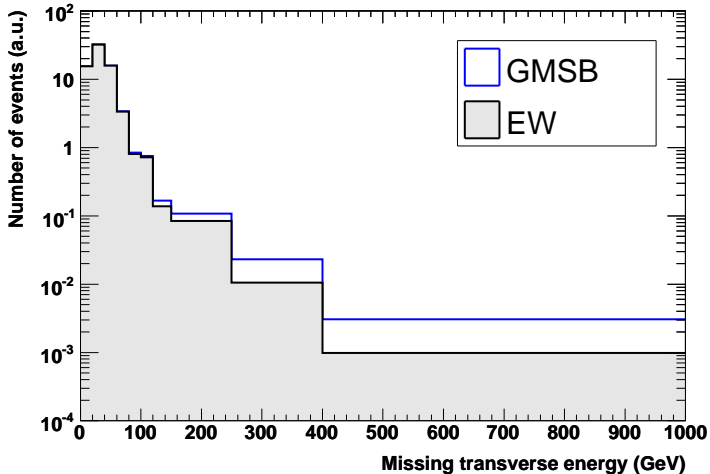
Figure 5.22: Distribution of $\not{E}_{\mathrm{T}}$ for the $e\gamma$ sample. With the available statistics no QCD events pass the selection.

π^0 produces the same signature in ECAL of a single photon, because the two photons are almost collinear.

For QCD events is not possible to apply the simple approach used in the EW case, where a good control sample, having the same $\not{E}_{\mathrm{T}}$ shape of the EW events in the $\gamma\gamma$ sample, is obtained by requiring that the reconstructed electromagnetic object with highest P_T of the event is identified as an electron instead of a photon. Thus, a different strategy must be considered to estimate the systematics on the shape of QCD background. A set of control samples, independent from the $\gamma\gamma$ sample, enriched in QCD events and with topology and resolutions similar to the QCD component of the $\gamma\gamma$ sample, needs to be found. These samples are used to compare data and MC distributions, in order to estimate the systematic uncertainties on the $\not{E}_{\mathrm{T}}$ measurement in QCD events. Because of the small MC statistics involved in this analysis, relaxed selection criteria are also considered.

As an example, a control sample selected with the 4-jet HLT is used, with the additional requirement that the single photon HLT did not fired. Loose offline selection criteria are applied, by requiring only one photon reconstructed in the barrel with $\mathrm{P}_T > 50$ GeV (see table 5.9). This control sample is enriched in QCD events, as shown in figure 5.23. The control sample is then compared with the sample used to extract the GMSB signal yield with the same relaxed cuts reported in table 5.9.

Figures 5.24 and 5.25 show the comparison of $\not{E}_{\mathrm{T}}^{gen}$ and $\Delta_{\not{E}_{\mathrm{T}}} = \not{E}_{\mathrm{T}} - \not{E}_{\mathrm{T}}^{gen}$

distributions, for the QCD events. The bulk of the distribution is similar between the sample used in the analysis and the control sample, while some discrepancies are observed in the tails.

This crude comparison shows that this approach is promising. More independent samples, based on a different selection at HLT, will be investigated in future studies.

Sample	Single γ HLT	4-jet HLT	$P_T^{1^{st}\gamma}$	$|\eta^{1^{st}\gamma}|$
γ sample	YES	–	> 50 GeV	< 1.479
QCD control sample	NO	YES	> 50 GeV	< 1.479

Table 5.9: Loose selection criteria for the γ sample and for the QCD control sample
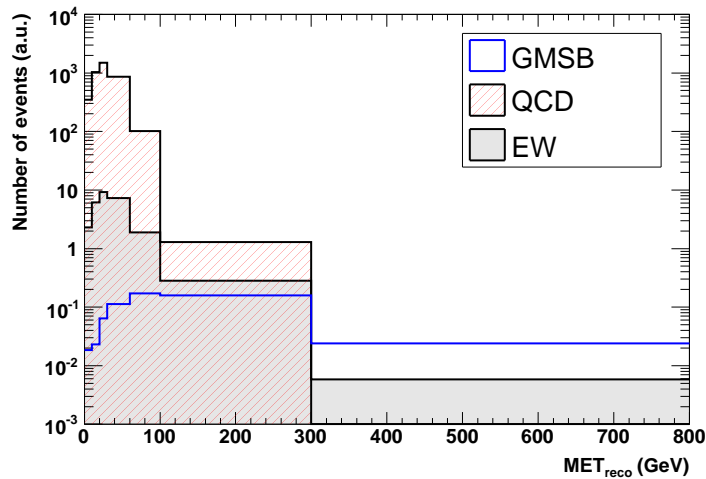

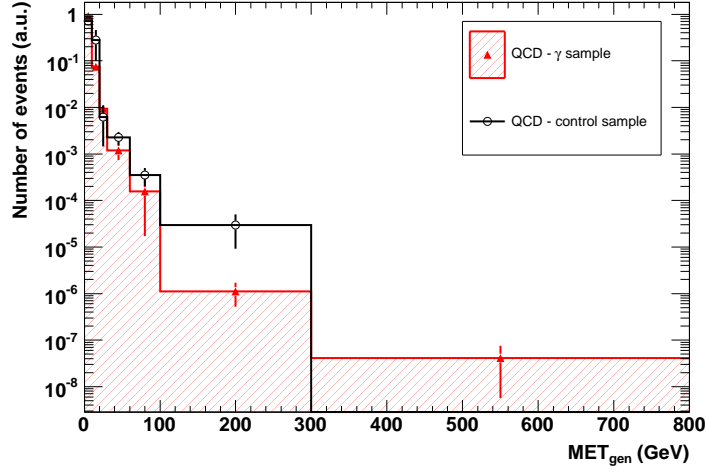Figure 5.23: $\not{E}_T$ distribution of the different components of the QCD control sample.

Figure 5.24: Distribution of $\not{E}_T^{gen}$ for the QCD components of the γ sample and the QCD control sample.
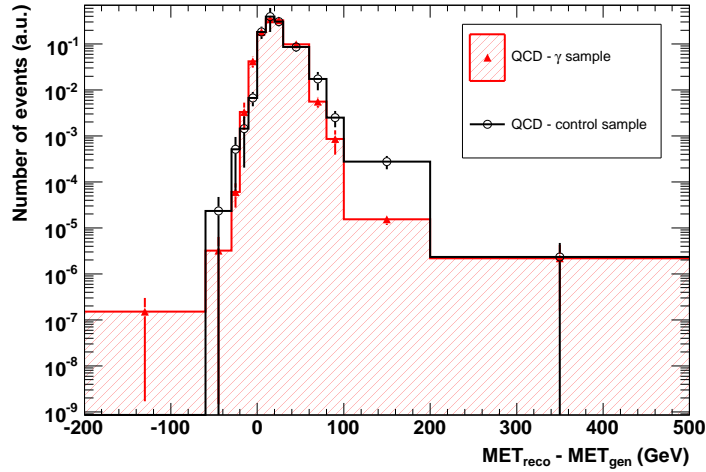

Figure 5.25: Distribution of $\Delta_{\not{E}_T} = \not{E}_T - \not{E}_T^{gen}$ for the QCD components of the γ sample and the QCD control sample.

5.9 Systematics

There are several systematics which can affect the extraction of GMSB signal yield both involving the signal and background modeling. Since this is a discovery analysis and not a precision measurement of the cross section, the systematics related to the signal are less relevant than background ones. In addition, given that the signal-over-background ratio of this analysis is quite large in the high $\displaystyle{\not}E_{\mathrm{T}}$ range, as shown in section 5.7, systematics uncertainties on background are expected to be not too large.

The real danger in this analysis, especially for early discoveries where the number of observed events is small, is represented by the tails in the resolution of the reconstructed quantities and they need to be taken under control. The most important source of systematic uncertainties is related with the $\displaystyle{\not}E_{\mathrm{T}}$ measurement. Since the $\displaystyle{\not}E_{\mathrm{T}}$ distribution of selected events is used to extract the signal yield, tails in the background distribution can fake the presence of signal events and any uncertainties related with $\displaystyle{\not}E_{\mathrm{T}}$ measurement is directly propagated to the final results of the analysis.

5.9.1 Theoretical uncertainties

The sources of theoretical uncertainties on signal and background can be summarized as [66]:

- the effect of neglecting higher order corrections to the coupling constants in the matrix element calculation of the physics process;

- the experimental precision of the SM parameters, which appear in the matrix element calculation;

- the parton showering, which describes the QCD radiation of outgoing partons from the hard process;

- the fragmentation model, which describes the hadronization using phenomenological models tuned with experimental data;

- the description of the underlying event, which includes all the remnant activity from the same pp interaction, the Initial State Radiation (ISR), and the pile-up;

- the description of the Parton Density Functions (PDFs) used to model the proton structure in the pp collision;

- the definition of Q^2 energy scale of the interaction.

Previous studies performed by CDF and D0 experiments at Tevatron, whose results are reported in [67] and [68] respectively, indicate that the main systematic uncertainties on the GMSB signal efficiency come from the initial/final (ISR/FSR) state radiation (10%) [2], the PDF description (5%) and the Q^2 energy scale of the interaction (3%).

Large MC statistics, especially for the background, is needed to perform detailed studies on the theoretical uncertainties in the LHC physics environment. The data will be used to understand the accuracy of the MC predictions in describing the SM background. A detailed study of the systematics described so far will be performed in future upgrades on this analysis and more precise estimates will be determined when the first data will be taken.

5.9.2 Experimental uncertainties

The main sources of systematic uncertainties associated with the detector measurements are discussed in this section. The estimate of most of the uncertainties is taken from the Technical Design Report of the CMS experiment [69].

Luminosity uncertainty

The measurement of the luminosity $\mathcal{L}$ is used to monitor the LHC performance in real time and to provide an overall normalization needed by cross section measurements [70]. In fact, the uncertainty on the luminosity $\mathcal{L}$ is almost linearly propagated to an uncertainty on the measurement of the cross section σ since

$$\sigma \propto \frac{1}{\mathcal{L}} \ . \tag{5.12}$$

The goal of the relative measurement of $\mathcal{L}$ is to determine in real time the average $\mathcal{L}$ in 0.1 s with a 1% statistical accuracy. This is obtained both by using signals from the forward hadron calorimeter and by using a set of purpose-built particle tracking telescopes based on single-crystal diamond pixel detectors, called the Pixel Luminosity Telescope (PLT).

The determination of the absolute scale of $\mathcal{L}$ is performed by using the measurements of pp total cross section and the measurement of the production rates for Ws and Zs. The measurement of the pp total cross section at % level will be performed by the TOTEM experiment [71], which will operate

---

[2]The systematic effects of ISR and FSR are the dominant. The quoted systematic error is determined by turning ISR off only or turning FSR off only.

at the luminosity of of $\mathcal{L} = 10^{28}$ cm^{-2} s^{-1}. This measurement, which is luminosity independent, combined with the the relative measurement performed at CMS can be used to extract the real time luminosity.

In addition, the measurement of the production rate of vector bosons can be used to calculate the integrated luminosity of a given sample of data with high accuracy. In this case, an important challenge will be to control the uncertainties associated with theoretical estimates of the cross section and the modeling of the detector acceptance [72].

The design goal for the precision of the absolute scale of the luminosity measurement at CMS is 5%, which is assumed to be achieved after 1 fb^{-1} of collected data. For integrated luminosities of less than 1 fb^{-1}, it is assumed that the precision is limited to 10%.

Electromagnetic calibration and energy scale uncertainties

There are two systematic uncertainties related with electromagnetic energy measurements: the uncertainty on the energy resolution and the one on the absolute energy scale.

At CMS start-up, the ECAL crystals are expected to be pre-calibrated at $\approx 2\%$, by combining different methods performed in laboratories and in test beam facilities (see details in section 3.3.2). In the very early period of data taking, the calibration precision will be improved to $\approx 1\%$ using the π^0 mass constraint in $\pi^0 \to \gamma\gamma$ decays (see). The design goal precision of 0.5% will be reached with about 5 fb^{-1} of integrated luminosity using isolated electrons from W decays, as estimated for MC studies. Systematics on energy resolution can be estimated by comparing data and MC distributions of known reconstructed quantities, as the width of Z boson.

The absolute energy scale can be determined using the Z mass constraint in $Z \to ee$ decays, and it is expected to be measured to a precision of about 0.05%.

For this measurement the absolute electromagnetic energy scale is more important than the energy resolution, since reconstructed photons and electrons are not used to reconstruct any physics resonance. Given that the absolute energy scale is measured with high precision, the systematic uncertainties discussed in this section are almost negligible compared to the other sources of uncertainties.

Missing transverse energy uncertainties

The $\slashed{E}_{\mathrm{T}}$ mis-measurement is mainly caused by:

- limited precision of the precalibrations of calorimeters (mostly HCAL);

- non-linearity of the ECAL+HCAL combined system in the LHC physics environment;

- dead channels;

- noisy channels.

The first two systematics affect the absolute scale of both the jet response and the $\not{E}_{\mathrm{T}}$. For this reason the jet calibration can be used to calculate correction coefficients to improve the $\not{E}_{\mathrm{T}}$ measurement.

Given the limitations of the precalibrations of the calorimeters, an overall uncertainty of 15% is expected for the "day-one" absolute jet energy scale. During data taking the γ+jet calibration [73] and the hadronic W boson mass calibration in $t\bar{t}$ events [74] will give the best estimates for the accuracy on the absolute jet energy scale.

The jet calibration using γ+jet events is based on the energy balance in the transverse plane between the photon and the recoiling jet, which in principle has a transverse momentum equal in module and opposite in direction to the photon. Given the large statistics this method can be used also in the early period of data taking. The main systematic uncertainties are due to 1) the transverse momentum unbalance due to extra jets produced by the presence of initial state radiation of the colliding partons, 2) the fact that the jet energy is different from the outgoing parton energy and depends on the specific jet reconstruction algorithm used. These uncertainties are currently estimated to be about 10% (3%) for jet P_T around 20 GeV (above 50 GeV).

With an integrated luminosity larger than 1 fb^{-1}, the W mass constraint can be used to calibrate the jet energy scale in $t\bar{t} \to bWbW \to bq\bar{q}bl\nu$ events. In this case, the largest systematic uncertainty comes from the pile-up and it is estimated around 3% for jet P_T larger than 50 GeV.

The detector failures, including the the presence of dead/noisy isolated channels or entire readout modules of the calorimeters, can be sources of systematic uncertainties in the $\not{E}_{\mathrm{T}}$ resolution, as discussed in detail [75]. Figure 5.26 show the distribution of reconstructed $\not{E}_{\mathrm{T}}$ in QCD jet events, in absence of detector failures and in three different scenarios where 1%, 3% and 5% percent of the ECAL and HCAL readout channels are noisy. The tails in the $\not{E}_{\mathrm{T}}$ distribution due to the noisy channels are dangerous since background events with large $\not{E}_{\mathrm{T}}$ values can fake the GMSB signal signature. Corrections to the $\not{E}_{\mathrm{T}}$ measurement to take into account dead/noisy channels of the calorimeters will be calculated "in situ" when first data will be available.

Due to the complex LHC physics environment, it is expected that systematic uncertainties on $\not{E}_{\mathrm{T}}$ reconstruction will be not completely understood in the first period of data taking. For this reason, it is important to use also
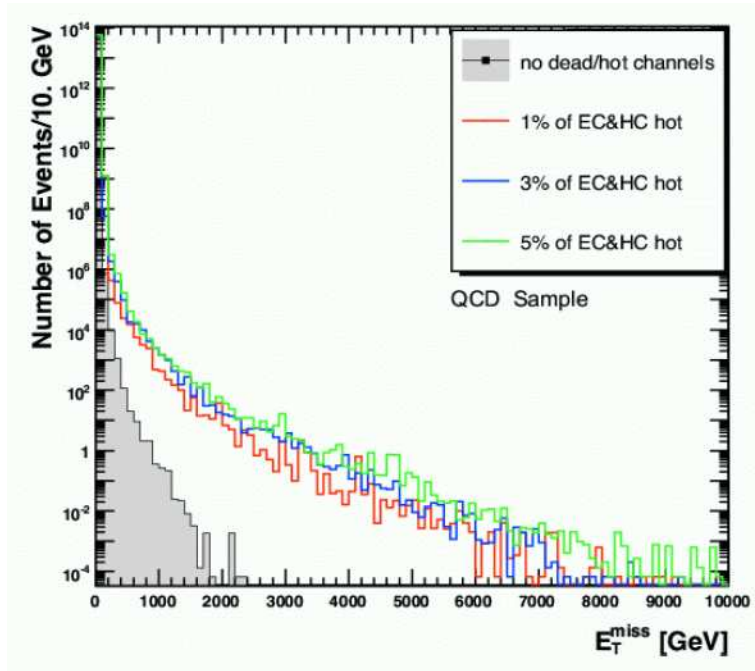
Figure 5.26: Distribution of $\not{E}_T$ for the QCD jet events. Shaded histogram is the reference distribution corresponding to no channels with detector problems. The red, blue and green distributions refer to the scenarios where 1%, 3% and 5% of the ECAL and HCAL readout channels are noisy [75].

control samples to estimate the background shape and the systematics on $\not{E}_T$ directly from data, as discussed in detail in section 5.8.

In conclusion, theoretical systematics play a secondary role in this discovery analysis, while $\not{E}_T$ mis-measurements can be sources of large systematic experimental uncertainties. In particular, the tails in the $\not{E}_T$ distribution of background events are dangerous since they can fake the presence of signal events.

Chapter 6

Discovery Potential

In this chapter, the discovery potential of SUSY for GMSB in the channel $\tilde{\chi}_1^0 \to \tilde{G}\gamma$, is discussed. The definition of signal significance is given in section 6.1. Section 6.2 describes the minimum integrated luminosity needed at LHC to observe this channel, as a function of the parameter Λ of the model. The possible future upgrades of this analysis are discussed in section 6.4. Uncertainties due to the systematic effects are no yet included in the results.

6.1   Signal significance

In high energy physics, significance S is usually meant as the number of standard deviations an observed signal is above the expected background fluctuations [76]. A given value of S corresponds to a probability that the observed signal is caused merely by fluctuations of the background, and this probability is obtained by performing the corresponding integrals of the standard Gaussian distribution. For example, a value of significance equal to S_x means that the probability of a background fluctuation to be more than the signal expected, is equal to the following integral of the standard Gaussian function

$$P(S_x) = 1 - \int_{-\infty}^{+S_x} \frac{1}{\sqrt{2\pi}} \cdot e^{\left(-\frac{t^2}{2}\right)} dt \quad . \tag{6.1}$$

The general agreement to claim a discovery in high energy physics, is that the value of S of a signal, measured in a single experiment, should exceed five and the corresponding one-sided Gaussian probability, defined in equation 6.1, is $P(5) \simeq 2.9 \cdot 10^{-7}$.

As anticipated in section 5.6, the extraction of signal (N_{GMSB}) and background (N_{EW} and N_{QCD}) yields is based on a likelihood fit to the $\not{E}_T$ distribution. Two different hypotheses are considered, the "null hypothesis" as-

suming that the observed distribution is due to background only, and an "alternative hypothesis" assuming the presence of both signal and background components. For the first hypothesis a fit, where N_{EW} and N_{QCD} are floating parameters and N_{GMSB} is fixed to zero, is used to calculate the value of likelihood $\mathcal{L}_B$. For the second hypothesis, a fit, where N_{GMSB} is also floating, is used to calculate the likelihood $\mathcal{L}_{S+B}$.

The definition of significance S_{L2} is

$$S_{L2} = \sqrt{2 \cdot (\ln \mathcal{L}_{S+B} - \ln \mathcal{L}_B)} \quad .\qquad (6.2)$$

The significance S_{L2} is an aleatory variable with a given probability density function. The distribution is reproduced by generating several toy Monte Carlo (MC) experiments.

For each experiment, signal and background events are generated using the $\not{E}_\mathrm{T}$ distribution after applying the selection criteria described in section 5.5.3. For each sample, the likelihood fit is used to extract the value of S_{L2}. Figure 6.1 shows the resulting S_{L2} distribution for the $\mathcal{L}_{int} = 150$ pb^{-1} $\Lambda = 140$ TeV case.
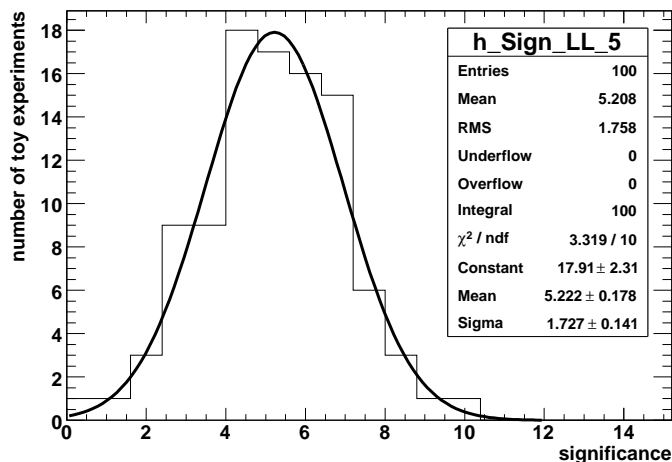

Figure 6.1: Distribution of signal significance S_{L2} obtained with 100 toy Monte Carlo experiments, for an integrated luminosity of 150 pb^{-1} and $\Lambda = 140$ TeV.

6.2 Discovery luminosity

The definition of discovery luminosity $\mathcal{L}_{int}^{disc}$ introduced by the LEP experiments at CERN, is the minimum integrated luminosity at a collider such that, in the 50% of the experiments repeated in the same conditions, the probability for the number of background events to fluctuate to more than the observed number of signal events is equal to $2.9 \cdot 10^{-7}$, corresponding to the one-sided integral of a standard Gaussian distribution between 5 and $+\infty$ (i.e. 5σ discovery).

According to this definition, the expected signal significance is calculated as the median of the S_{L2} distribution. It has to be noted that this definition of discovery luminosity provide only an estimate of the integrated luminosity needed for the discovery. For example, when performing a single experiment the probability to require an integrated luminosity for discovery larger than the estimated $\mathcal{L}_{int}^{disc}$ is 50%.

The signal significance S_{L2} as a function of the integrated luminosity, is shown in figure 6.2 for different Λ values. The data for a given value of parameter Λ are fitted with a $\sqrt{\mathcal{L}_{int}}$ function[1].

Since the signal cross section depends on Λ, $\mathcal{L}_{int}^{disc}$ needs to be extracted for different Λ values. Figure 6.3 shows the discovery luminosity for $S_{L2} = 5$, as a function of parameter Λ. $\mathcal{L}_{int}^{disc}$ rises exponentially with the parameter Λ [2]. As shown, GMSB signal can be discovered with an integrated luminosity of about 100 fb^{-1} in a wide range of parameter Λ, up to $\Lambda \sim 300$ TeV. GMSB models with a parameter Λ which lies just above the Tevatron limit ($\Lambda > 80$ TeV) [68] could be discovered at the beginning of the data taking, with an $\mathcal{L}_{int} \mathcal{O}(10)$ pb^{-1}.

---

[1]The significance is expected to scale as the square root of the integrated luminosity $\mathcal{L}_{int}$. This is shown for a counting-based significance S_{c1}, defined as:

$$S_{c1} = \frac{N_s}{\sqrt{N_b}} = \frac{\varepsilon_s \cdot \sigma_s \cdot \mathcal{L}_{int}}{\sqrt{\varepsilon_b \cdot \sigma_b \cdot \mathcal{L}_{int}}} = \frac{\varepsilon_s \cdot \sigma_s}{\sqrt{\varepsilon_b \cdot \sigma_b}} \cdot \sqrt{\mathcal{L}_{int}} \qquad (6.3)$$

where $N_s(N_b)$, $\varepsilon_s(\varepsilon_b)$ and $\sigma_s(\sigma_b)$ are respectively the selected number of events, the selection efficiency and the cross section of the signal (background).

[2]It can be demonstrated that

$$\mathcal{L}_{int}(\Lambda) \approx \frac{S_{L2}^2 \cdot \varepsilon_b \cdot \sigma_b}{\varepsilon_s^2(\Lambda) \cdot \sigma_s^2(\Lambda)} \propto e^{2\Lambda} \quad , \qquad (6.4)$$

where signal and background efficiencies and cross sections for the background, do not depend on Λ, while the signal cross section decreases exponentially as $\sigma_s(\Lambda) \propto \exp(-\Lambda)$ (see figure 2.4).
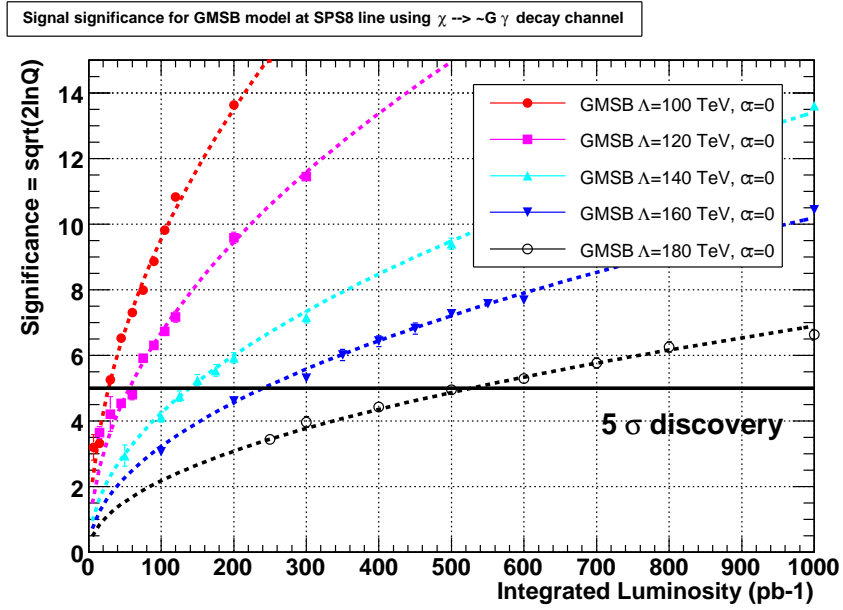
Figure 6.2: Signal significance S_{L2} as a function of integrated luminosity of collected data for different GMSB models generated.
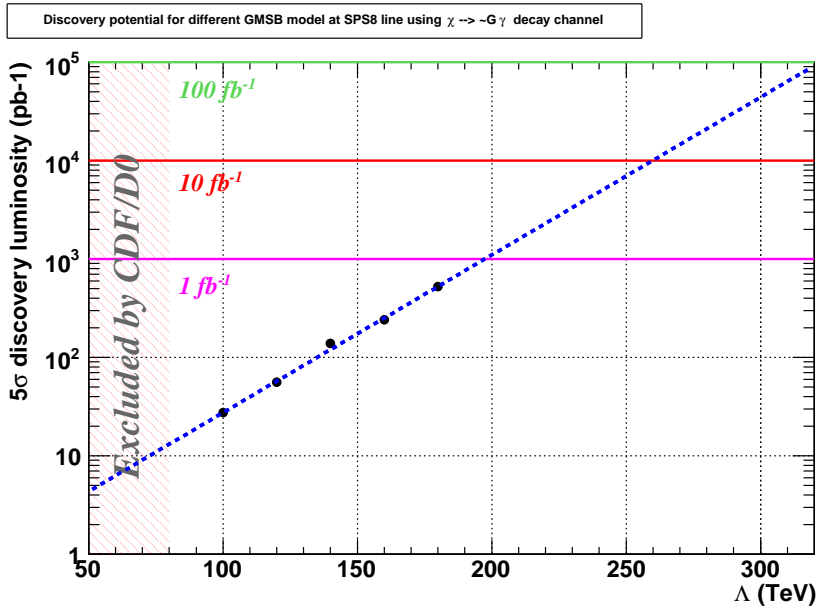

Figure 6.3: Discovery integrated luminosity $\mathcal{L}_{int}^{disc}$ as a function of parameter Λ.

132

6.3 Exclusion luminosity

Several theoretical models of the physics beyond the SM have been proposed in the last twenty years. Even in absence of discovery, the experiments at LHC can reduce the number of these models and set limits in the parameter space by excluding models which do not fit the collected data.

The amount of statistics needed to exclude a given model can be quantified by the so-called "exclusion luminosity" ($\mathcal{L}_{int}^{excl}$) defined as the minimum integrated luminosity such that, in the 50% of the experiments repeated in the same conditions, the probability, for the number of expected-signal-plus-background events to fluctuate to a value lower than the number of background events, is equal to 2.27%. This probability corresponds to the one-sided integral of the standard Gaussian distribution between 2 and $+\infty$ (i.e. 2σ exclusion).

The $\not{E}_T$ distribution is generated assuming that only background is present. The likelihood ratio is then extracted using two hypothesis. In the first hypothesis one assumes that the observed $\not{E}_T$ distribution is due to signal-plus-background. A fit to the $\not{E}_T$ distribution is performed, where N_{EW} and N_{QCD} are floating parameters and N_{GMSB} is fixed to the expect value of signal events for a given integrated luminosity. The value of the likelihood $\mathcal{L}'_{S+B}$ is then calculated. In the second hypothesis, the $\not{E}_T$ distribution is due to only background, and a fit where N_{GMSB} is fixed to zero is used to calculate the likelihood $\mathcal{L}'_B$. The significance S'_{L2} is

$$\mathrm{S}'_{L2} = \sqrt{2 \cdot \left(\ln \mathcal{L}'_B - \ln \mathcal{L}'_{S+B} \right)} \quad . \tag{6.5}$$

As for the discovery luminosity, the distribution of S'_{L2} is obtained by generating several toy MC experiments and its median is used to calculate the exclusion luminosity.

The significance S'_{L2} as a function of the integrated luminosity, is shown in figure 6.4 for different Λ values. The data for a given value of parameter Λ are fitted with a $\sqrt{\mathcal{L}_{int}}$ function.

Figure 6.5 shows the exclusion luminosity for $\mathrm{S}'_{L2} = 2$, as a function of parameter Λ. As shown, GMSB signal can be excluded with an integrated luminosity of about 100 fb^{-1} in a wide range of parameter Λ, up to $\Lambda \sim 350$ TeV. GMSB models with a parameter Λ which lies just above the Tevatron limit ($\Lambda > 80$ TeV) [68] could be excluded at the beginning of the data taking, with less than 10 pb^{-1}.
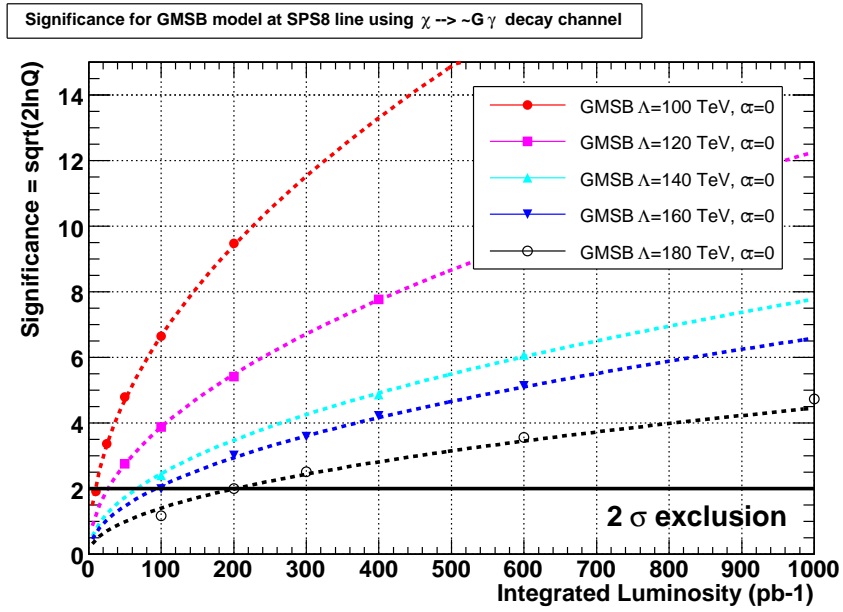
Figure 6.4: Significance S'_{L2} as a function of integrated luminosity of collected data for different GMSB models generated.
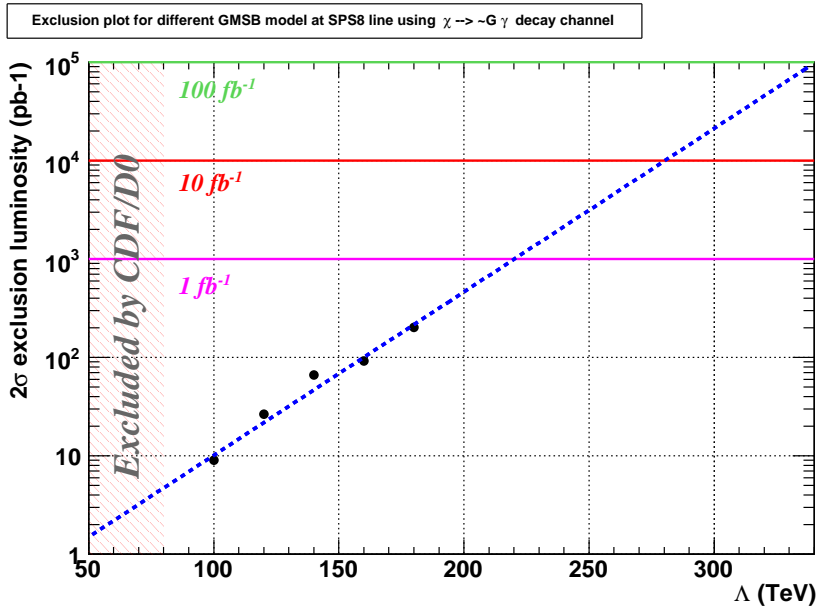

Figure 6.5: Exclusion integrated luminosity $\mathcal{L}_{int}^{excl}$ as a function of parameter Λ.

6.4 Future upgrades

This section describes the possible future upgrades of this analysis. They are divided in three main areas concerning event selection, background and $\tilde{\chi}_1^0$ lifetime studies.

6.4.1 Event selection upgrades and studies

Trigger studies

The study of the trigger selection represents an important issue, as discussed in the section 5.5.1. It has been shown that trigger efficiency for signal events is around 40%, mostly due to the photon isolation criteria. It is important to investigate if signal efficiency can be improved, for example by using triggers with relaxed thresholds.

Single γ selection

Around 20% of signal events (this fraction is slightly model dependent) has only one photon in the final state, as shown in figure 4.1, and it is rejected by the $\gamma\gamma$ selection. These events can be used to extract the GMSB event yield. Two independent samples, one corresponding to the $\gamma\gamma$ sample and the other with only one selected photon, can be created, each having different selection criteria (tighter for the sample with one photon). They can be combined in a simultaneous likelihood fit to improve the significance of the measurement.

Jet variables

Jet variables have been investigated in section 5.5.2 and they show a good discriminating power between signal and background. Such variables were not used in the final selection criteria, in order to not include the systematics related to jet reconstruction. Nevertheless, jets could be used in future to further improve the background rejection, in particular when the detector systematics will be under control. This will require a detailed study of the uncertainties related to the non-compensating calorimeter system, in terms of jet resolution and calibration of the jet energy scale.

6.4.2 Background studies

Control samples

As shown in section 5.8, the background contamination can be estimated directly from data using control samples.

The EW background can be determined by using an $e\gamma$ sample, where the reconstructed photon with highest transverse momentum of the event is replaced by an electron. However the lack of MC statistics does not allow to perform a detailed comparison between control sample and $\gamma\gamma$ sample in the high $\not{E}_{\mathrm{T}}$ region (see figure 5.21). These studies have to be repeated with substantially larger statistics.

Also for QCD background the statistics in not sufficient and no clear technique to extract $\not{E}_{\mathrm{T}}$ shape from data has been found. The approach of using the MC shape for the likelihood fit and different control samples to estimate the systematics on $\not{E}_{\mathrm{T}}$ resolution, must be performed with a dedicated MC production.

Monte Carlo samples

When modeling the background, some EW contributions like WW, WZ, ZZ, $W + \gamma$ and $Z + \gamma$, were not included. Their effect should be small as discussed in section 4.3.3. Nevertheless, these samples can be included in the future upgrades of this analysis to have a more detailed description of the background contamination.

6.4.3 $\tilde{\chi}_1^0$ lifetime studies

The lifetime of the neutralino is one of the free parameters of the GMSB models, as discussed in section 2.3. Different experimental signatures are expected depending on the neutralino lifetime. If the decay length of the neutralino is large enough and it decays inside the detector, the measurement of its lifetime can be performed. Two possible methods for lifetime determination are briefly presented in the following and will be investigated in details by the future studies.

Converted photons for lifetime determination

If the neutralino decays between the center of CMS and the ECAL, photons from $\tilde{\chi}_1^0 \to \tilde{\mathrm{G}}\gamma$ can be detected. Such photons do not point to the primary vertex, because 1) there is a displacement between the photon production vertex and the primary vertex, 2) the $\vec{p}$ of the photon is not parallel to the neutralino's one. Given that the ECAL crystals are almost projective, the photon hits the crystal frontal face with a non-zero angle. As a result, the energy deposit involves many more crystals and the photon cluster gets an eccentrical shape around the impact point [77].

The shape of the photon cluster is therefore correlated with the production vertex of the photon (i.e. the neutralino decay vertex) and depends on the kinematics of the decay. Then, the shape of the cluster can be used to extract the $\tilde{\chi}_1^0$ lifetime [57].

A more precise method is based on the reconstruction of photons which convert to e^+e^- pair in the tracker material. If the photon converts in the tracker material creating an e^+e^- pair, one or two tracks can in principle be reconstructed by using dedicated tracking algorithms [78]. Such tracks are non-pointing to the primary vertex, for the same reasons discussed so far. The e^+e^- track direction provides a good estimate of the momentum of the initial photon. This information is similar, but more precise, to the one given by the eccentricity of the cluster shape. Since about 40% of signal photons converts in the tracker material, this is an interesting method to investigate for the determination of $\tilde{\chi}_1^0$ lifetime.

$\tilde{\chi}_1^0 \rightarrow \tilde{\mathbf{G}}Z$ decay

The neutralino decays in $\tilde{G}Z$ final state in $\approx 10\%$ of the cases (model dependent). By reconstructing the Z decays to e^+e^- and $\mu^+\mu^-$ ($BR(Z \rightarrow ee/\mu\mu) \sim 6\%$), the Z decay vertex (coincident with the $\tilde{\chi}_1^0$ decay vertex) is obtained, providing a very precise measurement of the decay length of $\tilde{\chi}_1^0$. Given the small total selection efficiency $\varepsilon_{tot} \approx BR(\tilde{\chi}_1^0 \rightarrow \tilde{G}Z) \times BR(Z \rightarrow ee/\mu\mu) \times \varepsilon_{reco}^Z \approx 0.6\% \times \varepsilon_{reco}^Z$, this analysis will be feasible only with a large amount of integrated luminosity.

Chapter 7

Conclusions

The Standard Model (SM) of fundamental interactions is a successful theory describing strong, weak and electromagnetic interactions of elementary particles. In spite of the perfect agreement with all experimental observations, there are some theoretical unsolved problems in the SM. Supersymmetry (SUSY) is one of the plausible theory for the physics beyond the SM.

Theories with Gauge Mediated Supersymmetry Breaking (GMSB) are particularly interesting since they allow a natural suppression of the Flavour Changing Neutral Currents and, in addition, foresee relatively high production cross section and have a very distinctive experimental signature. Search for SUSY with gauge-mediated breaking has been already performed by experiments at LEP and Tevatron colliders, but results had shown no evidence of new physics.

The Compact Muon Solenoid (CMS) experiment at the Large Hadron Collider (LHC), in construction at the CERN laboratories of Geneve, will benefit of a larger energy in the center of mass of $\sqrt{s} = 14$ TeV, compared to the $\sqrt{s} = 1.96$ TeV of the Tevatron, thus permitting the possible creation of heavy SUSY particles above the current Tevatron reach. In addition, the very high luminosity of the machine $\mathcal{L} = 10^{34} \text{cm}^{-2}\text{s}^{-1}$ will allow a relatively large production rate of such rare events, to claim discoveries or exclusions in the early data taking. The search for SUSY is one of the most important items in the research program of the CMS experiment.

In this thesis, the study of the $\tilde{\chi}_1^0 \rightarrow \tilde{G}\gamma$ prompt decay within GMSB models, with a full simulation of the CMS detector, is presented. The presence of two high energy photons and large missing transverse energy in the final state due to gravitinos ($\tilde{G}$), makes the experimental signature of such events very clear.

For this analysis, the minimal GMSB model with only one dimensioned parameter Λ, which determines the overall mass scale of SUSY particles, is

considered. For the values of Λ investigated ($100 < \Lambda < 180$ TeV), the event selection is based on the requirement of at least two isolated photons in the ECAL barrel ($|\eta| < 1.5$), with P_T of the first and second photons with highest transverse momentum of the event, larger than 90–110 GeV and 30 GeV, respectively. The $\displaystyle{\not}E_T$ of the event is determined from energy deposited in the calorimeters for $|\eta| < 5.2$. Since $\displaystyle{\not}E_T$ is the most discriminating variable between signal and background, the $\displaystyle{\not}E_T$ distribution is used to extract the signal yield using a maximum likelihood fit. This approach, compared to a cut&count technique, offers the advantages that the systematics can be taken into account in the modeling of the $\displaystyle{\not}E_T$ shapes, which can be obtained directly from data using control samples. In addition, the background normalization is extracted from the fit itself. The electroweak background can be determined by using an $e\gamma$ sample, where the reconstructed photon with highest transverse momentum of the event is replaced by an electron. For the QCD background, the approach of using the MC shape of $\displaystyle{\not}E_T$ distribution for the likelihood fit and different control samples to estimate the systematics on $\displaystyle{\not}E_T$ resolution is being investigating.

The discovery potential of SUSY for GMSB, in the channel $\tilde{\chi}_1^0 \to \tilde{G}\gamma$, has been studied. The GMSB signal can be discovered with an integrated luminosity of about 100 fb^{-1} in a wide range of parameter Λ, up to $\Lambda \sim 300$ TeV. GMSB models with a parameter Λ which lies just above the Tevatron limit ($\Lambda > 80$ TeV) could be discovered at the beginning of the data taking, with an integrated luminosity of $\mathcal{O}(10)$ pb^{-1}. This result makes the search of Supersymmetry with high energy photons a very promising analysis for the CMS startup.

There are some possible future upgrades of this analysis and further studies to be investigated concerning the selection, the background and the $\tilde{\chi}_1^0$ lifetime measurement.

Some reconstructed quantities, like the P_T and the η of jets, are not included in this analysis, since they are in general very affected by systematics. These quantities could be used in future to further improve the background rejection.

When modeling the background, some EW contributions like WW, WZ, ZZ, $W + \gamma$ and $Z + \gamma$, were not included, but their effect on this analysis is expected to be small. Nevertheless, these samples can be included in the future upgrades of this analysis to have a more detailed description of the background contamination.

The $\tilde{\chi}_1^0$ lifetime is a free parameter of the GMSB model. If the $\tilde{\chi}_1^0$ decay length is large enough and it decays inside the detector, the measurement of its lifetime can be performed. Some methods to determine the $\tilde{\chi}_1^0$ lifetime

have been proposed and will be investigated in details by the future studies. One of these methods is based on the reconstruction of photons from $\tilde{\chi}_1^0 \to \tilde{G}\gamma$ which convert in an e^+e^- pair in the tracker material. Since the photons do not point to the primary vertex, the e^+e^- track momentum is correlated to the $\tilde{\chi}_1^0$ decay vertex and can be used to extract the $\tilde{\chi}_1^0$ lifetime.

Appendix A

The ECAL High Voltage System

A custom HV power supply system [79] has been designed for the ECAL in collaboration with CAEN Company [80]. The system is based on a standard control crate (SY1527) hosting 8 boards (A1520E) expressly designed for this application. Each board contains 9 HV channels implemented as a separate module, thus permitting a major flexibility in case of channel failure. In total the system is composed of 18 crates SY1527 and 144 boards A1520E. Each channel is designed to give a bias voltage to 50 capsules (a capsule contains two APDs coupled to back of each crystal) from 0 to 500 V. Each of the 36 ECAL supermodule requires 34 HV channels, taken from 4 boards (one spare channel out of two boards is left). An external automatic setup for HV channels calibration completes the system in order to guarantee output voltage and current measurement precision.

Since the APD gain has a quite high dependence on the bias voltage, the photodetectors require a very stable power supply system, as gain fluctuations directly contribute to the constant term of the energy resolution[1]. The contribution to the constant term, due to HV stability, should not exceed 0.2%. To satisfy this request, the voltage stability has to be of the order of 60-65 mV, for $M = 50$ and $\alpha_V = 1/M \cdot dM/dV = 3.1 \pm 0.1\%/V$.

An acceptance test on the long term stability is performed on each A1520E board on reception. The test foresees setting a voltage $V_{set} = 380$ V and the corresponding output voltage of the 9 channels are measured every 10 minutes, for around 30 days. Two examples of the output $V(t)$, measured as a function of time, are shown in figure A.1, for both a stable channel and a chan-

---

[1]The standard parametrization of energy resolution is $(\sigma(E)/E)^2 = (a/\sqrt{E})^2 + (b/E)^2 + C^2$, where a is the stochastic term, b the noise term and c the constant term

nel presenting a drift during the test. In both cases the day-night variations are clearly visible. The temperature in the laboratory is measured by 5 sensors located around the crate. Day-nigh variation and voltage-temperature correlation are shown in figure A.2. In the right plot, a temperature sensitivity of the voltage well inside the specifications is observed (the slope of the linear fit is $dV/dT \sim 3$ mV/$^\circ$C).
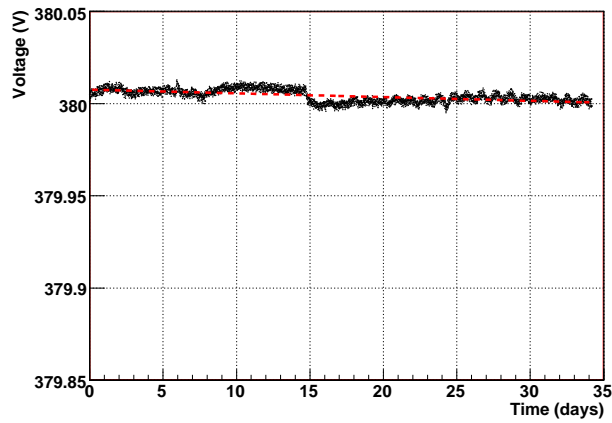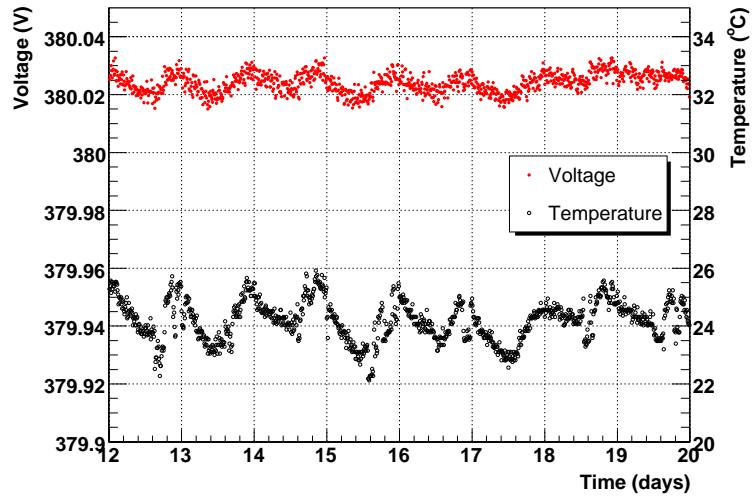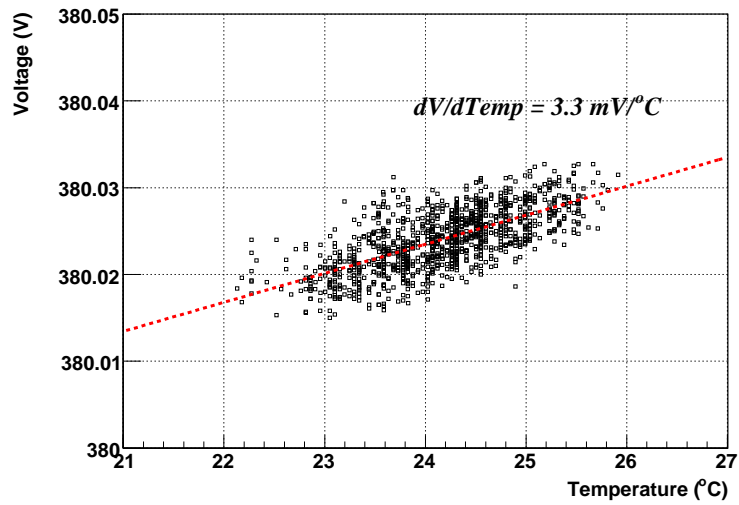

(a)
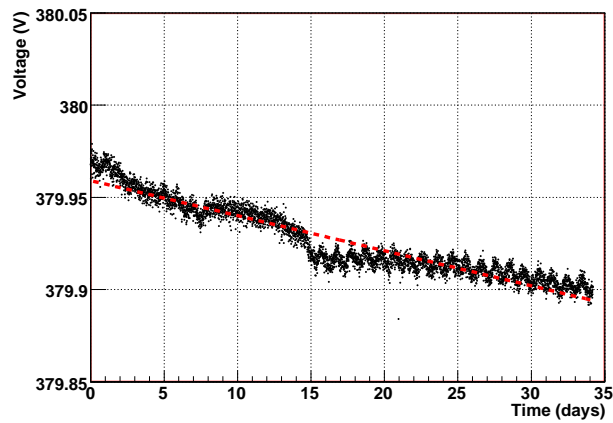
(b)

Figure A.1: Output voltage as a function of time for a stable channel (a) and for a channel outside the specifications (b)

Figure A.2: (a) Average of the 5 temperature measurements obtained by the temperature sensors located in the laboratory and voltage measurements taken in the same time interval. (b) Voltage values vs temperatures are shown; a linear fit is superimposed.

In almost all the channels which present a variation greater than 65 mV, the voltage measurements show a clear drift upwards or downwards and not a Gaussian-like behaviour. A channel is accepted if, after the fit of $V(t)$ with a first order polynomial function, the following conditions are satisfied:

- $\Delta V_{max} = \max(|V(t) - 380|) < 65$ mV

- fit slope < 2 mV /day

The distribution of ΔV_{max} is shown in figure A.3 for all the channels tested up to now.
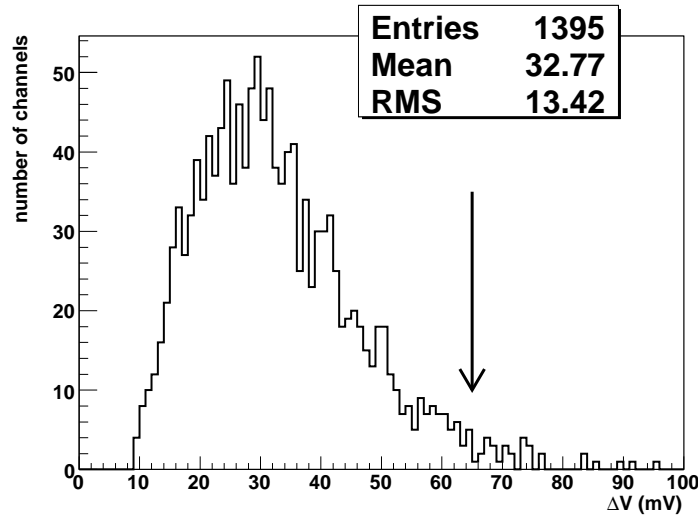
Figure A.3: Distribution of ΔV_{max}, the maximum difference between measured voltage and V_{set}. The channels having a value greater than 65 mV are rejected.

In conclusion, the HV system has been tested in the laboratory and during several ECAL test beam campaigns and the observed performances show that it is within the design specifications.

Appendix B

Intercalibration of ECAL with $\pi^0 \to \gamma\gamma$ decays

The $\pi^0 \to \gamma\gamma$ decays can be used for a rapid inter-calibration of the electro-magnetic calorimeter (ECAL) of CMS at the LHC startup. They may also provide an excellent monitoring tool of the ECAL performance in the long term. This appendix, describing the calibration study with the $\pi^0 \to \gamma\gamma$ decays, is organized as follows:

- The motivation for a fast *in situ* intercalibration using $\pi^0 \to \gamma\gamma$ decays is presented in section B.1.

- The online selection of $\pi^0 \to \gamma\gamma$ candidates using Level-1 trigger (L1) electro-magnetic (EM) candidates is described in section B.2.

- The fully simulated QCD samples used for the analysis are detailed in section B.3.

- The π^0 reconstruction algorithm, selection variables and reconstruction efficiencies are discussed in section B.4.

- The description of the calibration algorithm and the results obtained with simulated events are discussed in section B.5.

- The estimate of the time required to calibrate the whole ECAL is discussed in section B.6.

- Finally the estimate of the data rate in the High Level Trigger is shown in section B.7.

Part of the information on the LHC, the ECAL and the other CMS detectors, which are discussed in chapter 3, will be used in what follows.

B.1 Motivation for π^0 calibration

To fully exploit the CMS and ECAL physics potential, it is necessary to maintain an inter-calibration precision of $\sim 0.5\%$ level or better. Different methods can be used to achieve this design precision: pre-calibration at laboratories and *in situ* measurements.

The pre-calibration of the ECAL crystals is obtained by combining the results of three different calibration methods: a measurement of the light yield (precision around $\approx 4\%$) [36],[37], a precise inter-calibration with an electron beam (precision better than 0.5%) [37], and calibration using cosmic rays (precision around $2-3\%$) [38], [39].

During the LHC operation, the *in situ* calibration of the ECAL and fast monitoring will be crucial. At the beginning of the CMS operation, a very fast inter-calibration tool ("Energy Flow"), based on the ϕ symmetry of the released energy in a ring of crystals at a given pseudo-rapidity η, will be used to improve the pre-calibration [41].

To obtain a good global inter-calibration, this method must be combined with calibration algorithms using physics events, such as $Z \to e^+e^-$ [42] and $W \to e\nu$ [43] decays, to precisely inter-calibrate ECAL regions with different η (precision around $0.5-1\%$). The problem resides in the size of the sample that must be accumulated to reach the desired precision, i.e. ~ 1 fb^{-1} for the Z and > 5 fb^{-1} for the W, and the fact that calibration with W bosons requires the correct alignment of the tracking system.

In the LHC, the $\pi^0 \to \gamma\gamma$ decays are crucial to provide a fast *in situ* ECAL inter-calibration in the early days of the experiment [81]. Advantages and disadvantages of the π^0 calibration, compared to calibration algorithms with Z/W bosons, are summarized in the following items:

Advantages

- **Statistics**
  Very large number of neutral pions are produced in any proton-proton collision at the LHC. Therefore, the time required for the ECAL inter-calibration with π^0's is small compared to the calibration with Z/W bosons.

- **Tracker Independent**
  Being based on reconstruction of photon clusters in the electromagnetic calorimeter, $\pi^0 \to \gamma\gamma$ calibration does not depend on the performance of the tracker.

Disadvantages

- **QCD background contamination**
  Some experiments, like HERA-B [82], have already used low energy photons to calibrate calorimeters made of crystals with great precision, but in cleaner experimental environments. The π^0 calibration at CMS suffers from systematic effects due to the significant QCD background contamination.

- **Electronic noise**
  This calibration suffers from larger contribution from the electronic noise at low energy.

- **Low energy range and energy resolution**
  High energy π^0 candidates cannot be reconstructed because of the small opening angle between the photons compared to the granularity of the calorimeter. Using these photons, only energies below ~ 8 GeV are accessible. In addition, the energy measurement of these photons have a worse resolution compared to the high energy electrons coming from Z/W decay because the stochastic and noise terms are dominant with respect to the constant term (see equation 3.7). Since the statistical precision of the calibration constants depends linearly on the width of the invariant mass, a large number of reconstructed π^0 is needed achieve the desired precision.

- **Linearity**
  The π^0 calibration uses low energy photons which are much less energetic than photons produced in the high P_T physics events at the LHC. The linearity of the calorimeter response must be known at the level of 10^{-3} for the inter-calibration constants to be used over a wide energy range.

B.2 π^0 selection in the High Level Trigger

The total cross section of proton-proton collisions at the LHC is $\sigma_{TOT} \approx 100$ mb. Assuming an LHC luminosity of $\mathcal{L} = 2 \cdot 10^{33}$ cm^{-2}s^{-1}, an event rate of about 10^8 Hz is expected; about 10^2 Hz are Z/W events and less than 1 Hz are Higgs and SUSY events. In the remaining fraction of events, mostly QCD and minimum bias events (see section 3.2), large number of low energy π^0s (less than ten GeV) are produced, which, in principle, can be selected for ECAL calibration purpose.

The CMS Trigger System [83] is designed to reduce the large rate of events in two steps. The production rate of 10^8 Hz is reduced to a maximum of 50 kHz by the Level-1 (L1) Trigger, and subsequently to 10^2 Hz by the High Level Trigger (HLT). In the last step, most of the low energy π^0s useful for calibration are rejected by the HLT requirements, since these criteria are optimized for high P_T physics analysis. For this reason, a dedicated π^0 selection at HLT level is needed.

The idea is to look for π^0s in all the events which have passed the L1 trigger decision. The selection criteria of the L1 triggers are tuned to provide an output rate of around 20 kHz, in order to have a margin of safety of a factor ~ 2 with respect to the maximum L1 rate allowed. This rate is shared at 50% between muon and calorimeter triggers. The muon triggers are dominated by minimum bias events, whereas calorimeter triggers are mostly due to QCD jet events.

The π^0 selection, working in parallel with the other HLT triggers, is based on the use of electromagnetic objects of the L1 calorimeter trigger (L1 EM candidates) to identify ECAL regions of interest for a quick selection and reconstruction of π^0 candidates.

The analysis presented in this thesis is focused on the calibration of the ECAL barrel. One possible improvement on this analysis is the application of the same method to the endcaps.

B.2.1   L1 electromagnetic candidates

In the ECAL barrel, the L1 EM candidates are regions of 4×4 trigger towers, for a total of 20×20 crystals, with relevant electromagnetic deposit inside. Some criteria, based on calorimeter measurements without the tracker information, are applied by L1 trigger to distinguish between electromagnetic and hadronic energy deposits. As illustrated in figure B.1, each such candidate has fixed $\Delta\eta \times \Delta\phi = 0.35 \times 0.35$ dimensions in the ECAL geometry. A detailed discussion on such trigger objects can be found in [83].

Since each L1 EM candidate corresponds to about 1/4 of an ECAL super-module, there are $(4+4) \times 18$ possible L1 EM candidates in the whole barrel; anyway, only the 4 candidates with higher transverse energy are retained to be used by HLT algorithms.

In the standard HLT, L1 EM candidates are used as a starting point for the electron and photon reconstruction. In this application, they are used as seeds for a quick identification and reconstruction of π^0 candidates useful for calibration. This is discussed in the next section.
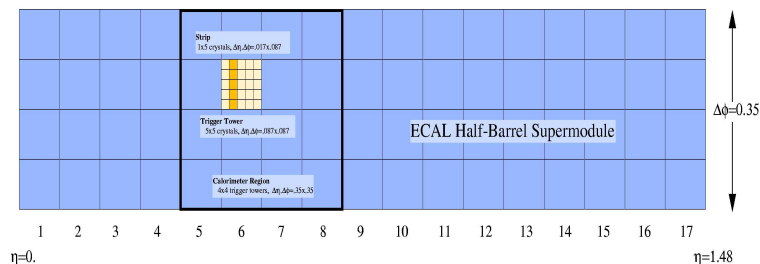
Figure B.1: Calorimeter Trigger Tower layout in one ECAL half barrel super module. The trigger towers are organized in calorimeter regions of 4×4 towers.

B.2.2 Seeding with L1 electromagnetic candidates

The 4 L1 EM candidates with higher energy are used to look for π^0 candidates in limited regions of the ECAL, hence reducing significantly the CPU time for processing event data. This allows an online analysis of all events accepted by the L1 trigger without any further rejection.

Within each 20×20 crystal region, photon candidates are created with a fast 3×3 clustering algorithm, and then combined to form π^0 candidates. This is shown schematically in the figure B.2 and discussed in detail in section B.4.

For each L1 EM candidate with at least one selected π^0 candidate, the reconstructed energy of a subset of crystals in the calibration stream is stored. Upon accumulating sufficient statistics, the calibration can be performed offline, as discussed in section B.5.

B.3 Description of Monte Carlo samples

In this analysis, fully simulated QCD jet events, in different bins of $\hat{P}_T$[1], and reconstructed with ORCA (version 8_7_4) [47], are used. These samples include pile-up events which are superimposed to signal events generated with PYTHIA [52], accordingly with a luminosity of $\mathcal{L} = 2 \cdot 10^{33}$ cm^{-2}s^{-1}. In what follows, these datasets are labeled as jm_03b_qcd_$\hat{P}_{low}$_$\hat{P}_{high}$, where $\hat{P}_{low}$ and $\hat{P}_{high}$ are, respectively, the lowest and highest $\hat{P}_T$ for each QCD jet sample.

Table B.3 summarizes the number of generated events N_{gen}, the L1 trigger

---

[1]See definition at section 3.4.
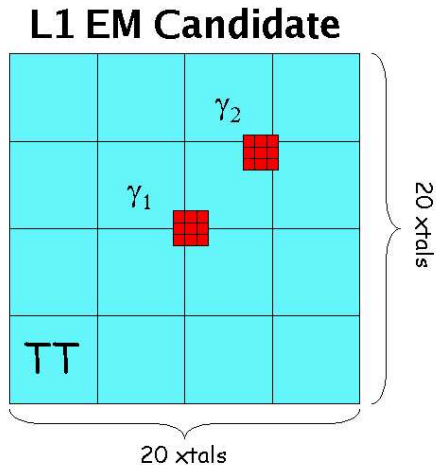
Figure B.2: Selection of π^0 candidates within the 20×20 region of a L1 EM candidate. Photon candidates are selected with a simple 3×3 clustering algorithm.

efficiency ϵ_{L1}, the production cross section σ, the effective cross section $\sigma_{L1}^{eff} = \sigma \cdot \epsilon_{L1}$, and the estimated L1 trigger rate $\mathcal{R}_{L1} = \epsilon_{L1} \cdot \mathcal{L} \cdot \sigma$ (with $\mathcal{L} = 2 \cdot 10^{33}$ cm^{-2}s^{-1}) for each sample.

The large uncertainty on $\mathcal{R}_{L1}$ at low $\hat{P}_T$ is due to the small trigger efficiency in this region. The cross section, the trigger efficiency and the trigger rate as a function of $\hat{P}_T$ are shown in figures B.3.

$\hat{P}_T$ range (GeV)	N_{gen}	σ (mb)	ϵ_{L1}	σ_{L1}^{eff} (10^{-4} mb)	$\mathcal{R}_{L1}$ (kHz)
$15 < \hat{P}_T < 20$	45k	1.5	$(5.1\pm1.1)10^{-4}$	7.7±1.6	1.53±0.32
$20 < \hat{P}_T < 30$	90k	0.6	$(1.54\pm0.13)10^{-3}$	9.26±0.78	1.85±0.16
$30 < \hat{P}_T < 50$	90k	0.15	$(9.85\pm0.33)10^{-3}$	14.7±0.5	2.95±0.01
$50 < \hat{P}_T < 80$	170k	0.02	$(4.76\pm0.05)10^{-2}$	9.52±0.10	1.90±0.02
$80 < \hat{P}_T < 120$	240k	0.03	$(12.73\pm0.07)10^{-2}$	3.82±0.02	0.764±0.004
$120 < \hat{P}_T < 170$	135k	0.005	$(37.1\pm0.1)10^{-2}$	1.86±0.06	0.371±0.001

Table B.1: Number of generated events N_{gen}, L1 trigger efficiency (ϵ_{L1}), production cross section (σ), the effective cross section ($\sigma_{L1}^{eff} = \sigma \cdot \epsilon_{L1}$), and the L1 trigger rate (at $\mathcal{L} = 2 \cdot 10^{33}$cm^{-2}s^{-1}) for QCD jet events in different regions of $\hat{P}_T$.
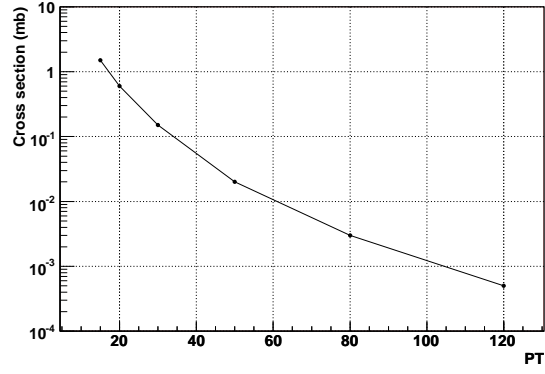
(a)
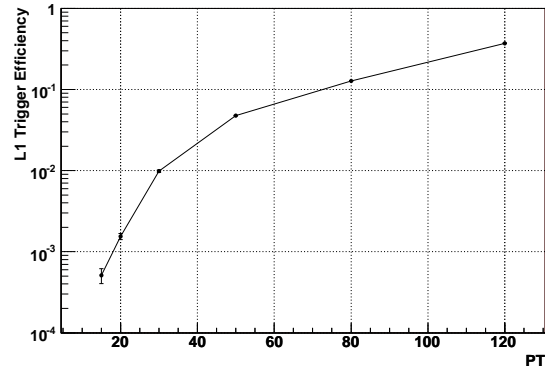
(b)
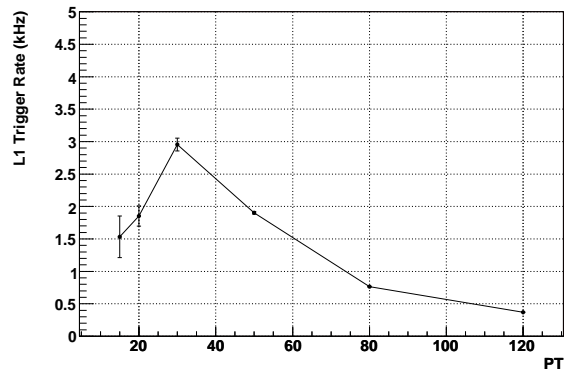
(c)

Figure B.3: Cross section (a), L1 trigger efficiency (b) and L1 trigger rate
(c) as a function of $\hat{P}_T$ of QCD jet samples.

B.4 π^0 reconstruction and selection

B.4.1 Selective Readout

At the L1 trigger level the ECAL channels are not all read out since the data volume would exceed the allocated space by a factor 20. In order to reduce this amount of data a selective readout is applied (see [84] for details).

The selective readout algorithm classifies the trigger towers of the ECAL in three different groups, by comparing energy deposited in each tower to 2 thresholds: high interest ($E_T > 5$ GeV), medium interest (2.5 GeV $< E_T < 5$ GeV) and low interest ($E_T < 2.5$ GeV) trigger tower.

If a trigger tower belongs to the high interest class, all crystals of this trigger tower and of its neighbors are read with no zero suppression. If a trigger tower belongs to the medium interest class the crystals of this tower are read with no suppression. If a trigger tower belongs to the low interest class and it is not the neighbor of a high interest tower, only crystals with energy above $3\sigma_{noise}$ are read out, where $\sigma_{noise} \approx 40$ MeV is the RMS of the noise distribution of an ECAL crystal.

The number of read-out crystals in L1 EM candidates depends on selective readout as illustrated in figure B.4. Zero suppression causes a degradation of the energy resolution for low energy photons produced in $\pi^0 \rightarrow \gamma\gamma$ decays, since part of the energy is not collected, as well as a bias in the reconstructed invariant mass $m(\gamma\gamma)$, as shown later. The detailed study on the impact of this effect on the π^0 calibration is one of the possible future improvements on this analysis.

B.4.2 Clustering algorithm

Photons are reconstructed with a simple clustering algorithm. The algorithm starts by searching for cluster seeds in the L1 EM candidate. The seeds are defined as crystals with a measured energy of at least 0.5 GeV. The seeds are then sorted according to their energy. Starting from the seed with highest energy, a 3×3 cluster centered around the seed is formed, excluding the crystals with non-positive energy. Therefore, there can be a minimum of one and a maximum of 9 crystals in a cluster. We require each crystal to belong to only one cluster. Hence, crystals surrounding the seed with energy greater than 0.5 GeV are removed from the list of seeds.

The energy E_{reco} of the cluster is the sum of the energy of its crystals. The position (η_{reco}, ϕ_{reco}) is the energy-weighted average of the position of the crystals [60].
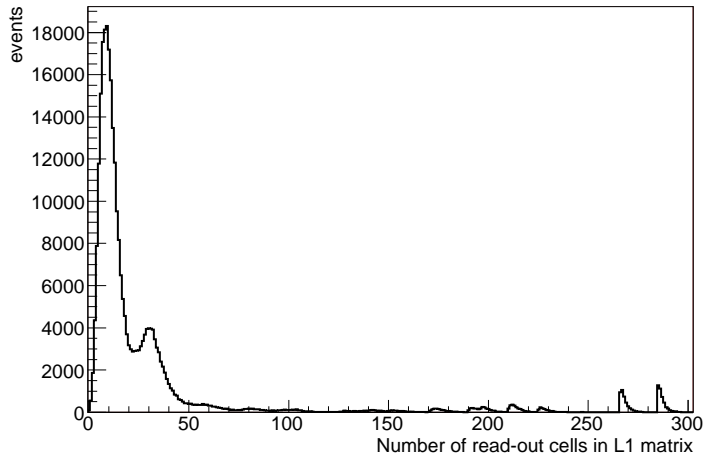
154

Figure B.4: Distribution of the number of crystals read out in L1 EM candidates (sample `jm_03b_qcd_30_50`).

B.4.3 Monte Carlo truth matching

A simple matching algorithm is used to distinguish signal π^0 candidates from combinatorial background, mostly represented by energy deposits of hadrons in the ECAL. Three Monte Carlo (MC) truth variables are used: the energy E_{MC}, the pseudo-rapidity η_{MC}, and the ϕ_{MC} coordinate of the photons from the π^0 decay.

A reconstructed π^0 candidate is identified as signal when both its daughters (photons) satisfy -0.3 GeV $< \Delta E < 0.2$ GeV, $|\Delta\phi| < 0.01$, and $|\Delta\eta| <$ 0.1, with $\Delta\eta = \eta_{MC} - \eta_{reco}$, $\Delta\phi = \phi_{MC} - \phi_{reco}$, and $\Delta E = E_{MC} - E_{reco}$. The energy distributions of signal and background π^0 candidates are shown in figure B.5.

B.4.4 π^0 Selection variables

Some selection variables have been investigated to discriminate between signal and background π^0 candidates. These variables are described in the following and their distributions for signal and background candidates are shown in figures B.6–B.13 for the sample `jm_03b_qcd_30_50`. All distributions are normalized to unity.

- **E1/E9 and E9/E25:**
  E1 is the energy of the seed crystal and E9 (E25) is the sum of energies

155
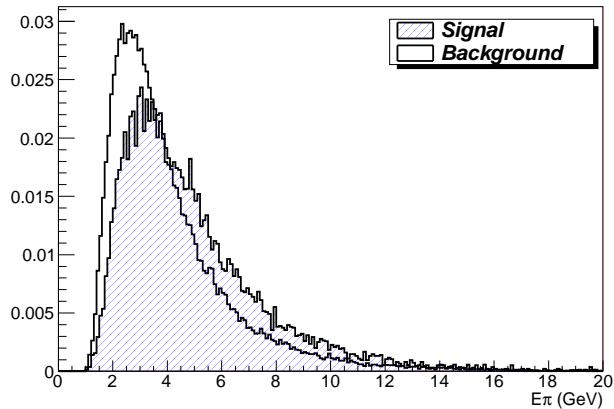
Figure B.5: Energy distribution of signal (filled) and background (empty) π^0 candidates.

of the 3×3 (5×5) matrix of crystals centered around the seed. For a cluster produced by a photon, a large fraction of the energy is deposited in the central crystal since the electromagnetic shower radius is comparable to the crystal size. Tails are due to different sources: for instance the shower can start in the middle of two crystals or two photon showers can overlap in the same cluster. For fake photons the crystals in the cluster have more similar energies and these ratios tend to have a smaller value. Figures B.6 and B.7 show the distributions of these two variables.

- **D12**:
  D12 is the larger between $\Delta\eta$ and $\Delta\phi$, which are the number of crystals separating the seed of each of the two clusters making a π^0 candidate. Figure B.8 shows that clusters coming from $\pi^0 \to \gamma\gamma$ decay are closer than background clusters. This variable is correlated with the energy of the π^0 since the minimum angular separation Θ_{12}^{min} between the two photons can be written as $\Theta_{12}^{min} = 2\arctan\left(m_{\pi^0}/\sqrt{E_{\pi^0}^2 - m_{\pi^0}^2}\right)$, where E_{π^0} (m_{π^0}) is the energy (mass) of the π^0.

- **$N_{cluster}$**: Number of clusters reconstructed in a L1 EM candidate (figure B.9).

- **$(E_{tot} - E_{\pi})/E_{tot}$**:
  E_π is the energy of the π^0 candidate and E_{tot} is the sum of the energy

156

of all reconstructed clusters in a L1 EM candidate. This variable describes the amount of energy deposited in the L1 EM candidate by the clusters not assigned to the π^0. Figure B.10 shows that background π^0 candidates are less isolated than signal ones.

- **$\mathbf{N^{clus}_{xtals}}$:**
  Number of crystals belonging to photon cluster. Clusters can have $N^{clus}_{xtals} < 9$ because of the selective readout (figure B.11). Clusters having only one crystal are discarded.

- **$\mathbf{E^+_{clus}}$:** The energy of the most energetic cluster used to compute $\gamma\gamma$ invariant mass (figure B.12).

- **$\mathbf{E^-_{clus}}$:** The energy of the least energetic cluster used to compute $\gamma\gamma$ invariant mass (figure B.13).

Two sets of requirements, summarized in table B.2, are used to define a `loose` and a `tight` selection. These selection criteria are not optimized at this time.
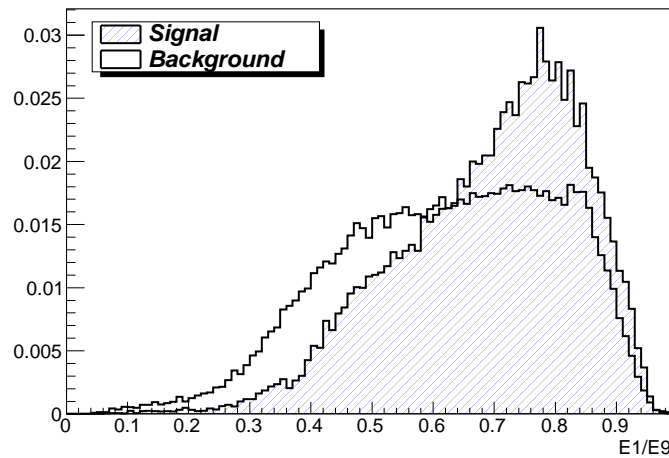
Figure B.6: Distribution of E1/E9.
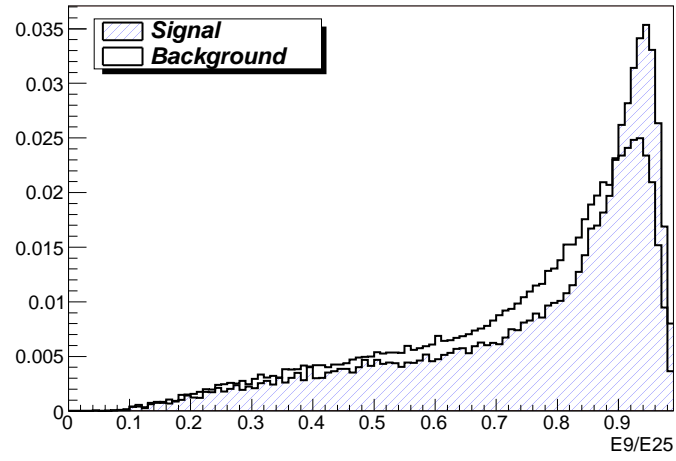
Figure B.7: Distribution of E9/E25.
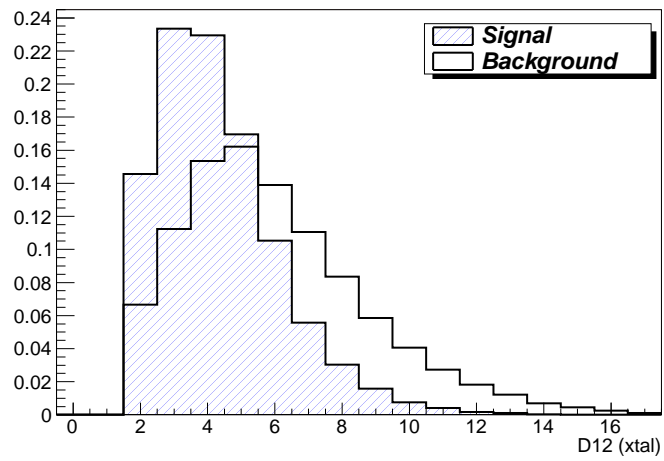
Figure B.8: Distribution of D12.
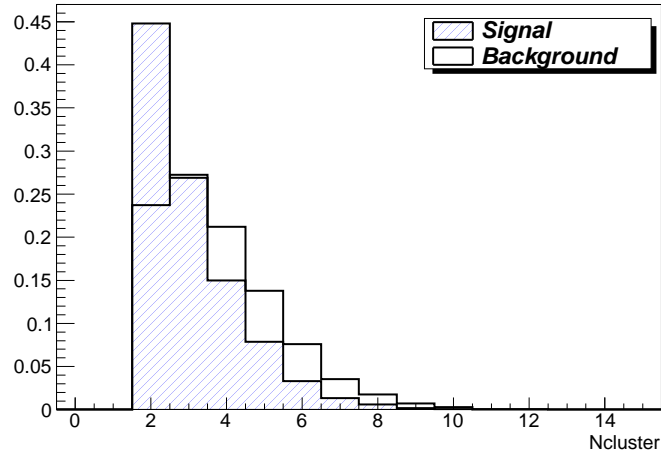
Figure B.9: Distribution of $N_{cluster}$.
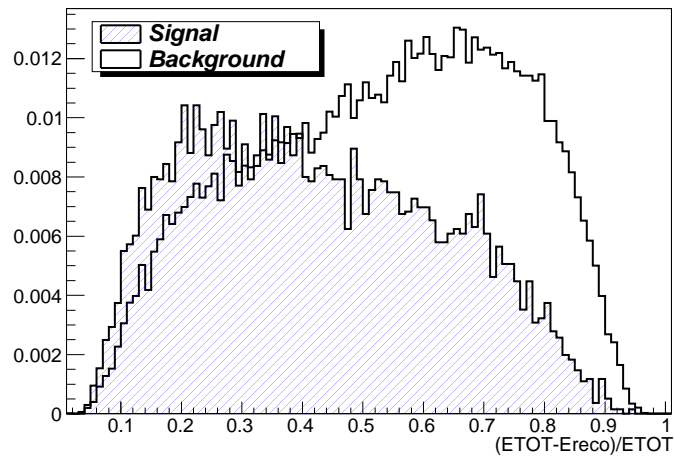
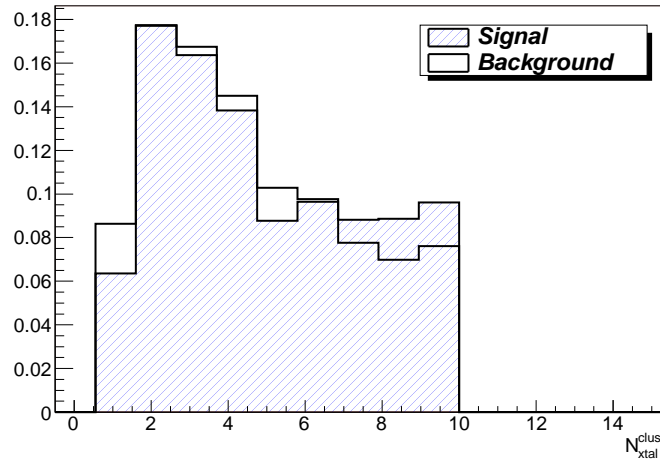Figure B.10: Distribution of $\frac{E_{tot}-E_\pi}{E_{tot}}$.
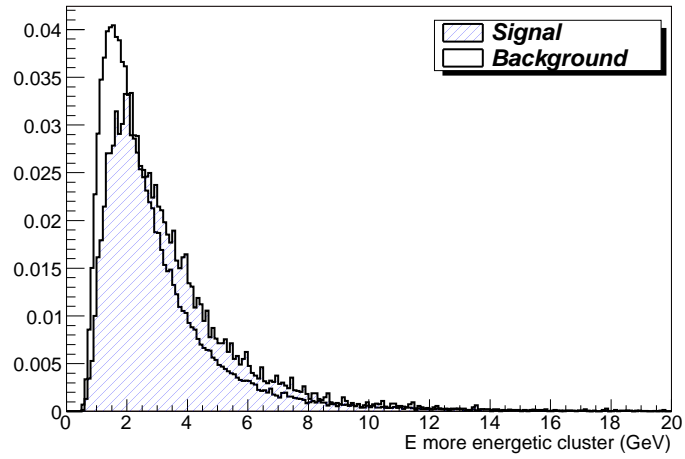
Figure B.11: Distribution of N_{xtals}^{clus}.
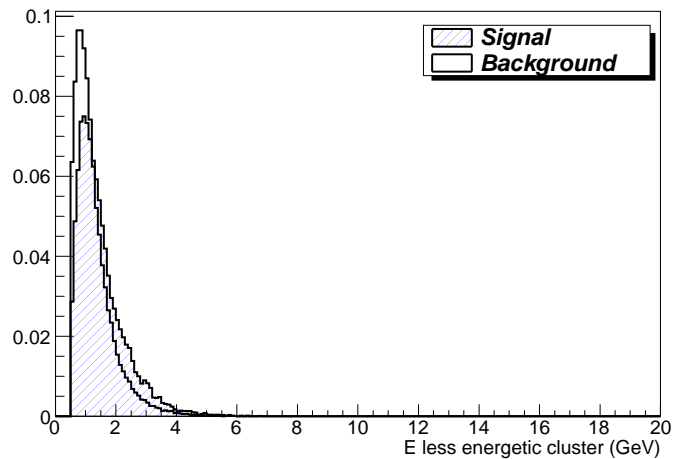

Figure B.12: Distribution of E_{clus}^{+}.

Figure B.13: Distribution of E_{clus}^-.

Table B.2: Definition of `loose` and `tight` selection criteria.

Selection criteria	nocut	loose	tight
E1/E9	-	> 0.6	> 0.75
E9/E25	-	> 0.85	> 0.85
D12 (xtal)	-	-	≤ 5
$N_{cluster}$	-	≤ 3	$= 2$
$(E_{tot} - E_\pi)/E_{tot}$	-	< 0.35	< 0.35
N_{xtals}^{clus}	-	≥ 2	≥ 2
E_{clus}^+ (GeV)	-	-	> 2
E_{clus}^- (GeV)	-	-	> 1

B.4.5 Reconstruction efficiency and signal purity

After the selection, number of signal and background π^0 candidates are determined from fits to the $m(\gamma\gamma)$ invariant mass. Figures B.14, B.15, and B.16 show, respectively, the distribution of $m(\gamma\gamma)$ after the `nocut`, `loose` and `tight` selection criteria, defined at table B.2, for the sample `jm_03b_qcd_30_50`. A Gaussian function is used to fit the signal component, while the background is modeled with a second-order polynomial; the fitted curves are overlaid on each distribution.
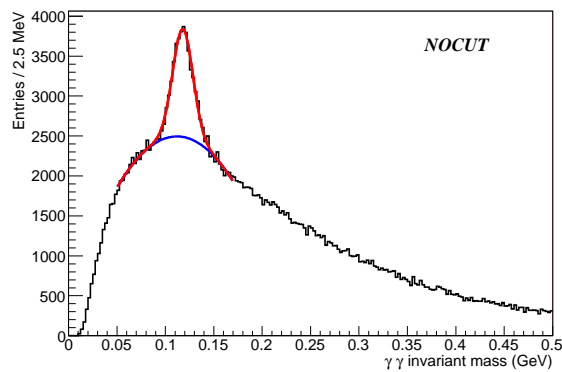
Figure B.14: The $\gamma\gamma$ invariant mass distribution with no selection (`nocut`) applied for the sample `jm_03b_qcd_30_50`.
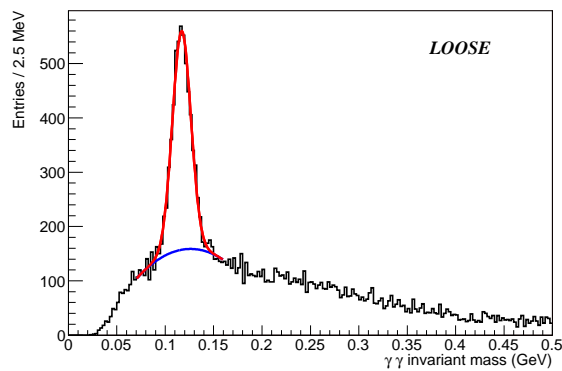

Figure B.15: The $\gamma\gamma$ invariant mass distribution after the `loose` selection for the sample `jm_03b_qcd_30_50`.
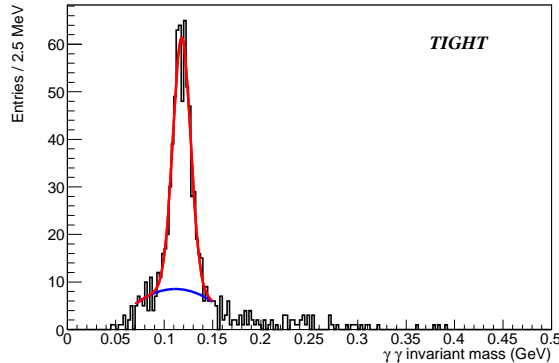
Figure B.16: The $\gamma\gamma$ invariant mass distribution after the `tight` selection for the sample `jm_03b_qcd_30_50`.

Number of signal and background candidates are computed by integrating the corresponding fit components in the interval 85 MeV $< m(\gamma\gamma) <$ 145 MeV, and are reported in table B.4.5 for each sample, including the fit results.

The fitted mean m_π of the signal Gaussian is about 20 MeV lower than the nominal π^0 mass. This is caused by the selective readout, as anticipated in section B.4.1.

The signal efficiency ϵ_{reco} is defined as the ratio of the fitted number of selected signal π^0 candidates, and the number of generated π^0s, which have both photons with an energy at generator level of $E_{MC}^{\gamma_{1,2}} > 0.5$ GeV, and falling within the L1 EM candidate selected for reconstruction.

These efficiencies, reported in table B.4.5 for each sample, include the effect of photon conversion in the tracker material. This is verified by removing all requirements on the selection variables (category `nocut` in table B.4.5). The low efficiency in this case is almost entirely due to the photons converted before reaching the ECAL, as discussed in the next section.

The average number of reconstructed π^0 candidates per event and the average signal purity are computed from the values for individual samples weighted with their effective cross section σ_{eff}, and are summarized in table B.4.5 for the three different selection criteria.

nocut						
Dataset	σ_{eff} (10^{-4} mb)	ϵ_{reco} (%)	$N_{\pi^0}^{reco}$	S/B	σ_π/m_π (%)	m_π (MeV)
jm_03b_qcd_15_20	7.7±1.6	34.5±0.5	0.11	0.47	9.0±0.4	116.2±0.3
jm_03b_qcd_20_30	9.26±0.78	33.4±0.3	0.14	0.39	8.8±0.3	116.8±0.2
jm_03b_qcd_30_50	14.7±0.5	29.5±0.2	0.17	0.26	9.2±0.2	118.1±0.2
jm_03b_qcd_50_80	9.52±0.10	25.0±0.1	0.19	0.15	9.8±0.4	120.0±0.2
jm_03b_qcd_80_120	3.82±0.02	21.0±0.1	0.23	0.10	10.2±0.5	121.7±0.2
jm_03b_qcd_120_170	1.85±0.06	17.6±0.1	0.25	0.08	9.9±0.8	121.9±0.4
loose						
jm_03b_qcd_15_20	7.7±1.6	11.7±0.3	0.038	1.04	7.9±0.4	116.9±0.4
jm_03b_qcd_20_30	9.26±0.78	9.1±0.2	0.039	0.96	7.7±0.3	117.2±0.2
jm_03b_qcd_30_50	14.7±0.5	6.1±0.1	0.042	1.06	8.1±0.3	117.0±0.2
jm_03b_qcd_50_80	9.52±0.10	3.56±0.05	0.039	0.9	7.8±0.2	117.6±0.2
jm_03b_qcd_80_120	3.82±0.02	2.40±0.03	0.038	0.96	8.0±0.2	117.6±0.2
jm_03b_qcd_120_170	1.85±0.06	1.80±0.03	0.035	0.85	7.4±0.3	117.5±0.2
tight						
jm_03b_qcd_15_20	7.7±1.6	1.3±0.1	0.0044	2.3	7.4±0.6	118.2±0.8
jm_03b_qcd_20_30	9.26±0.78	1.13±0.06	0.0056	3.2	8.3±0.6	119.4±0.6
jm_03b_qcd_30_50	14.7±0.5	0.82±0.04	0.0051	2.6	7.8±0.6	118.2±0.5
jm_03b_qcd_50_80	9.52±0.10	0.45±0.02	0.0050	2.3	7.5±0.4	118.5±0.4
jm_03b_qcd_80_120	3.82±0.02	0.30±0.01	0.0049	2.3	7.1±0.3	118.8±0.3
jm_03b_qcd_120_170	1.85±0.06	0.25±0.01	0.0055	3.0	7.3±0.4	118.7±0.4

Table B.3: Effective cross section σ_{eff}, reconstruction efficiency ϵ_{reco}, number of reconstructed signal π^0 per event $N_{\pi^0}^{reco}$, signal to background ratio S/B, and mean m_π and width σ_π of the fitted signal Gaussian. Unless specified, all values have a relative uncertainty of 2% or less.

Selection criteria	$\langle N_{\pi^0}^{reco} \rangle$	$\langle S \rangle / \langle B \rangle$
nocut	$16.5 \pm 0.8 \ 10^{-2}$	0.19 ± 0.012
loose	$4.0 \pm 0.2 \ 10^{-2}$	1.00 ± 0.07
tight	$5.1 \pm 0.3 \ 10^{-3}$	2.55 ± 0.20

Table B.4: Average number of signal reconstructed π^0 per event $\langle N_{\pi^0}^{reco} \rangle$ and the ratio between the average signal $\langle S \rangle$ and background $\langle B \rangle$ yields, computed by weighting with the relative cross section of each sample.

B.4.6 Reconstruction efficiency vs. η

The π^0 reconstruction efficiency decreases with increasing η as shown in figure B.17. This is due to photon conversion in the material between the interaction point and the ECAL. Conversion probability P_{conv} for high energy photons with energy $E_\gamma >> $ MeV passing through a material with radiation length X_0 is given by

$$P_{conv} \approx 1 - e^{\left(-\frac{7}{9} \cdot \frac{X}{X_0}\right)}. \tag{B.1}$$

This probability is higher toward the end of the barrel due to the larger amount of material in front the ECAL in that region (figure B.18).

The distribution of the $\gamma\gamma$ invariant mass, with results of a fit overlaid, in each of the 4 modules of a super module of the ECAL are shown in figures B.19 and B.20.

Number of reconstructed π^0 (figure B.21) and the signal to noise ratio S/B (figure B.22), reported in table B.4.6, both decrease for increasing η, while the number of background candidates shows no particular behavior versus η (figure B.21).

Module	η range	ϵ_{reco} (%)	$N_{\pi^0}^{reco}$	S/B	σ_π/m_π (%)	m_π (MeV)
1	$0 < |\eta| < 0.435$	7.8±0.3	(1.47±0.04) 10^{-2}	1.60±0.07	8.2±0.6	116.6±0.4
2	$0.435 < |\eta| < 0.783$	6.8 ± 0.3	(1.11±0.03) 10^{-2}	1.27±0.06	8.3±0.6	116.2±0.5
3	$0.783 < |\eta| < 1.131$	5.5 ± 0.3	(0.95±0.03) 10^{-2}	0.81±0.04	7.9±0.6	118.6±0.5
4	$1.131 < |\eta| < 1.479$	4.5 ± 0.3	(0.62±0.03) 10^{-2}	0.57±0.03	7.5±0.7	116.5±0.7

Table B.5: Summary results for η dependence of π^0 reconstruction for the sample `jm_03b_qcd_30_50`. The `loose` selection criteria is applied (see table B.2).
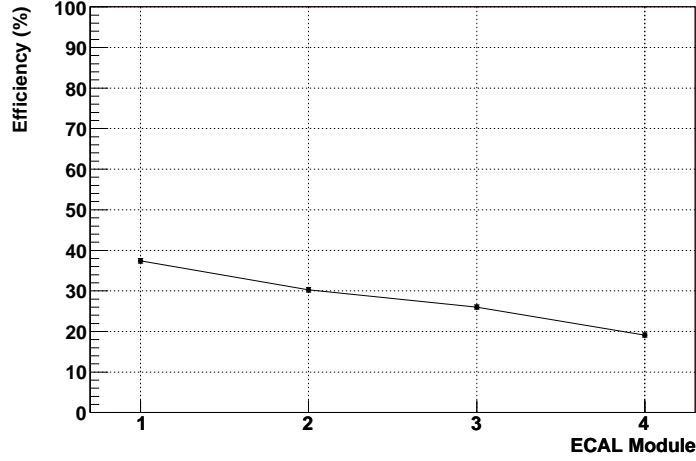
Figure B.17: Reconstruction efficiency ϵ_{reco} for different ECAL modules for the sample jm_03b_qcd_30_50. ϵ_{reco} includes the conversion probability. No selection criteria is applied (see nocut column of table B.2).
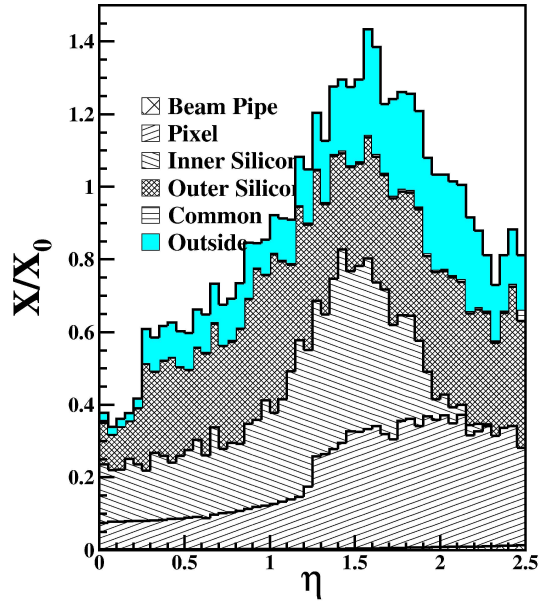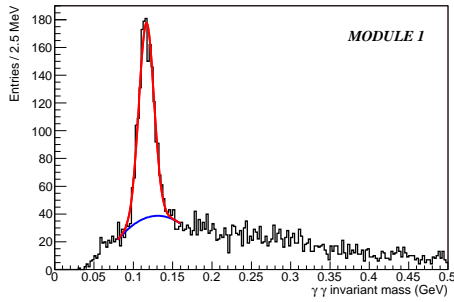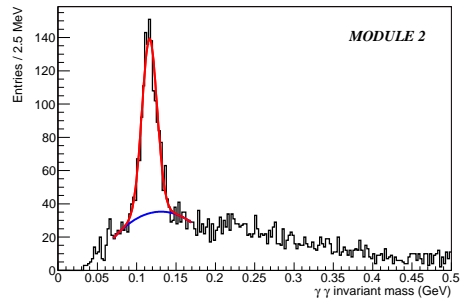

Figure B.18: Amount of material (in radiation length X_0) in front of the ECAL, including that for tracker material, the beam pipe, the support structure and the cables, as a function of pseudo-rapidity [30]
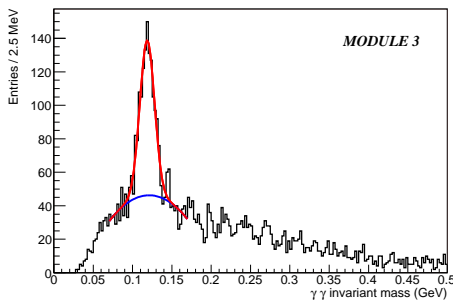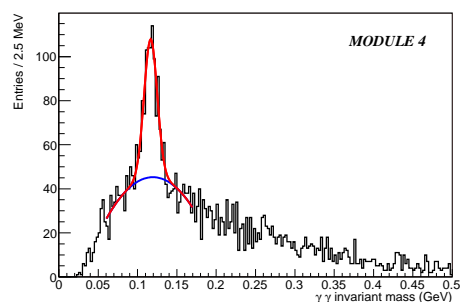
166

Figure B.19: The $\gamma\gamma$ invariant mass distribution for π^0 candidates falling in the module 1 (a) and in the module 2 (b) of the ECAL, after the `loose` selection criteria, for the sample `jm_03b_qcd_30_50`.

Figure B.20: The $\gamma\gamma$ invariant mass distribution for π^0 candidates falling in the module 3 (a) and in the module 4 (b) of the ECAL, after the `loose` selection criteria, for the sample `jm_03b_qcd_30_50`.
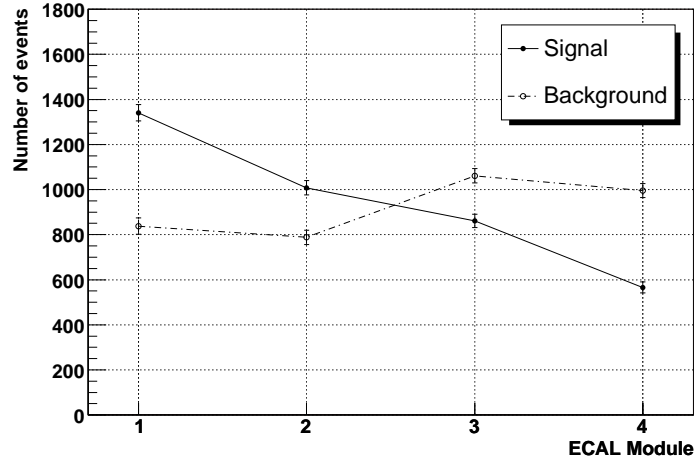
Figure B.21: Number of $\gamma\gamma$ signal (solid) and background (dashed) events in different ECAL modules for the sample jm_03b_qcd_30_50. The loose selection criteria is applied (see table B.2).
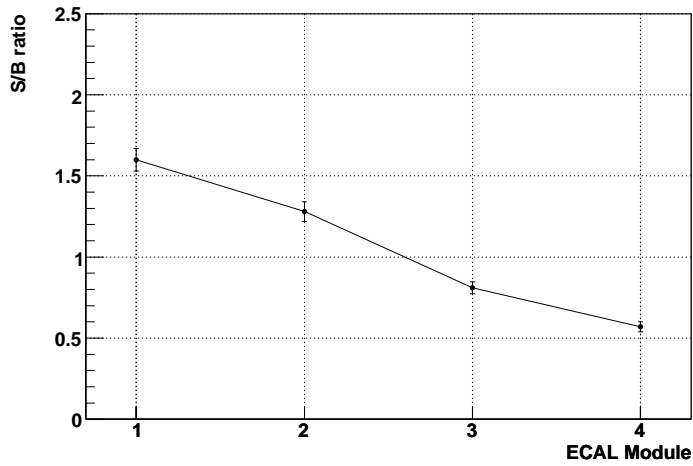

Figure B.22: Signal over background ratio S/B in different ECAL modules for the sample jm_03b_qcd_30_50. The loose selection criteria is applied (see table B.2).

B.4.7 Effect of L1 accept on reconstruction efficiency

Due to the limited number of events in the samples at low $\hat{P}_T$ and the small L1 trigger efficiency for these samples, very few events are available to study π^0 reconstruction. Therefore all simulated events are used, including those discarded by the L1 trigger, in computing the reconstruction efficiencies discussed in the previous section.

It has been verified, however, that distributions of selection variables are similar for events selected and discarded by the L1 trigger, and hence the estimated reconstruction efficiencies and signal purities are not affected by ignoring the L1 decision.

Figure B.23 shows the distribution of E_T for the L1 EM candidates in the sample `jm_03b_qcd_30_50`, which has a L1 trigger efficiency of about 1%. At low E_T where the π^0 candidates are reconstructed, the distributions with and without the L1 decision are very similar. Figures B.24 and B.25 show similar comparison for the distribution of $E_{tot} - E_\pi/E_{tot}$ for signal and background candidates, respectively.

Finally, the distribution of the $\gamma\gamma$ invariant mass is compared between the selected and discarded events, and again no significant difference between the two samples is observed.

It can be concluded that the reconstruction efficiency measured with all simulated events is a valid estimate of its value for the subset of events selected by the L1 trigger.
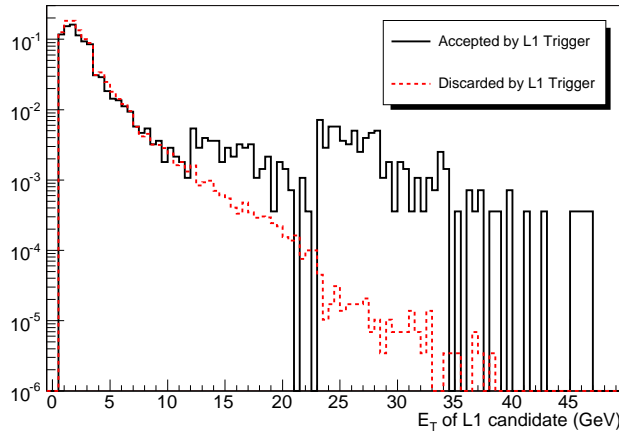

Figure B.23: Distribution of transverse energy of L1 electromagnetic candidate for events accepted (solid) or discarded (dashed) by the L1 trigger, for the sample `jm_03b_qcd_30_50`. Distributions are normalized to unity.
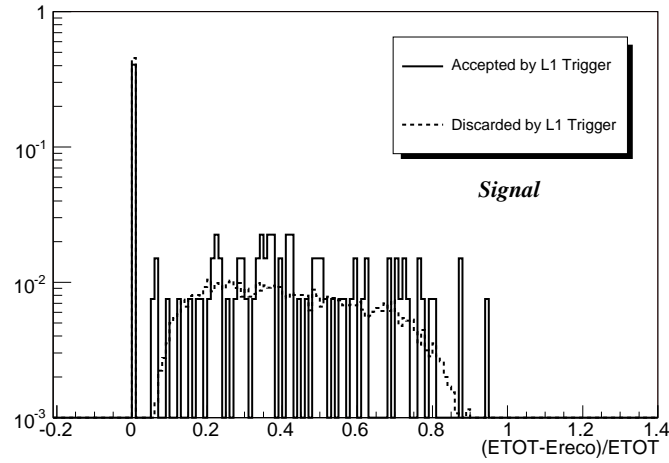
Figure B.24: The $\frac{E_{tot}-E_\pi}{E_{tot}}$ distribution of signal π^0 candidates in events accepted (solid) or discarded (dashed) by the L1 trigger, for the sample jm_03b_qcd_50_80.
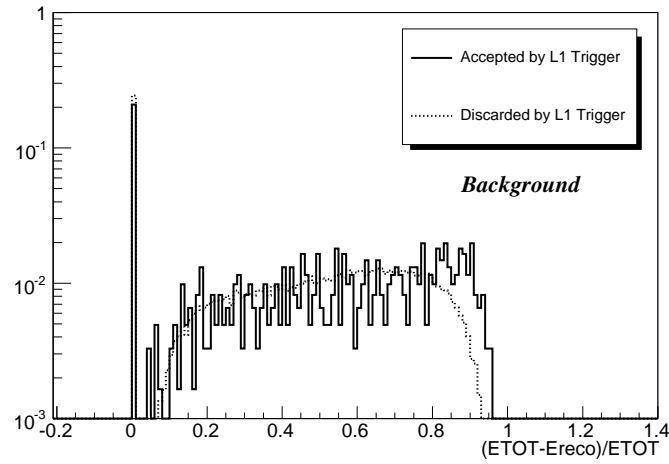

Figure B.25: The $\frac{E_{tot}-E_\pi}{E_{tot}}$ distribution of background π^0 candidates in events accepted (solid) or discarded (dashed) by the L1 trigger, for the sample jm_03b_qcd_50_80.
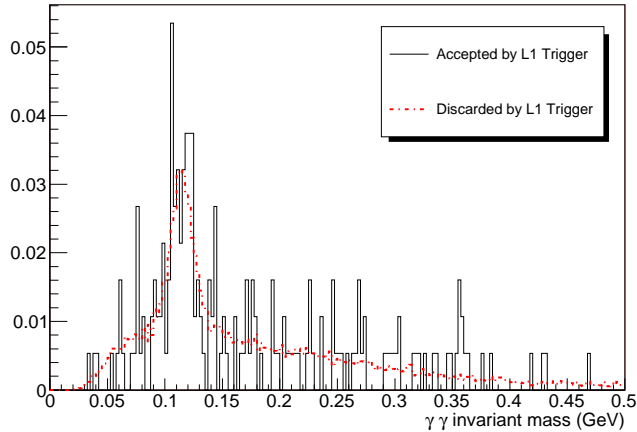
Figure B.26: The $\gamma\gamma$ invariant mass distribution for π^0 candidates in events accepted (solid) or discarded by (dashed) the L1 trigger, for the sample `jm_03b_qcd_50_80`. Distributions are normalized to unity.

B.5   Intercalibration with π^0candidates

This section describes the calibration algorithm using the $\pi^0 \rightarrow \gamma\gamma$ candidates which have been reconstructed with the method described in the previous section. To test the algorithm with large statistics, a sample of 2 millions of QCD jet events with high $\hat{P}_T$ (`eg03_jets_2g_pt50170`) is used. The dependence of the calibration precision on the number of reconstructed π^0 per crystal and on the background contamination are studied.

B.5.1   Iterative calibration algorithm

The calibration method used in this analysis is similar to that implemented for the $Z \rightarrow e^+e^-$ calibration at the reference [42]. It is based on the relation among the true mass value of decaying particle, the reconstructed mass value and the calibration coefficients of calorimeter crystals.

The energy measured in the crystal j for the candidate i ($E^i_{j_{meas}}$) is related to the energy which would have been measured in that crystal without any mis-calibration ($E^i_{j_{true}}$) by the equation $E^i_{j_{meas}} = (1 + \varepsilon_j) \cdot E^i_{j_{true}}$, where ε_j is the mis-calibration factor. The calibration coefficient of the crystal j is defined as $c_j = (1 + \varepsilon_j)^{-1}$.

171

The photon energy is the sum of the energies of the crystals of the 3×3 cluster associated to it:

$$E^i{}_{meas} = \sum_{j\epsilon\gamma} E^i_{j\,meas} = E^i_{true} \cdot \left(1 + \sum_{j\epsilon\gamma} \varepsilon_j w^i_j\right) \tag{B.2}$$

where the weight $w^i_j = E^i_{j\,true}/E^i_{true}$ is the fraction of energy deposited in the crystal j with respect to the photon energy without any mis-calibration. The reconstructed $\gamma\gamma$ invariant mass can be written as:

$$\mathrm{M}^i_{inv} = \sqrt{2 \cdot E^i_{\gamma_1} \cdot E^i_{\gamma_2} \cdot (1 - \cos \Theta^i_{12})} \simeq \mathrm{M}_{\pi^0} \cdot \sqrt{\left(1 + \sum_{j\epsilon\gamma_1,\gamma_2} \varepsilon_j w^i_j\right)} \tag{B.3}$$

where Θ^i_{12} is the angle between the two photons, which is estimated using the energy weighted average position of the clusters. The terms $\mathcal{O}(\varepsilon^2)$ are neglected. The sum runs over all the crystals of the two clusters. By inverting equation B.3, the following relation is found for each π^0 candidate:

$$\left(\frac{\mathrm{M}^i_{inv}}{\mathrm{M}_{\pi^0}}\right)^2 - 1 = \sum_{j\epsilon\gamma_1,\gamma_2} \varepsilon_j w^i_j \tag{B.4}$$

The unknown values of ϵ_j can be obtained by solving the linear system, where the number of equations corresponds to the number of candidates. The inversion of such equation matrix is difficult because this matrix is far to be diagonal. Furthermore, the weight matrix w^i_j is not known and can be only approximated by using the measured energy deposits. These issues can be solved using an iterative method.

This method uses the ratio $\mathrm{M}_{inv}/\mathrm{M}_{\pi^0}$ that is calculated for each candidate. The effect of the mis-calibration of the crystals is folded into the factor $\langle\varepsilon\rangle^i$ which is defined as $\langle\varepsilon\rangle^i = \sum_j \varepsilon_j w^i_j / \sum_j w^i_j$. It corresponds to the weighted average of the mis-calibration factors for the candidate i, using the fraction of the energy deposited in each crystal. Taking into account that there are two photons we get:

$$\langle\varepsilon\rangle^i = \frac{1}{2} \cdot \left[\left(\frac{\mathrm{M}^i_{inv}}{\mathrm{M}_{\pi^0}}\right)^2 - 1\right] \tag{B.5}$$

Each single mis-calibration factor ε_j is then obtained as the average over all candidates of the $\langle\varepsilon\rangle^i$ coefficients, weighted by w^i_j:

$$\varepsilon_j \simeq \frac{\sum_i \langle\varepsilon\rangle^i w^i_j}{\sum_i w^i_j} \tag{B.6}$$

Since this relation is approximated, the procedure is iterated until the calibration coefficients converge. After n iterations the calibration coefficient of crystal j is the product:

$$\mathcal{C}_j = \prod_{iteration\ k=1}^{n} c_j^k = \prod_{iteration\ k=1}^{n} \frac{1}{1+\varepsilon_j^k} \qquad (B.7)$$

B.5.2   Calibration procedure

Each iteration of the calibration procedure consists of:

1. **Reconstruction**: $\pi^0 \rightarrow \gamma\gamma$ candidates are reconstructed and selected using the criteria detailed in section B.4;

2. **Invariant mass window**: reconstructed π^0s which lie under the invariant mass peak are selected. This is done to reduce the impact of the tails of the invariant mass distribution and of the background on the calibration. The invariant mass window is set to [-35 MeV,+35 MeV] around π^0 peak position calculated in the previous iteration. The optimization this range is one of the possible improvements on this calibration.

3. **Running the algorithm iteration**: calibration coefficients are calculated using the selected π^0 candidates;

4. **Update**: the calibration coefficients are updated and the reconstruction (including the clustering) is redone. Then, a new iteration starts.

As anticipated, large datasets are required to determine the calibration coefficients with small uncertainties ($\mathcal{O}(1\%)$) on the whole barrel. Due to the limited Monte Carlo statistics, the performance of the algorithm is tested by folding the barrel in a small matrix of 21×21 crystals. After this folding, the π^0 calibration procedure is applied on this matrix only. This folding increases the available statistics but introduces additional systematic effects.

In the following the quantity

$$S \approx \frac{1}{2} \cdot \sum_{candidate\ i} w_j^i.$$

is used, which represents the integral contribution of that crystal (j) in the $\pi^0 \rightarrow \gamma\gamma$ reconstruction. This quantity is used to determine the dependence of the calibration precision on the statistics.

Figure B.27 shows the value of $\sum_i w_j^i$ for the crystals in the 21x21 folded matrix. The lower value of $\sum_i w_j^i$ at the borders depends on the fact that one

of the two photons produced by the π^0 decay falls outside the matrix. We exclude these crystals to reduce possible low statistics effects by considering only a 11×11 crystals region in the middle of the matrix. The crystals excluded by this cut are kept perfectly calibrated at each iteration of the procedure.
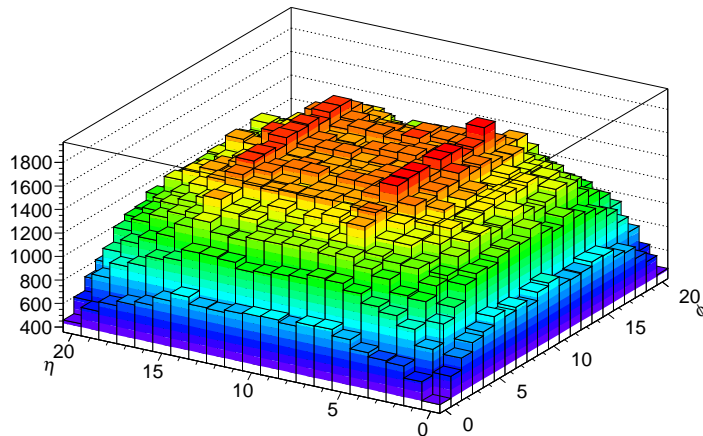

Figure B.27: Distribution of $\sum_i w_j^i$ for crystals contained in the folded 21x21 matrix

B.5.3 π^0 Calibration with signal events

The calibration procedure is performed with the largest possible π^0 sample, to test the algorithm with large statistics. For this reason, the $\pi^0 \rightarrow \gamma\gamma$ candidates are selected by only requiring $(E_{tot} - E_\pi)/E_{tot} < 0.35$ (see section B.4.4). Signal and background π^0 candidates are identified with the Monte Carlo matching described in section B.4.3. Figure B.28 shows the π^0 invariant mass distribution for selected signal candidates.

An initial crystals mis-calibration is simulated using a Gaussian smearing of $\sigma = 5\%$. The calibration precision after each iteration is reported in Figure B.29. It is defined as the standard deviation of the distribution of the calibration coefficients (σ_c) divided by its average (c). Average and standard deviation are obtained by fitting the distribution with a Gaussian distribution (see Figure B.30).

It has to be noted that the mean of the distribution differs from 1 (≈ 1.1). This is due to the shift between the true and the reconstructed π^0 mass
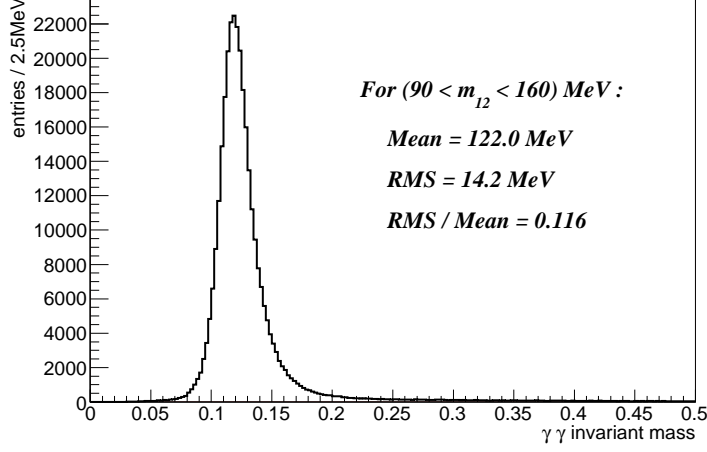
174

Figure B.28: Invariant π^0 mass distribution for signal π^0 candidates with $(E_{tot} - E_\pi)/E_{tot} < 0.35$ for the sample `eg03_jets_2g_pt50170`.

induced by the selective read-out.

The calibration precision obtained, in absence of background, with a statistics of $S = 800$, is $\sigma_c/c \approx 1.2\%$.

Figure B.31 shows the calibration precision σ_c/c as a function of S. The calibration precision can be parametrized as

$$\frac{\sigma_c}{c} = \frac{\sigma_{stat}}{\sqrt{S}} \oplus \sigma_{sys} \tag{B.8}$$

where $\sigma_{stat}/\sqrt{S}$ are σ_{syst} are the statistical and the systematic term, respectively. The curve fitted using this parametrization is overlaid to the data in Figure B.31. The fit results are $\sigma_{stat} = (22.8 \pm 3.0)\%$ and $\sigma_{sys} = (0.93 \pm 0.14)\%$.

Points with different statistics are correlated, since a single set of events is divided to create subsamples of different size. This correlation is not taken into account when extracting the uncertainty on the fit parameters.

The statistical term σ_{stat} is consistent with the expectations. A naive parametrization of σ_{stat} can be obtained by assuming equal energy for both photons as

$$\tilde{\sigma}_{stat} = \frac{\sqrt{2} \cdot \frac{\sigma_\pi}{m_\pi}}{\sqrt{\langle \sum_k^{cluster} w_k^2 \rangle}} \tag{B.9}$$
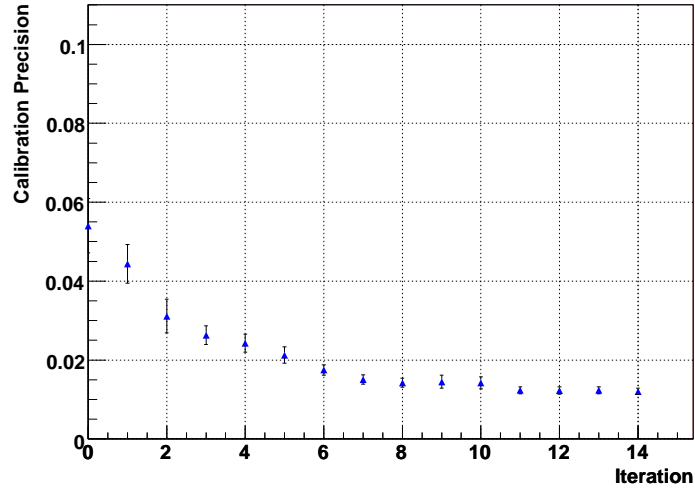
where:

Figure B.29: The calibration precision σ_c/c as a function of the number of the iterations.
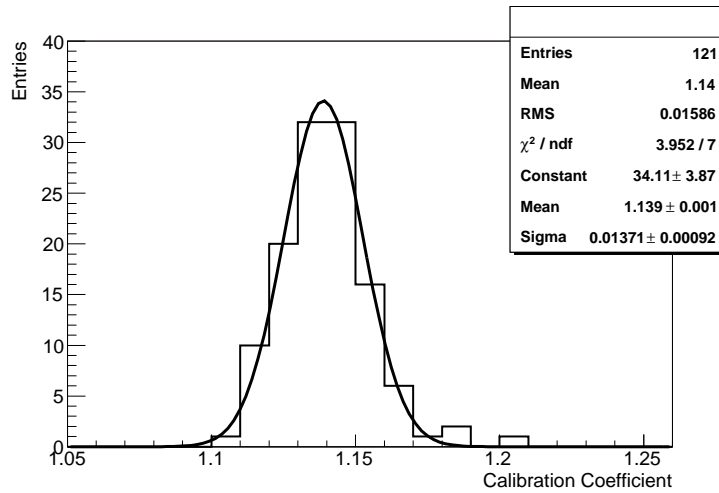

Figure B.30: Distribution of calibration coefficients in 11x11 fiducial region after 14 iterations. The values $\mu = (1.139 \pm 0.001)$ and $\sigma = (1.37 \pm 0.09)10^{-2}$ are obtained from the Gaussian fit.

- $w_k = E_k/E_{clus}$ is the fraction of the cluster energy deposited in the crystal k. The sum over k is performed over the crystals of the cluster. Figure B.32 shows the distribution of $\sum_k^{cluster} w_k^2$.

- σ_π and m_π are, respectively, the width and mean value of the π^0 invariant mass distribution (figure B.28).

The obtained value $\tilde{\sigma}_{stat} \approx 21\%$ is consistent with the fit result.

Finally, a systematic uncertainty of $\sim 1\%$ is observed. This can be due to the folding of different η regions of the barrel in the 21×21 matrix. In addition, the selective readout introduces important biases. Thus, further studies and larger Monte Carlo statistics are required to understand and reduce the systematics of the method.
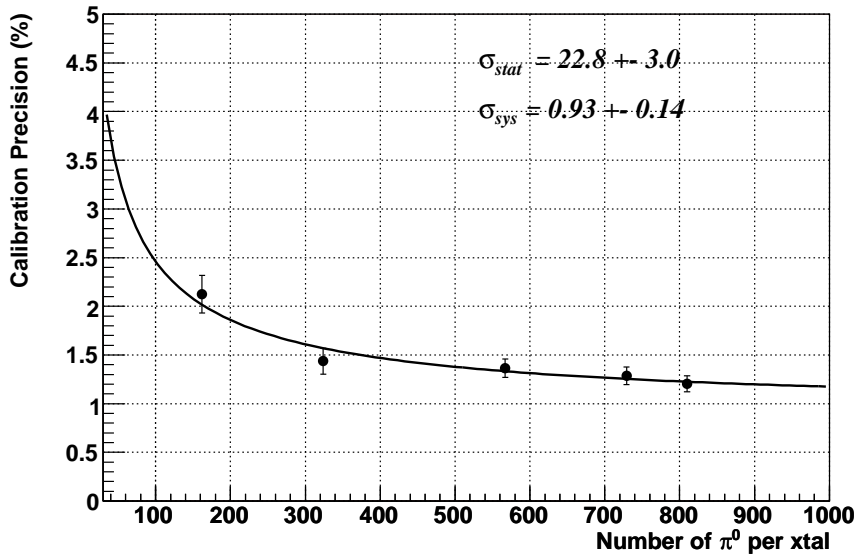

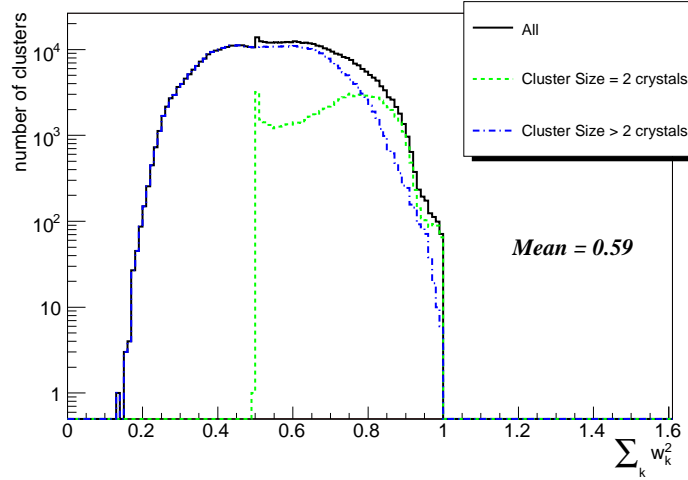
Figure B.31: Calibration precision as a function of the S.

177

Figure B.32: Distribution of $\sum_k^{cluster} w_k^2$. The contributions from clusters made by 2 and > 2 crystals are also shown.

B.5.4 Background impact on calibration

In order to check the impact of the background contamination on the calibration precision, an arbitrary amount of reconstructed background candidates are added to the signal sample. The calibration procedure is the same as in the signal only case discussed before.

Figure B.33 shows how the calibration precision depends on the signal over background ratio. If the background does not introduce either biases or additional systematic effects, the calibration precision can be described by

$$\frac{\sigma_c}{c} = \sigma_{stat} \cdot \frac{\sqrt{S+B}}{S} \oplus \sigma_{sys} \tag{B.10}$$

where S and B are the number of π^0 reconstructed per crystal for signal and background candidates, respectively. Using this variable, different calibration precision results, obtained with and without background contamination, are merged in the same plot, as shown in figure B.34. The overlaid curve corresponds to the parametrization of equation B.10 and uses the parameters σ_{stat} and σ_{sys} obtained in the previous section with no background. The points at small $\sqrt{S+B}/S$ follow the curve, while some deviation is observed at larger $\sqrt{S+B}/S$.

It can be concluded that the background does not introduce large effects but more statistics is needed to perform detailed studies, in particular for large background contaminations.
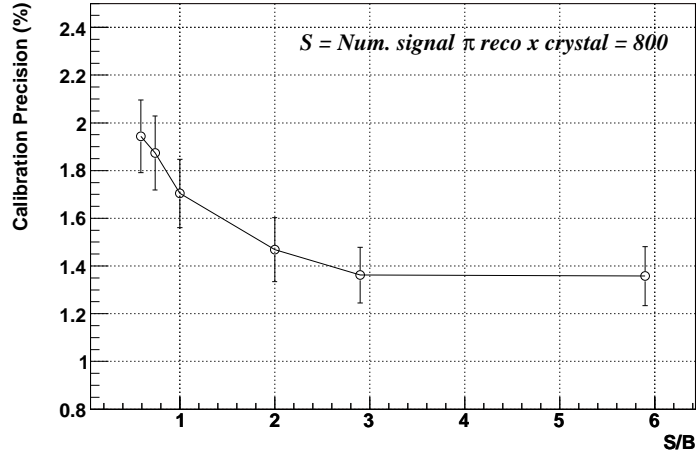
178

Figure B.33: Calibration precision as a function of background contamination. Number of signal candidates per crystal is $S \approx 800$.
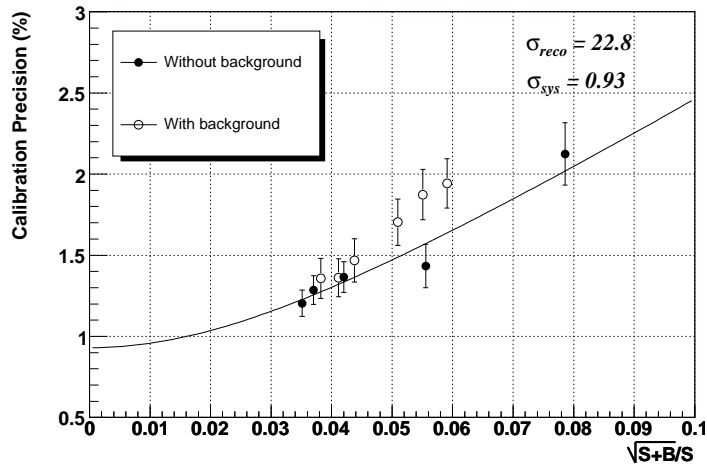

Figure B.34: Calibration precision as a function of number of $\sqrt{S+B}/S$. The curve is obtained from equation B.10 using σ_{stat} and σ_{sys} extracted from fit without background contamination (see paragraph B.5.3)

179

B.6 Estimate of time required for ECAL calibration

All information obtained in the previous sections can be combined to give an estimate of the time required to calibrate the whole ECAL detector with a given precision.

The dependence of calibration precision from signal and background statistics is given by the equation B.10, here reported

$$\frac{\sigma_c}{c} = \sigma_{stat} \cdot \frac{\sqrt{S+B}}{S} \oplus \sigma_{sys} \quad . \tag{B.11}$$

The value of S can be calculated by the following relation, valid for signal $\pi^0 \to \gamma\gamma$ candidates,

$$N_{\pi^0}^{reco}(\eta) \cdot \mathcal{R}_{L_1} \cdot T_{calib} = S \cdot \mathrm{N}_{xtals}^{\eta} \tag{B.12}$$

where $N_{\pi^0}^{reco}(\eta)$ is the number of signal π^0 candidates reconstructed per event in a given η region of ECAL, $\mathcal{R}_{L_1}$ is the L1 trigger rate, T_{calib} is the time of data taking, S is the number of π^0 candidates reconstructed per crystal and $\mathrm{N}_{xtals}^{\eta}$ is the number of crystals in a given η region of ECAL.

The levels of signal and background and the reconstruction efficiency, calculated in the section B.4 for the sample `jm_03b_qcd_30_50`, are used.

The selection criteria `nocut` and `loose` (see table B.2) give very similar values of $\sqrt{S+B}/S$. Furthermore the amount of data to be stored when no selection criteria is applied is $\mathcal{O}(10)$ larger than in case of loose selection. For this reasons the following estimations is given using the `loose` selection.

Following a conservative approach, a L1 trigger rate equal to 10 kHz is assumed for QCD jet events, as discussed in section B.3 (see table B.3).

It has been noticed that reconstruction efficiency decreases at increasing η (see paragraph B.4.6). Thus, the estimate of calibration precision as a function of time is given for different η regions.

Figure B.35 shows that all crystals of ECAL calorimeter could be calibrated at $\approx 1\%$ in about 100 hours of real data taking. Due to the lower reconstruction efficiency, more time is needed to calibrate, at a given precision, ECAL modules at higher η.
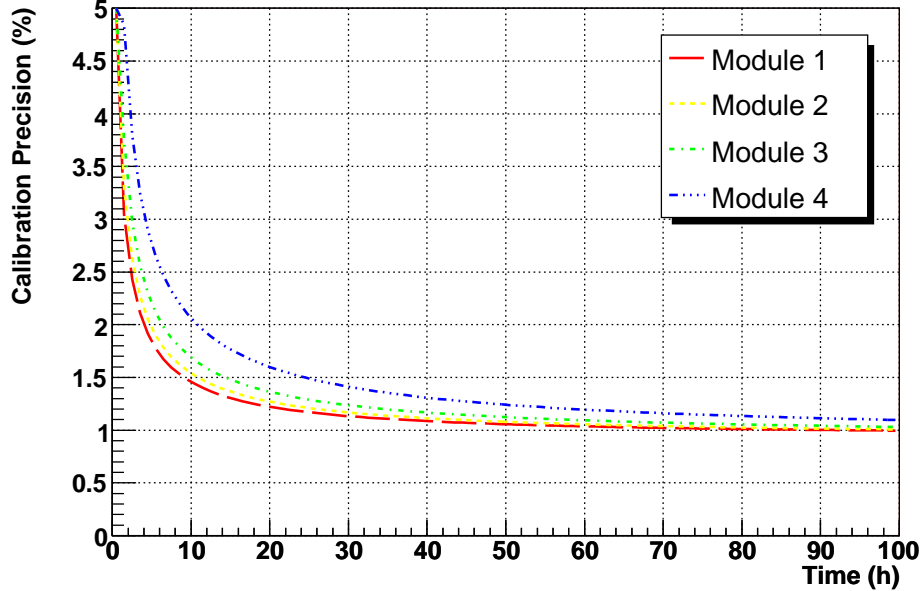
Figure B.35: Calibration precision as a function of data taking time.

B.7 Estimate of data rate in the High Level Trigger

In the previous section, the inter-calibration of the barrel is shown to be possible with a few days of data taking, using the π^0 candidates selected with the `loose` criteria. An important issue to understand the real feasibility of this calibration during data taking, is to estimate the rate of data to be stored in the HLT.

For this study, the L1 trigger rate is assumed to be dominated by QCD jet events. We use the simulated QCD jet sample `jm_03b_qcd_30_50` and apply the `loose` selection criteria described in section B.4.4.

In addition, the maximum number N_{max} of read out cells in a L1 EM candidate is required to be 100. It is verified that this requirement does not modify the reconstruction efficiency nor the signal purity.

The rate is given by

$$\text{rate} = \mathcal{R}_{L_1} \times N_{L_1}^{\pi^0} \times N_{L_1}^{xtal} \times S_{RecHit} \times f_{mass} \qquad \text{(B.13)}$$

where

- the L1 trigger rate is assumed to be $\mathcal{R}_{L_1} = 10$ kHz;

- $N_{L_1}^{\pi^0} \approx 0.2$ is the average number of L1 EM candidates containing at least one reconstructed π^0; the distribution of $N_{L_1}^{\pi^0}$ is shown in figure B.36;

- $N_{L_1}^{xtal} \approx 20$ is the average number crystals read out in a 20×20 L1 EM candidate which contains at least one reconstructed π^0. Figure B.37 shows the distribution of $N_{L_1}^{xtal}$;

- $S_{RecHit} = 12$ bytes is the size of a reconstructed RecHit (`EcalRecHit`) in ORCA, which includes energy, time and χ^2;

- $f_{mass} \approx 0.5$ is the fraction of events with at least one π^0 having an invariant mass in the range $70 < m(\gamma\gamma) < 160$ MeV; this mass region is 20% wider than the region used in the calibration.

The estimated rate is 250 kB/sec of data that must be stored to perform the calibration procedure described in this note. This rate is well within the constraints of the dedicated calibration/alignment stream. It is expected that this rate could be further reduced after optimization of the selection criteria, and by moving additional requirements, currently applied during the calibration procedure, into the HLT.
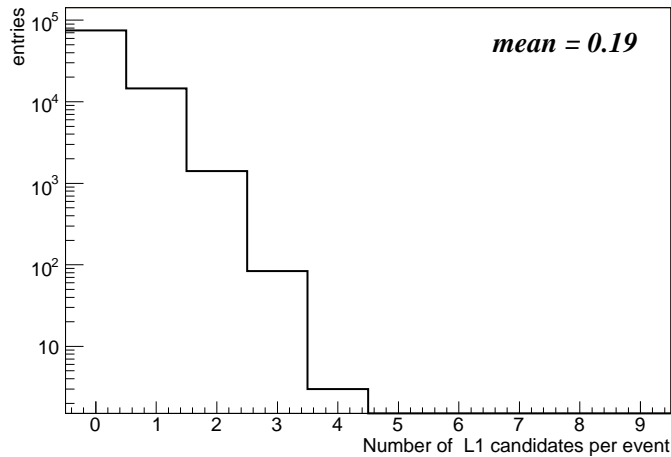

Figure B.36: Distribution of number of L1 EM candidates per event with at least one π^0 reconstructed. Loose selection criteria are applied and the number of read-out cells in the L1 EM candidates is required to be < 100.
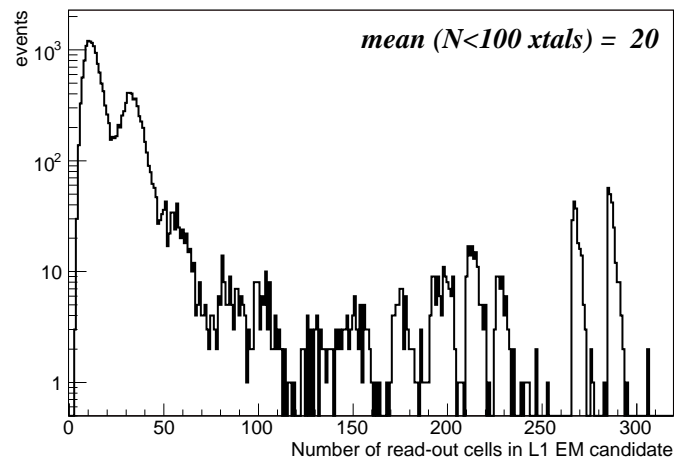
Figure B.37: Distribution of the number of cells that are read out in a L1 EM candidates with at least one reconstructed π^0. The average is computed for matrices with less than 100 cells read out.

Bibliography

[1] Weinberg, S. A Model of Leptons. *Phys. Rev. Lett., 19, 1264 (1967).*

[2] The LEP Electroweak Working Group. *http://lepewwg.web.cern.ch/LEPEWWG/.*

[3] The UTfit Collaboration. The 2004 UTfit Collaboration Report on the Status of the Unitarity Triangle in the Standard Model. *JHEP 0507 (2005) 028, hep-ph/0501199v2.*

[4] LEP Working Group for Higgs Boson Searches et al. Search for the Standard Model Higgs boson at LEP. *Phys. Lett. B 565 (2003) 61.*

[5] Hambye, T. and Riesselmann, K. SM Higgs mass bounds from theory. *DO-TH 97/18, DESY 97-152, hep-ph/9708416.*

[6] The K2K collaboration, Ahn, M. H. et al. Measurement of Neutrino Oscillation by the K2K Experiment. *Phys.Rev. D74 (2006) 072003, hep-ex/0606032.*

[7] Fogli, G.L. et al. Observables sensitive to absolute neutrino masses: a reappraisal after WMAP-3y and first MINOS results. *Phys.Rev. D75 (2007) 053001, hep-ph/0608060.*

[8] Tevatron Electroweak Working Group (for the CDF and D0 Collaborations). A Combination of CDF and D0 Results on the Mass of the Top Quark. *Fermilab-TM-2380-E, TEVEWWG/top 2007/01, arXiv:hep-ex/0703034.*

[9] Ross, Graham G. Grand Unified Theories. *Reading, Usa: Benjamin/cummings (1984) 497 P. (Frontiers In Physics, 60).*

[10] Peskin, Michael E. Beyond the standard model. *hep-ph/9705479, SLAC-PUB-7479.*

[11] WMAP Collaboration (D.N. Spergel et al.). Wilkinson Microwave Anisotropy Probe (WMAP) three year results: implications for cosmology. *Astrophys.J.Suppl.170:377,2007, astro-ph/0603449.*

[12] Siegel, Warren. Introduction to string field theory. *hep-th/0107094, YITP-SB-01-39.*

[13] N. Arkani-Hamed, S. Dimopoulos, and G. Dvali. The Hierarchy problem and new dimensions at a millimeter. *Phys. Lett. B 436: 263-272 (1998).*

[14] Martin, Stephen P. A supersymetry Primer. *hep-ph/9709356 2006.*

[15] Kazakov, D. I. Beyond the standard model. *hep-ph/0411064.*

[16] Chamseddine, Ali H. and Arnowitt, R. and Nath, Pran. Locally Supersymmetric Grand Unification. *Phys.Rev.Lett.49:970 (1982).*

[17] Randall, L. and Sundrum, R. Out Of This World Supersymmetry Breaking. *Nucl. Phys. B 557 (1999) 79-118, hep-th/9810155.*

[18] Kaplan, D. E. Supersymmetry Breaking through Transparent Extra Dimensions. *Phys. Rev. D 62 (2000) 035010, hep-ph/9911293.*

[19] Giudice, G. F. and Rattazzi, R. Theories with gauge-mediated supersymmetry breaking. *Phys.Rept.322:419-499,1999, hep-ph/9801271.*

[20] Dubovsky, S. L. and Gorbunov, D. S. and Troitsky, S. V. Gauge mechanism of mediation of supersymmetry breaking. *Phys.Usp.42:623-651,1999, Usp.Fiz.Nauk 169:705-736,1999, hep-ph/9905466.*

[21] Martin, Stephen P. Low scale and gauge mediated supersymmetry breaking at the Fermilab Tevatron Run II. *hep-ph/0008070.*

[22] Bagger, Jonathan A. and Matchev, Konstantin T. and Pierce, Damien M. and Zhang, Ren-jie. Weak scale phenomenology in models with gauge mediated supersymmetry breaking. *Phys.Rev.D55:3188-3200,1997, hep-ph/9609444.*

[23] Allanach, B. C. et al. The Snowmass Points and Slopes: benchmarks for SUSY searches. *Eur.Phys.J.C 25,113 123 (2002).*

[24] The LHC study group. LHC Design Report, 1995 CERN/AC/95-05 (LHC). *0212101.*

[25] Pumplin, J. et al. New Generation of Parton Distributions with Uncertainties from Global QCD Analysis. *JHEP 0207 (2002) 012, MSU-HEP-011101, hep-ph/0201195.*

[26] Achilli, A. et al. Total cross-section and rapidity gap survival probability at the LHC through an eikonal with soft gluon resummation. *IISC-CHEP-09-07, arXiv:0708.3626.*

[27] The CMS Collaboration. CMS Physics Technical Design Report Volume II: Physics Performance. *CERN/LHCC 2006-021, pag 1023.*

[28] The CMS Collaboration. CMS Physics Technical Design Report Volume I: Detector Performance and Software. *CERN/LHCC 2006-001.*

[29] The CMS Collaboration. The Tracker System Project Technical Design Report. *CERN/LHCC 98-6.*

[30] The CMS Collaboration. The CMS ECAL Technical Design Report. *CERN/LHCC 97-33.*

[31] Borgia B., Longo E., Baccaro S., Dafinei I. Tungstate crystals proceedings of the international workshop on tungstate crystals. *ISBN 88-87242-10-0.*

[32] Baccaro, S. et al. APD Properties and Recovery from Radiation Damage. *CMS NOTE-1997/030.*

[33] Camanzi B. et al. The Performance of Prototype Vacuum Phototriodes in the First Full Sized Supercrystal Array for the ECAL Endcaps. *CMS NOTE-2000/054.*

[34] M.Hansen. The New Read Out Architecture for the CMS ECAL. *CERN-LHCC-2003-055.*

[35] P.Adzic et al. Energy Resolution of the Barrel of the CMS ECAL. *CMS NOTE 2006/148.*

[36] Barone, L.M. et al. Improvement on PbWO4 Crystal Intercalibration Precision from Light Yield Measurements at the INFN-ENEA Regional Center. *CERN RN-2004/003.*

[37] P. Adzic et al. Results of the first performance tests of the CMS electromagnetic calorimeter. *Eur.Phys.J.C44S1:1-10,2006.*

[38] Bertl, W. et al. Feasibility of Intercalibration of CMS ECAL Supermodules with Cosmic Rays. *CMS NOTE-2004/036.*

[39] Bonesini, M. et al. Inter-calibration of the CMS electromagnetic calorimeter with cosmic rays before installation . *CMS Note 2005/023.*

[40] The CMS Collaboration. The CMS ECAL Technical Design Report - Calibration and Light Monitoring System. *CERN/LHCC 97-33, Chapter 6.*

[41] The CMS Collaboration. CMS Physics Technical Design Report Volume I: Detector Performance and Software - Phi independence. *CERN/LHCC 2006-001, Chapter 4, pag 172.*

[42] Meridiani, P. and Paramatti, R. On the use of Z —> e+ e- events for ECAL calibration. *CERN-CMS-NOTE-2006-039.*

[43] The CMS Collaboration. CMS Physics Technical Design Report Volume I: Detector Performance and Software - Intercalibration using single electrons. *CERN/LHCC 2006-001, Chapter 4, pag 175.*

[44] The CMS Collaboration. he Hadron Calorimeter Project Technical Design Report. *CERN/LHCC 97-31.*

[45] The CMS Collaboration. The Magnet Project - Technical Design Report. *CERN/LHCC 97-10.*

[46] The CMS Collaboration. The Muon Project - Technical Design Report. *CERN/LHCC 97-32.*

[47] ORCA. *http://cmsdoc.cern.ch/orca/.*

[48] The CMS Collaboration. The Computing Project Technical Design Report. *CERN-LHCC-2005-023.*

[49] Nicolai M. Josuttis. Object-Oriented Programming in C++. *JOHN WILEY & SONS, LTD.*

[50] COBRA. *http://cobra.web.cern.ch/cobra/.*

[51] CMKIN. *http://cmsdoc.cern.ch/cmsoo/projects/CMKIN/.*

[52] PYTHIA 6.4 Physics and Manual. *hep0603175, http://www.thep.lu.se/ torbjorn/Pythia.html.*

[53] OSCAR. *http://cmsdoc.cern.ch/OSCAR/.*

[54] GEANT4. *http://geant4.web.cern.ch/geant4/*.

[55] Baer, H. et al. ISAJET. *http://www.hep.fsu.edu/ isajet/*.

[56] Allanach, B. C. et al. SUSY Les Houches Accord: Interfacing SUSY Spectrum Calculators, Decay Packages, and Event Generators. *JHEP 0407 (2004) 036, CERN-TH/2003/204, hep-ph/0311123*.

[57] Goscilo,A. et al. Search for decaying in flight neutralinos and long lived staus within Gauge Mediated Supersymmetry Breaking models. *CMS-AN-2006-095*.

[58] Duhrssen, M. et al. The Process gg —¿ WW as a background to the Higgs signal at the LHC. *JHEP 0505:064,2005 , hep-ph/0504006*.

[59] Accomando, E. et Al. Electroweak corrections to W gamma and Z gamma production at the LHC. *Eur.Phys.J.C47:125-146,2006, hep-ph/0509234*.

[60] E.Meschi et al. Electron Reconstruction in the CMS Electromagnetic Calorimeter. *CMS Note 2001/034*.

[61] Franci, D. Graduate thesis on "Photon and neutral pions identification algorithms with the electromagnetic calorimeter of the CMS experiment". *http://www.roma1.infn.it/exp/cms/tesi/index.html*.

[62] Avery, P. et al. Measurement of Missing Transverse Energy With the CMS Detector at the LHC. *CMS NOTE 2006/035*.

[63] The CMS Collaboration. CMS Physics Technical Design Report Volume I: Detector Performance and Software - Missing transverse energy resolution in QCD events. *CERN/LHCC 2006-001, chapter 11, pag 414-15*.

[64] The CMS Collaboration. CMS Physics Technical Design Report Volume I: Detector Performance and Software - Jet reconstruction. *CERN/LHCC 2006-001, Chapter 11, pag 407*.

[65] The CMS Collaboration. CMS Physics Technical Design Report Volume I: Detector Performance and Software - HLT selection for photons. *CERN/LHCC 2006-001, chapter 10, pag 373*.

[66] The CMS Collaboration. CMS Physics Technical Design Report Volume II: Physics Performance - Theoretical uncertainties. *CERN/LHCC 2006-021, pag 1490*.

[67] D. Acosta et al. Search for Anomalous Production of Diphoton Events with Missing Transverse Energy at CDF and Limits on Gauge-Mediated Supersymmetry-Breaking Models. *Phys. Rev. Lett. 94, 041803 (2005).*

[68] Abazov, V. M. et al. Search for supersymmetry with gauge-mediated breaking in diphoton events at D0. *Phys.Rev.Lett.94:041801,2005.*

[69] The CMS Collaboration. CMS Physics Technical Design Report Volume II: Physics Performance - Experimental uncertainties. *CERN/LHCC 2006-021, pag 1500.*

[70] The CMS Collaboration. CMS Physics Technical Design Report Volume I: Detector Performance and Software - Luminosity Measurement. *CERN/LHCC 2006-001, chapter 8, pag 315.*

[71] The CMS/TOTEM Collaboration. Prospects for Diffractive and Forward Physics at the LHC. *CERN/LHCC 2006-039/G-124.*

[72] Mangano M. et al. How accurately can we measure the W cross section? *JHEP 0405 (2004) 056.*

[73] Konoplianikov, V. et al. Jet calibration using γ+jet events. *CMS NOTE 2006/042.*

[74] D'Hondt et al. Light quark jet energy scale calibration using the W mass constraint in single-leptonic $t\bar{t}$ events. *CMS NOTE 2006/025.*

[75] Esen, S. et al. $E\!\!\!/_{\mathrm{T}}$ performance in CMS. *CMS NOTE 2007/041.*

[76] Bartsch V., Quast G. Expected signal observability at future experiments. *IEKP-KA/2003-30.*

[77] Franzoni, G. The CMS electromagnetic calorimeter and its sensitivity to non pointing photons. *PhD Thesis, University of Milano-Bicocca (2004).*

[78] Marinelli, N. Track finding and identification of converted photons. *CMS NOTE 2006/005.*

[79] Bartoloni, A. et al. High Voltage System for the CMS Electromagnetic Calorimeter. *CERN-CMS-NOTE-2007-009.*

[80] CAEN, Tools for Discovery. *http://www.caen.it/.*

[81] Gataullin, M. Intercalibration of the CMS Barrel Electromagnetic Calorimeter Using Neutral Pion Decays. *CMS DN-2007/013.*

190

[82] Avoni, G. et al. The electromagnetic calorimeter of the HERA-B experiment. *Nucl.Instrum.Meth.A580:1209-1226,2007.*

[83] The CMS Collaboration. The TriDAS Project Technical Design Report, Volume I: The Trigger Systems. *CERN/LHCC 2000 - 38.*

[84] The CMS Collaboration. CMS Physics Technical Design Report Volume I: Detector Performance and Software - Selective readout. *CERN/LHCC 2006-001, Chapter 4, pag 156.*